

PREMIO FIRENZE UNIVERSITY PRESS  
TESI DI DOTTORATO

- 17 -



Francesca Di Patti

# **Finite-Size Effects in Stochastic Models of Population Dynamics**

*Applications to Biomedicine and Biology*

Firenze University Press  
2010

Finite-Size Effects in Stochastic Models of Population Dynamics : Applications to Biomedicine and Biology / Francesca Di Patti. – Firenze : Firenze University Press, 2010.

(Premio FUP. Tesi di dottorato ; 17)

<http://digital.casalini.it/9788884539175>

ISBN 978-88-8453-976-2 (print)

ISBN 978-88-8453-917-5 (online)

Progetto di copertina: Alberto Pizarro Fernández

© 2010 Firenze University Press  
Università degli Studi di Firenze  
Firenze University Press  
Borgo Albizi, 28  
50122 Firenze, Italy  
<http://www.fupress.com/>

*Printed in Italy*

# Contents

<b>Introduction</b>	<b>III</b>
<b>Chapter 1</b>	
<b>Theory of Pain</b>	<b>1</b>
1.1 The pathophysiology of pain	2
1.2 Reducing pain via pharmacological therapy	3
1.2.1 Opioid analgesics	4
1.3 Importance of personalized medicine	5
1.4 The case of Tramadol	7
1.5 Experiments	10
<b>Chapter 2</b>	
<b>Characterizing the individual response to medical treatment</b>	<b>15</b>
2.1 A comprehensive dynamical approach	16
2.1.1 A short account on one-dimensional diffusion	17
2.1.2 The mathematical model: Diffusion and time delay	19
2.1.3 Validation of the model	21
2.2 Unbiased tools for data processing	26
2.2.1 Markov cluster algorithm	27
2.2.2 Ecological clustering	28
2.3 The problem of missing data: Filling the gaps	32
2.3.1 Test case microarray inspired	34
<b>Chapter 3</b>	
<b>Role of fluctuations in the experienced pain perception</b>	<b>39</b>
3.1 The chemical equations governing the microscopic process	40
3.1 Neglecting the inward migration of inactive molecules	45
3.2.1 Considering the case $\hat{\delta}_1 = \hat{\eta}_1$	46
3.2.2 Mean -eld vs. stochastic numerical computations	49
3.2.3 Parameters for the resonance condition	51
3.1 On the general case	54
3.3.1 Assuming $\hat{\eta}_1 = \hat{\delta}_1$	56
3.3.2 General case	56

<b>Chapter 4</b>	
<b>A stochastic approach to the coupled parent drug and metabolite dynamics</b>	<b>61</b>
4.1 Description of the model	62
4.2 The deterministic limit	65
4.2.1 Analysis of the macroscopic equations	66
4.3 The van Kampen expansion	68
4.3.1 Analysis of the fluctuations	70
<b>Chapter 5</b>	
<b>Extended auto-catalytic networks</b>	<b>73</b>
5.1 Enhanced stochastic oscillations	74
5.1.1 On the fluctuations	78
5.2 On a spatial model of autocatalytic reactions	84
5.2.1 The perturbative expansion	85
5.2.2 Right hand side of the master equation: $N^{-1/2}$ terms	90
5.2.3 Right hand side of the master equation: $N^{-1}$ terms	91
5.2.4 The Fokker Planck equation	94
<b>Conclusions</b>	<b>99</b>
<b>A The Gillespie algorithm</b>	<b>103</b>
<b>Bibliography</b>	<b>109</b>

## Introduction

Population dynamics [1] constitutes a widespread branch of investigations which finds particularly important applications within the realm of life science. In general terms, it aims at characterizing the time evolution of interacting species of homologous entities, so to unravel, among others, the fundamental mechanisms which drive their dynamics as observed in real systems.

Population is indeed a technical term which is referred to various, completely distinct fields of applications ranging, from e.g. the level of expression of a protein in a cell, to the number of animals in a finite ecosystem.

The classical approach to population dynamics [2] relies on characterizing quantitatively the densities  $\mathbf{x} = (x_1, \dots, x_n)$  of  $n$  species through a system of ordinary differential equation of the type

$$\frac{d}{dt}\mathbf{x} = f(\mathbf{x})$$

where the function  $f$  depends on the specific interactions being at play. In other words, the analytical expression for  $f$ , incorporates pure competition, predator–prey interactions, or even cooperative effects. Moreover, a specific delay might be required to account for the processing time which is needed for a system under scrutiny to react to an external stimulus or signal [3]. This is a paradigmatic problem of many biological pathways. A classical example is the haematopoiesis, the formation of blood cellular components [4], where the production of thrombocytes is delayed of seven days with respect to the level of megakaryocytes, the progenitor cells. These latter take in fact seven days to complete their differentiation cycle. Towards a refined level of approximation, more than one independent variable is often to be assumed, which in turn implies dealing with the partial differential equation for an exhaustive modelization effort [5]. For instance, when tracing the dispersion of a diffusing chemical compound, space and time are to be explicitly encapsulated into the mathematical description.

However, and despite the degree of coarse–graining intrinsic to the model, all these are phenomena that can be tackled via the population viewpoint, namely focusing on the evolution of homogeneous family of constituents as whole, and solely allowing for effective (global) interactions between microscopic elements. It is customary to refer to this level of description as to the deterministic theory. Noise and other disturbances can be eventually hypothesized to alter the ideal deterministic, hence reproducible, dynamics but always act as a macroscopic bias.

As opposed to this formulation, a different level of modeling can be invoked which instead focuses on the individual–based description. This amounts to characterizing the microscopic dynamics via explicit rules governing the interactions among individ-

uals and with the surrounding environment. This former approach has been recently adopted in various contexts such as predator–prey interactions [6], metabolic reactions [7], and epidemic models [8]. These models are usually implemented numerically through algorithms which use random numbers, and for these reason we refer to these models with the term stochastic. The stochasticity is now intrinsic to the systems and stems from the microscopic finiteness of the investigated medium.

Those alternative, conceptual strategies translate into different tools for characterizing a given phenomenon under inspection, and it is therefore of interest to highlight similarities, and/or discrepancies, in the associated predictions. A viable method that enables us to bridge the gap between the two levels of description is the so-called van Kampen's system size expansion. Starting from the stochastic scenario and performing a perturbative development with respect to a small parameter which encodes the amplitude of finite size fluctuations, one recovers, at the leading order, the mean-field equations. These latter govern the coupled evolution of the average population amount, as in the spirit of the deterministic representation. Including the next-to-leading order corrections, one obtains a description of the fluctuations, as a set of linear stochastic differential equations. Such system can be hence analyzed exactly, so allowing us to quantify the differences between the stochastic formulation and its deterministic analogue.

Again, let us emphasize that fluctuations do not arise from an external noise. Despite the evidence that it is always present in actual population dynamics and that it is an essential ingredient of life processes, noise is often omitted. When instead considered, it is frequently assumed to act as a source of disorder and it is included in the dynamics as an external elements. At variance, the individual-level approach allows us to investigate the unavoidable intrinsic noise, which originates from the discreteness of the system and that has to be considered in any sensible model of natural phenomena.

In this thesis we will apply the van Kampen theory to a selection of problems in biomedicine and biology, for which we shall also propose dedicated interpretative framework. More specifically, we will focus on the role of finite-size corrections, and show how these might significantly alter the dynamics. In particular we shall analyze the molecular mechanisms involved in the perception of pain, and the autocatalytic reactions which widely occur in many biochemical processes.

The first chapter is devoted to introducing the main aspects involved in the neurobiology of pain. We will briefly describe the various types of pain and the corresponding pharmacological treatments. Moreover we shall mention the new frontier of the personalized medicine, making always reference to the problem of pain emergence.

The second chapter presents a gallery of methods, which we did developed as support of the experimental data analysis. First, a deterministic model is put forward to interpret drug kinetics data, with the aim of quantifying the individual response to a specific medical treatment. Moreover, the problem of missing data in microarray experiments is considered, and a method suggested that exploit the similarity between sequences. In the last section of this chapter, we report on a new algorithm for detecting different level of clustering.

The third chapter deals with a stochastic model to investigate the microscopic processes which trigger the sensation of pain. The model accounts for the action of analgesic drug and introduces an effect of competition among chemical species populating the bloodstream. Regular oscillations in the amount of bound receptors are detected, following a resonant amplification of the stochastic component intrinsic to the system.

The condition for such oscillations to occur are studied, resorting to combined numerical and analytical techniques. Extended and connected patches of the admissible parameters space are detected which do correspond to the oscillatory behaviors. These findings are discussed with reference to the existing literature on patients' response to the analgesic treatment.

In the fourth chapter we present a minimalist stochastic model for the mechanism of action of tramadol. The model accounts for the process of metabolization through the cytochrome CYP2D6 and the interactions between molecules and target receptors. From the master equation, through the van Kampen method, we obtain the macroscopic equations, and the Fokker Planck equation governing the fluctuations around the deterministic behavior. The role of fluctuation is discussed with reference to clinical tests and outcome of pharmacological therapy.

The last Chapter is dedicated to a different topic, where similar modelization techniques prove necessary. A simplified scheme of  $k$  coupled autocatalytic reactions is analyzed. This problem is supposedly related to the inner dynamics of a simplified model of cell, as previously recognized in the literature. The role of stochastic fluctuations is elucidated through the use of the van Kampen system-size expansion and the results compared with direct stochastic simulations. Regular temporal oscillations are predicted to occur for the concentration of the various chemical constituents, with an enhanced amplitude resulting from a resonance which is induced by the graininess of the system. Space is then accounted for, resulting in organized spatio-temporal structures.



## Chapter 1

### Theory of Pain

The International Association for the Study of Pain (IASP) defines pain as “an unpleasant sensory and emotional experience which we primarily associate with tissue damage or describe in terms of such damage, or both”. Although this is a vague definition, it recognizes that pain is a combined sensory, emotional, and cognitive phenomenon. Interestingly, physical pathologies do not necessarily manifest when a patient experiences pain. Indeed, pain can be thought of as being composed of three hierarchical levels: a sensory–discriminative component (e.g., location, intensity, quality), a motivational–affective component (e.g., depression, anxiety), and a cognitive–evaluative component (e.g., thoughts concerning the cause and significance of the pain) [9]. Clinically, this conceptual vision is useful to focus the attention on the broad range of factors that may contribute to the emergence of pain as reported by the patients.

In general terms, according to the medical literature, pain is “whatever the patient says it is”. One may argue that pain is a warning sensation delivered to the patient’s brain signalling that a stimulus is causing, or may cause, damage. Following this philosophy, the best clinical approach in most circumstances is to assume that the patient is reporting a true experience, even in the absence of an obvious demonstrable source of tissue injury. However, accepting a patient’s complaint of pain as valid does not necessarily demand the initiation of a specific treatment.

The difficulties in the pharmacological management of pain are not solely related to the complex underlying network of molecular interactions, which remains at present to be fully elucidated. As an additional complication, the same administered dose of drug can result in a wide variability of effects, depending on specific individual traits. This observation points to the need for the so called personalized medicine, one of the new challenges of the post genomic era. This, relatively novel discipline elaborates information on the genetically determined variability in the metabolism of drugs, aiming at developing personalized pharmacological protocols to enhance the effectiveness of the therapy.

This chapter is devoted to providing a general, though synthetic, overview on the neurobiology of pain. We shall be in particular interested in highlighting the various types of pain and discussing possible treatment strategies. The pharmacological aspects are here briefly reviewed with reference to the issue of personalized medicine.

## 1.1 The pathophysiology of pain

Pain perception, or nociception (from the Latin word for “hurt”), is the process by which a painful stimulus is transmitted from the site of stimulation to the central nervous system. Several successive steps are to be accounted for in the nociception process: The contact with stimulus, the reception, the transmission and the pain center perception [10, 11, 12]. In the following we shall set down to analyzing those processes.

The contact with the stimulus can be mechanical (pressure, punctures and cuts) or chemical (burns). As an example, we can consider the cut of a finger. The stimulus is captured by nociceptors, nerve cell endings that, like normal sensory neurons, travel in peripheral sensory nerves. Their cell bodies lie in the dorsal root ganglia of peripheral nerves just inside the spine. Nociception uses different neural pathways than normal perception (like light touch, pressure and temperature). In response to non-painful stimulation, the first group of neurons to fire are normal somatic receptors. At variance, when external agents cause pain, nociceptors are activated at first. Nociceptors, indeed, sense pain via free nerve endings rather than specialized endings such as those involved in resolving the touch or pressure feelings. However, while normal sensory neurons are myelinated (insulated) and conduct quickly, nociceptor neurons are lightly or non-myelinated and slower. We can divide nociceptors into three classes: The  $A\delta$ -mechanosensitive receptors and the  $A\delta$ -mechanothermal receptors which are faster conducting neurons that respond to mechanical stimuli (pressure, touch) and to heat, and the polymodal nociceptors (C fibers) which are slowly conducting neurons that respond to a variety of stimuli. After the cut of the finger, several factors contribute to the reception of pain: The mechanical stimulation, the potassium released from the insides of the damaged cells, the prostaglandins, histamines and bradykinin from immune cells that invade the area during inflammation, and the substance P<sup>1</sup> from nearby nerve fibers. These substances cause action potentials in the nociceptor neurons. The first sensation experienced at the moment of the injury is an intense pain. The signal for this pain is conducted rapidly by the  $A\delta$ -type nociceptors. The pain is followed by a slower, prolonged, dull ache, which is instead conducted by the slower C-fibers.

In this way, the signals originated from the injury event travel into the spinal cord through the dorsal roots. There, they make synapses<sup>2</sup> on neurons within the dorsal horn (the top half of the butterfly-shaped gray matter). They synapse on neurons within the spinal cord segment and also on neurons one to two segments above and below their segment of entry. These multiple connections relate to a broad area of the body. This in turn explains why it is sometimes difficult to determine the exact location of pain, especially internal pain. The secondary neurons send their signals upward through an area of the spinal cord's white matter, termed the spinothalamic tract. This area can be pictorially seen as a highway: Traffic from all of the lower segments rides up the spinal cord. The signals of the spinothalamic tract is transmitted along the spinal cord through the medulla (brain stem) and synapse on neurons which are located in the thalamus, and act as brain's relay center. Some neurons also synapse in the medulla's reticular formation, a region which is deputed to physical behaviors. Nerves from the thalamus then pass the signal to various areas of brain's somatosensory cortex.

<sup>1</sup> Substance P is a neuropeptide, namely a short-chain polypeptide that functions as a neurotransmitter and as a neuromodulator which alters the excitability of the dorsal horn ganglion (pain responsive neurons).

<sup>2</sup> Synapse is the functional connections between neurons, or between neurons and other types of cells.

Once the pain information reaches the brain, it gets processed following schemes which are still to be completely resolved. Obviously, the signals should eventually reach the motor cortex, then down through the spinal cord and to the motor nerves. These impulses would cause muscle contractions to move the hand so to escape the source of potential injury.

Physicians and neuroscientists generally classify pain depending on its duration, or according to the associated clinical characteristics.

When it comes to quantifying the time duration, pain can be divided in three main classes, namely acute, chronic and cancer pain. Acute pain is caused by an injury to the body. It warns on a potential damage that requires immediate action. It can last for a few minutes to six months and fade off when the injury heals. Chronic pain persists long after the trauma has healed (notice that, in some cases, it may occur in the absence of any trauma). Chronic pain does not warn the body to respond, and it usually lasts longer than six months. Finally, cancer (or malignant) pain is clearly associated with malignant tumors. Tumors tend to invade healthy tissues so exerting a mechanical pressure on the nerves or blood vessels, which generates pain. Occasionally, cancer pain can be also classified as chronic pain.

A grouping based on inferred pathophysiology, broadly classifies pain syndromes into nociceptive, neuropathic, psychogenic or idiopathic [13]. These latter categories are here quickly reviewed.

Clinically, pain can be labeled “nociceptive” if it directly correlates to the degree of tissue injury. More specifically, nociceptive pain is presumed to occur as a result of the normal activation of the nociceptive system by noxious stimuli. This type of pain response also occur in presence of inflammation (inflammatory pain).

Neuropathic pain refers instead to dysfunction of the peripheral or central nervous system (CNS). These may be caused by injury to either neural or non-neural tissues. Although neuropathic pain is certainly influenced by ongoing tissue injury, it can be sustained by fundamental mechanisms which have become independent of the initial injury or damage. A continuing sensation of pain is in fact reported after the stimulation has ceased. Neuropathic pain presents diverse characteristics: On the one hand it mimics the qualitative features of somatic pain. On the other, it is also frequently described as a continuous burning, shock-like or paresthetic [14].

The patient’s psychological state contributes importantly to pain perception and associated suffering symptoms [15]. The patient’s self-report on pain should be evaluated while assessing other factors of paramount importance, as the presence of anxiety, depression, or other psychiatric disorders. In some cases, pain itself can be intimately linked to the psychological dimension, a phenomenon generically referred to as “psychogenic” pain. However, when convincing inferences about the pathophysiological origin of the pain syndrome cannot be made, it is customary to diagnosis the so called “idiopathic” pain.

## 1.2 Reducing pain via pharmacological therapy: Analgesics

An analgesic, also known as a painkiller, is any member of the rather complex family of drugs, commonly employed to relieve pain or, equivalently, achieve analgesia. The word analgesic comes from Greek an- (“without”) and -algia (“pain”).

Analgesic drugs act in various ways on the peripheral and central nervous systems.

The main classes of analgesics are the narcotics and the nonsteroidal anti-inflammatory drugs (NSAIDs). The narcotic analgesics, also termed opioids, are all derived from opium. The narcotic analgesics may vary in potency, but they are all extremely effective when used in adequate doses. A number of chemical classes can be identified, but all share similar therapeutic effects and side effects. Notably, analgesics do provide a symptomatic relief, but, in general, they have no direct effect on the generating cause.

Although pain syndromes may be different in many respect, the sensory pathway is ultimately solicited by the affected organ/tissue to the brain. Analgesics act at the level of the nerves, either by blocking the signal from the peripheral nervous system, or by distorting the subsequent processing by the central nervous system.

To clarify the key elements that are to be encapsulated in a sensible mathematical model, as developed in the following, we shall here concentrate on reviewing the principle of opioids' action.

### 1.2.1 Opioid analgesics

Beneficial and/or adverse effects of opioid analgesics can be traced to their interaction with the endogenous opioid systems [16]. Opioid agents and their receptors populate the central and peripheral nervous systems and other tissues. Opioid systems are indeed crucial in a vast gallery of homeostatic functions and movement control, as well as involved in the processing of noxious sensory input. The antinociceptive system, from which pain modulation stems, is itself extraordinarily complex. Information on this system constitute a useful background for understanding the effects associated to opioid analgesics.

Pain transmission in the spinal cord is regulated by a balance of facilitatory and inhibitory influences. These latter operate on the neural circuits of the somatosensory system. Noxious stimuli activate high-threshold primary sensory neurons in the periphery. This seeding activity is then conducted to their central terminals, which synapse on nociceptive (secondary) neurons in the spinal cord. Although opioid compounds are found in the periphery as well, they produce the condition for analgesia by primarily inhibiting the nociceptive transmission in the central nervous system (CNS).

Opioid receptors positioned presynaptically and postsynaptically at the first central synapse in the spinal cord have been extensively analyzed. Those located on the presynaptic nerve terminal decrease the release of excitatory neurotransmitters from nociceptive neurons and respond to a large spectrum of noxious stimuli. Such a presynaptic inhibition reflects by the opioid receptor activation on ion channels. More into details, opioid activation yields to hyperpolarization of the terminal through the opening of potassium channels or closing of calcium channels, the hyperpolarized neurons having a smaller probability to give rise to spontaneous discharge or evoked responses. Opioid receptors located postsynaptically have similar effects on the secondary neuron. Hyperpolarization caused by changes in ion fluxes leads to a reduced response of this neuron as an excitatory input is sent by primary nociceptive neurons.

Opioids exert their analgesic effects by binding (and then activating) receptors that are part of the endogenous opioid system. This latter usually operates so to modulate the sensory input as caused by noxious stimuli, its response being activated by endogenous peptide neurotransmitters. Opioids can in turn mimic and, importantly, amplify the actions of those neurotransmitters.

The endogenous opioid system includes a large plethora of opioid peptides which

are ligands for numerous types of opioid receptors. Some of these naturally produced peptides, induce a morphinelike effects and can be displaced from their apposite binding sites by opioid antagonists. Three distinct families of endogenous opioid peptides are often invoked: the endorphins, the enkephalins, and the dynorphins, which derive from the precursor polypeptides pro-opiomelanocortin, proenkephalin, and prodynorphin, respectively.

The endogenous opioid peptides do bind to opioid receptors. In the CNS, there are 3 primary types of opioid receptors that mediate analgesia and are respectively labeled  $\mu$ ,  $\kappa$ , and  $\delta$ . Enkephalins interact preferentially with the  $\delta$  receptor, dynorphins with the  $\kappa$  receptor, while endorphins bind to both  $\mu$  and  $\delta$  receptors with a similar degree of chemical affinity. As previously remarked, those peptides display rather diverse physiologic functions, one of which is associated to the antinociception effect here discussed. In different systems and settings, they can function as neurotransmitters, neuromodulators or, even, neurohormones.

Drugs targeted to opioid receptors are broadly divided in four classes: agonists, partial agonists, mixed agonist-antagonists, and antagonists. Receptor activation by an agonist launches the pharmacologic actions, whereas an antagonist sit on the receptor without inducing any sensible effects. The intrinsic activity of a drug is then regarded as a quantitative indicator to distinguish between the aforementioned classes, including the intermediate categories. Partial agonists may also have antagonistic properties, because they compete with pure agonists for occupancy of opioid receptor sites. The degree of competition is determined by their affinity score to the receptor. For example, Buprenorphine hydrochloride, an analgesic used for addiction therapy, is a partial agonist being characterized by a very high affinity for the  $\mu$  receptor; it can hence chase for the receptor and so have antagonist properties. The opioid analgesics most commonly used in clinical practice bind selectively to the  $\mu$  receptor and are called  $\mu$ -agonists. Morphine is the prototypical example of  $\mu$ -agonist. Despite the similarities between morphine and other  $\mu$ -agonists agents, different drugs can result in a large variety of effects in the individual patient. Consider for instance a patient who is chronically exposed to a  $\mu$ -agonist and assume that it is suddenly switched to another: Pain can often be controlled by administering doses of the second drug that are by far lower than estimated according to their relative potencies and both the pattern and severity of non-analgesic effects can be distinct. This observation, widely known as incomplete cross-tolerance, suggests that these  $\mu$ -agonists are not acting through identical receptors.

As it should be clear from the above, a consistent molecular model for drug absorption requires accommodating for several different effects, which simultaneously cooperate with positive or negative interference. In the forthcoming chapters we shall focus on a limited set of key mechanisms which, we believe, do play a role of paramount importance. In particular, anticipating our developments, we shall describe the dynamics of the active molecular agents by including the effect of the stochastic search for the target receptor and the competition with other chemical species populating the bloodstream.

### 1.3 Importance of personalized medicine

In medicine, individual response is crucial. Two patients, exposed to the same treatment can, for instance, experience completely different effect. Severe, even life-threatening

ning, side effects can be reported in one case, while in the other only minor consequences are registered. Alternatively, the drug may shrink an illness in one person but not in another.

The body is a complex machine, and so many factors participate in making the response to an external input hard to predict. One major source of distinction between individuals stems from the inherited variations in the individual genes. Even slight variations can alter the reaction of the body. Pharmacogenomics is the science that studies, among other things, how individuals react to an administered medication. Pharmacogenomics is sometimes described as “personalized” or “individualized” medicine because it holds the promise to eventually devise specific drug treatments based on the individual genetic background.

Pharmacogenomics is indeed a promising field. A handful of tests are nowadays made available that can detect some of the genetic variations and so help predicting how a patient is likely to respond to an imposed medical treatment. Just to clarify, it could be revealed via the genetic analysis that a scrutinized patient is carrying a genetic modification which makes the drug stay in the body longer than normal, so eventually causing serious side effects. On the contrary, she/he may have a variation that reduces the effectiveness of the medication: This is hence less potent than reported on average. Once a variation is identified, scientists might be able to match it up with a response to a particular medication and so develop a personalized approach to medicine.

Often the sensitivity versus a drug is due to a very small genetic modification that yields to a decreased activity of a particular enzyme responsible for the biotransformation of that drug. More precisely, once introduced in the body, drugs undergo a process of metabolization which converts them to metabolites. These latter are more water soluble with respect to the original compound and thus can be more easily excreted. Metabolism can also convert prodrugs (pharmacological substance administered in an inactive form) into therapeutically active compounds, and it may even result in the formation of toxic metabolites [17]. Pharmacologists classify pathways of drug metabolism as either phase I reactions (i.e. oxidation, reduction and hydrolysis) or phase II conjugation reactions. Among enzymes that catalyze phase I drug metabolism, the most important are the cytochrome P450 enzymes, a superfamily of microsomal drug-metabolizing enzymes [17]. One member of this family, cytochrome P4502D6 (CYP2D6) is by far the most intensively studied and best understood example of pharmacogenetic variations in drug metabolism. The *CYP2D6* gene<sup>3</sup> is highly polymorphic with over 70 known alleles identified at the CYP2D locus on chromosome 22q13. At least 15 of these alleles encode nonfunctional gene products as a result of single nucleotide polymorphisms (SNPs), gene deletion, aberrant splicing or premature translation termination. Carriers of two nonfunctional alleles show a severely impaired metabolism of CYP2D6 substrates and are customarily referred to as poor metabolizers (PMs). In contrast, individuals with at least one functional allele and thus normal CYP2D6 activity are termed extensive metabolizers (EMs). Among Caucasians, 5–10 % are PMs and further 10–15 % show impaired yet residual activity of CYP2D6, the so called intermediate metabolizers (IMs). The 1–5 % of the Caucasian population has a duplication or multi-

<sup>3</sup> Genes encoding CYP enzymes, and the enzymes themselves, are designated with the abbreviation “CYP”, followed by an Arabic numeral indicating the gene family, a capital letter indicating the subfamily, and another numeral for the individual gene. The convention is to italicise the name when referring to the gene.

Designation	Mutations	Enzyme activity	Allelic frequency in Caucasian	Allelic frequency in African	Allelic frequency in Oriental
<i>CYP2D6*1</i>	Wild-type	Normal			
<i>CYP2D6*2</i>	Several substitutions	Normal	18	20	10
<i>CYP2D6*3</i>	A <sub>2549</sub> deletion	Deficient	2	0	0
<i>CYP2D6*4</i>	G <sub>1846</sub> A substitution	Deficient	12–22	1–2	0–1
<i>CYP2D6*5</i>	Gene deletion	Deficient	2–7	4–6	6
<i>CYP2D6*9</i>	G <sub>2613</sub> –A <sub>2615</sub> deletion	Decreased	2	2	3
<i>CYP2D6*10</i>	C <sub>100</sub> T substitution	Decreased	1–2	4–6	51
<i>CYP2D6*17</i>	C <sub>1023</sub> T, C <sub>2850</sub> T substitutions	Decreased	0	17–35	0
<i>CYP2D6*41</i>	C <sub>–1584</sub> G, G <sub>2988</sub> A substitutions	Decreased	8	10	3
<i>CYP2D6</i> ×2	Gene duplication	Increased	1–10	2–29	0–2
<i>CYP2C9*1</i>	Wild-type	Normal			
<i>CYP2C9*2</i>	C <sub>430</sub> T substitution	Decreased	8–13	4	0
<i>CYP2C9*3</i>	A <sub>1075</sub> C substitution	Decreased	6–9	2	2–3
<i>CYP2C19*1</i>	Wild-type	Normal			
<i>CYP2C19*2</i>	G <sub>681</sub> A substitution	Decreased	13	13–25	23–32
<i>CYP2C19*3</i>	G <sub>636</sub> A substitution	Decreased	0	0–2	6–10

Table 1.1: *CYP* allele subgroups, characteristic mutations, enzyme activity and frequency among Caucasians, Africans and Orientals. Data are derived from references [18, 19, 20, 21, 22, 23]

duplication of the *CYP2D6* gene leading to the phenotype of ultra rapid metabolisers (UMs) [24].

Table 1.1 clearly indicates that the polymorphisms are not occasional mutations. On the contrary, they are widespread in the population. It is hence natural to assume that this pronounced degree of variability might interfere non trivially with the process of drug absorption. Before proceeding with a pharmacological treatment, one should have a clear picture on the genetic characteristic of the patient being treated.

In the next section we will make reference to the case of a synthetic opioid, the tramadol, to illustrate how the genetic polymorphism of cytochrome P450 deeply affects the mechanism of the drug's action.

#### 1.4 The case of Tramadol

In this section we review the main features of tramadol hydrochloride (tramadol), a centrally acting analgesic that is structurally related to codeine and morphine. The interested reader may refer to [25] for an exhaustive account on the subject.

Tramadol was first synthesized in 1962 and has been available for pain treatment in Germany since 1977. It is administered as drops, capsules and sustained-release formulations for oral use, suppositories for rectal use and solution for intramuscular, intravenous and subcutaneous injection. After oral administration, tramadol is rapidly and almost completely absorbed. It is mainly excreted via the kidneys. Plasma protein

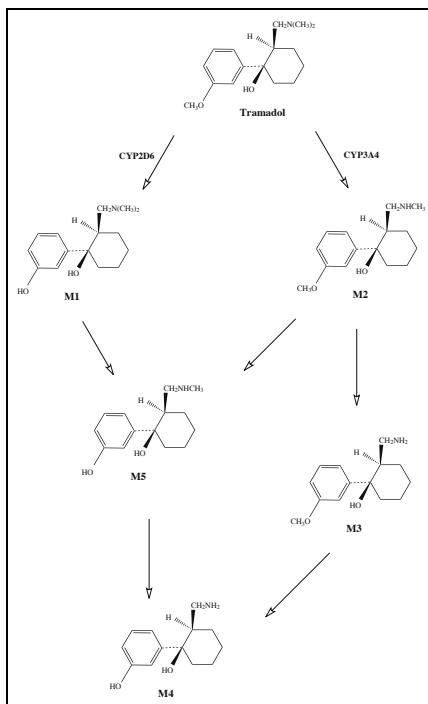


Figure 1.1: Some known metabolic pathways of tramadol.

binding is about 20%.

The human *in vivo* metabolism of tramadol is complex with 23 metabolites being identified: 11 phase I metabolites and 12 phase II conjugates. The major metabolic pathways (see Fig.1.1 ) are O-demethylation<sup>4</sup> to O-desmethyl-tramadol (M1) by the polymorphic isozyme cytochrome P450 2D6 (CYP2D6), and N-demethylation to N-desmethyl-tramadol (M2) by cytochrome P450 2B6 (CYP2B6) and cytochrome P450 3A4 (CYP3A4). The primary metabolites of tramadol, may be further metabolized to three secondary metabolites, namely N,N-desmethyl-tramadol (M3), N,N,O-tridesmethyl-tramadol (M4) and N,O-desmethyl-tramadol (M5).

As already mentioned in the preceding section, the gene encoding for cytochrome CYP2D6 is known to show polymorphisms and the existence of different alleles results in functionally different enzymes. For this reason, the biotransformation of tramadol changes within the phenotypic population depending on the genotype of CYP2D6. More-

<sup>4</sup> Demethylation is the chemical process resulting in the removal a methyl group (CH<sub>3</sub>) from a molecule. In biochemical systems, this process is often catalyzed by an enzyme such as one of the cytochrome P450 (CYP) family of liver enzymes. N-demethylation and O-demethylation are reactions which remove a group CH<sub>3</sub> from NCH<sub>3</sub> and OCH<sub>3</sub>.

Drug	Opioid receptor affinity			Uptake inhibition	
	$\mu$	$\delta$	$\kappa$	norepinephrine	serotonin
(±)-Tramadol	2.1	57.6	42.7	0.78	0.9
(+)-Tramadol	1.3	62.4	54.0	2.51	0.53
(-)-Tramadol	24.8	213	53.5	0.43	2.35
(+)-M1	0.0034				
Morphine	0.00034	0.092	0.57	inactive	inactive
Imipramine	3.7	12.7	1.8	0.0066	0.021

Table 1.2: Relative activity for inhibition of opioid receptor binding or monoamine uptake. Data (expressed in  $\mu\text{mol/L}$ ) from [26, 27].

over tramadol is administered as a racemic mixture<sup>5</sup> of two enantiomers<sup>6</sup>, (+)-tramadol and (-)-tramadol, that are essentially metabolized by the liver producing (+)-metabolites and (-)-metabolites, respectively.

In vitro and in vivo studies have convincingly shown that the metabolism and distribution of tramadol are stereoselective<sup>7</sup>. In other words, out of two (or more) possible reactions, one predominates. In vitro, O- and N-demethylation of tramadol were both shown to be stereoselective. The O-demethylation of tramadol, leading to M1, was determined to be two fold greater for the (-)- enantiomer than for the (+)-enantiomer. On the other hand, N-demethylation, leading to M2, was considerably faster after incubation of the (+)-enantiomer compared with the (-)-enantiomer. Since O-demethylation is the preferred pathway for biotransformation of tramadol, higher plasma concentrations of (+)-tramadol and (-)-M1 compared with (-)-tramadol and (+)-M1, respectively, can be expected in vivo.

To study the stereoselectivity of renal clearance, isolated kidneys of rats were perfused with tramadol and M1. The renal clearance of the enantiomers of both compounds was stereoselective, (-)-tramadol and (+)-M1 being preferentially eliminated. In addition, the O-demethylation of tramadol was stereoselective in the kidneys, (-)-tramadol being preferentially metabolized.

Both tramadol and metabolites contribute to the analgesic activity via different mechanisms. Tramadol displays only a modest affinity for  $\mu$  opioid receptors and no affinity for  $\delta$  or  $\kappa$  opioid receptors. The affinity of tramadol for  $\mu$  opioid receptors is approximately 10-fold less than that of codeine and 6000-fold less than that of morphine. These scores for the affinity, taken as such, do not seem sufficient to explain the observed analgesic action of tramadol (see Fig. 1.2).

<sup>5</sup> In chemistry, a racemic mixture, or racemate, is one that has equal amounts of left- and right-handed enantiomers of a chiral molecule.

<sup>6</sup> Enantiomer is one of two stereoisomers (molecules that have the same molecular formula and sequence of bonded atoms, but which differ in the three dimensional orientations of their atoms in space) that are non-superposable complete mirror images of each other.

<sup>7</sup> Stereoselectivity is the property of a chemical reaction in which a single reactant forms an unequal mixture of stereoisomers during the creation of a new stereocenter. The selectivity arises from differences in steric effects and electronic effects in the reactions leading to the two products.

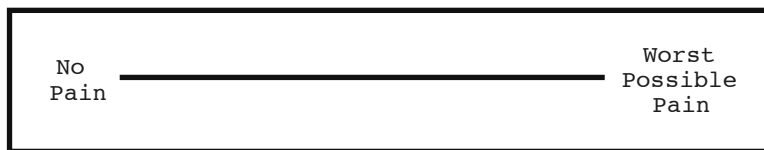


Figure 1.2: Visual Analog Scale

On the contrary, the metabolite M1 binds with about 300-fold higher affinity than the parent compound. Still, it has a much lower affinity when compared to morphine. The increase in subjective (and objective) pain thresholds as induced by tramadol is, at variance with what happens for other opioids, only partially blocked by the opioid antagonist naloxone. Therefore, the activation of  $\mu$  opioid receptors appears to be only one of the components of the mechanism of action of tramadol. More precisely, (+)-tramadol has a 2-fold higher affinity for the  $\mu$  opioid receptor than the racemate. Of the metabolites, (+)-M1 has the highest affinity for the  $\mu$  opioid receptor, being about 700-fold more potent than the ( $\pm$ )-tramadol. Another metabolite with a higher affinity than the ( $\pm$ )-tramadol for the  $\mu$  opioid receptor is ( $\pm$ )-M5.

In addition to its opioid action, tramadol inhibits the neuronal re-uptake of norepinephrine. In particular both the enantiomers of tramadol are involved in this pathway, the (+)-enantiomer being about 4-fold more potent than the (-)-enantiomer. Moreover ( $\pm$ )-tramadol and its (+)-enantiomer, but not the (-)-enantiomer and M1, increase serotonin efflux.

In conclusion, we can summarize saying that (+)-M1 acts as a  $\mu$  opioid agonist, (+)-tramadol inhibits serotonin re-uptake and (-)-tramadol inhibits norepinephrine re-uptake. The activity of the other kind of metabolites has not yet been studied.

## 1.5 Experiments

In the preceding sections we presented a general, though synthetic, overview on of the main phenomena that are involved in pain expression and management. Those aspects can be brought into evidence via dedicated experiments which enables researches to gain a comprehensive and quantitative insight into the problem at hand.

When dealing with pain, it is crucial to quantify its associated intensity. Clinicians dispose of several, carefully validated, pain scales. Among them, the Visual Analog Scale (VAS) is by far the most adopted in medical practice. VAS is essentially a visual questionnaire. The patient has to mark a sign on a graduated line (usually ten centimeters long) in the position that he feels would best correlate to the sensation of pain that he is experiencing. The reference positions are respectively the leftmost extreme on the line, labeled with “no pain”, and its end point which is assumed to correspond to the “worst possible pain” (see Fig. 1.2).

Clearly, such a method cannot be regarded as an objective criterion for pain assessment, actual responses being strongly influenced by diverse psychological factors, as the emotional state or the anxiety. To overcome this obvious limitation, other methods have

been developed and extensively employed to quantify the effectiveness of a pharmacological treatment. One of such objective criterion, often referred to as a physiological marker of pain, is the Evoked Response Potential (ERP). ERP is a time dependent electrical potential which is recorded from a human patient (or an animal), following an external stimulus. The time series of the brain electric activity is acquired via electrodes positioned on the head. The signal refers to the local activity of simultaneously firing neurons, and hence return a convolved information which necessitate further elaboration. Working with animals, more invasive tests have been conducted, allowing to unambiguously relate the registered signal to an externally imposed input. Aiming at clarifying the above technique, we shall here briefly recall the experiments described in [28]. In this paper, the authors investigate the effect of common anesthetic, on the rodent whisker sensory system. To this end an electrode array is implanted on the somatosensory cortex of adult rats. The electrode is uniquely sensitive to the cluster of neurons which are connected to a specific whisker barrel. In this respect, it allows to register EEG and ECG signals (and their time evolution) after a whisker stimulation event. Figure 2 of [28] reports on the main conclusion of the aforementioned study. Different panels represent the EEG and ECG amplitude respectively under anesthetized, wake, and sleep conditions. It can be immediately remarked that, while ERPs from control (non treated) rats present rather stochastic patterns, regular cycles are instead found to emerge when the animal are kept under pharmacological treatment. This observation constitutes indeed an indirect signature of medicaments' action, which ultimately stems from their associated molecular peculiarity. As already noticed above, anesthetics act on large sets of biochemical reactions, being in principle directed towards independent neuronal families, and so determining profound differences in the evoked response components.

Besides estimating the degree of experienced pain with a certain level of accuracy, it is also important to access a genetic screening of the patient being treated so to optimize the administered pharmacological protocol. Human DNA sequencing opened up novel scenarios and, among other things, translated into reliable methodologies for characterizing gene expression levels and detecting the presence of SNPs or deletion/duplication in the genome.

These methods are essentially based on the well known microarrays technology. Microarrays are solid surfaces on which a series of thousands of microscopic spots of DNA oligonucleotides are arrayed. Each spot contains a small portion of DNA sequence specific for a gene. This can be a short section of a gene or other DNA element that are used as probes to hybridize a cDNA or cRNA sample previously labeled with a fluorophore dye. The idea is to determine relative abundance of nucleic acid sequences in the target, by monitoring the intensity of the emitted fluorescence.

This is a rather powerful technology which enables for massive (and parallel) studies of genes activation within a given biological system. In the last few years, microarrays have been widely applied to the field of genetic polymorphism. As an example, the AmpliChip CYP450 Test manufactured by Affymetrix for Roche Diagnostics made it possible to carry out a comprehensive analysis of two, particularly important, genes which encode enzymes crucial in mediating drug efficacy and adverse drug reaction. The tests allow one to detect genetic variations in the Cytochrome P450 2D6 and 2C19 genes and provides the associated predictive phenotype profile (poor, intermediate, extensive, or ultra-rapid metabolizer). The AmpliChip CYP450 Test distinguishes among 29 known polymorphisms in the CYP2D6 gene, including gene duplication and gene deletion.

With reference to the CYP2C19 gene, the test can resolve the two major polymorphisms so far isolated. The actual implementation of the methodology is quite straightforward and non invasive. Only a sample blood from the patient is required. The blood is then manipulated in the laboratory so to perform a PCR amplification of selected segments of the DNA extracted from the patient sample. The amplified DNA segment is labeled with a fluorescent dye and then inserted into the AmpliChip CYP450, a plastic cartridge housing the microarray. The following step consists in the hybridization and scanning of the chip. The hybridization takes place into the Affymetrix hybridization chamber: The complementary base-pairs from the DNA fragments in the sample hybridize with those on the microarray which give a perfect match. Technical problems related on this specific operation will be reviewed in the forthcoming chapter. Then the Amplichip is moved to the Affymetrix scanner, where laser scanning of the hybridization pattern is performed. Images captured with the scanner are analyzed through a dedicated software which brings into evidence the genetic variations and quantifies the corresponding phenotype.

The phenotypic profile of the patient constitutes a useful indicator which can help physicians to design the most appropriate drug and dose selection. Moreover, beyond the realm of purely genetic investigations, pharmacokinetics can also guide on the choice of the optimal therapy. The principles of pharmacokinetics, synergistically integrated with a pharmacodynamics viewpoint, are in fact useful ingredients to elucidate the complex dose-effect relationships. Figure 1.3 presents a schematic interpretation of the interplated complementarity referenced above. Pharmacodynamics correlates the concentration of drug as measured in the blood to its induced effect. Pharmacokinetics aims at quantifying, under different conditions, the administered dose which is necessary to produce the sought concentration amount (as required by pharmacodynamics paradigms) [29]. This latter task necessitates accounting for various important ingredients as absorption, distribution, metabolism and excretion (ADME). Absorption is the process through which the substance is propagated from the administration site to the systemic circulation. Distribution studies instead the dispersion of the drug molecules throughout the fluids and tissues of the body. Metabolism relates to the biotransformation of the substance which yields to the metabolites. Finally, excretion clarifies the end process of the drug elimination from the body.

Quantifying the four levels of the ADME process, implies estimating the associated pharmacokinetic reaction parameters. To this end a suitable mathematical model can be numerically fitted to the plasma drug concentration data as seen from blood samples. Textbooks on pharmacology [30, 31] reports indeed on very crude mathematical formulations which are by far reminiscent of the key physiological aspects involved. Indeed, rough compartmental ansatz are put forward which allow to define averaged mathematical indicators. This latter are then extracted from real data via a simplistic inspection on the acquired experimental series. No serious attempt to perform direct, non linear, fitting is registered that could provide a more sensible ensemble of the estimated parameters.

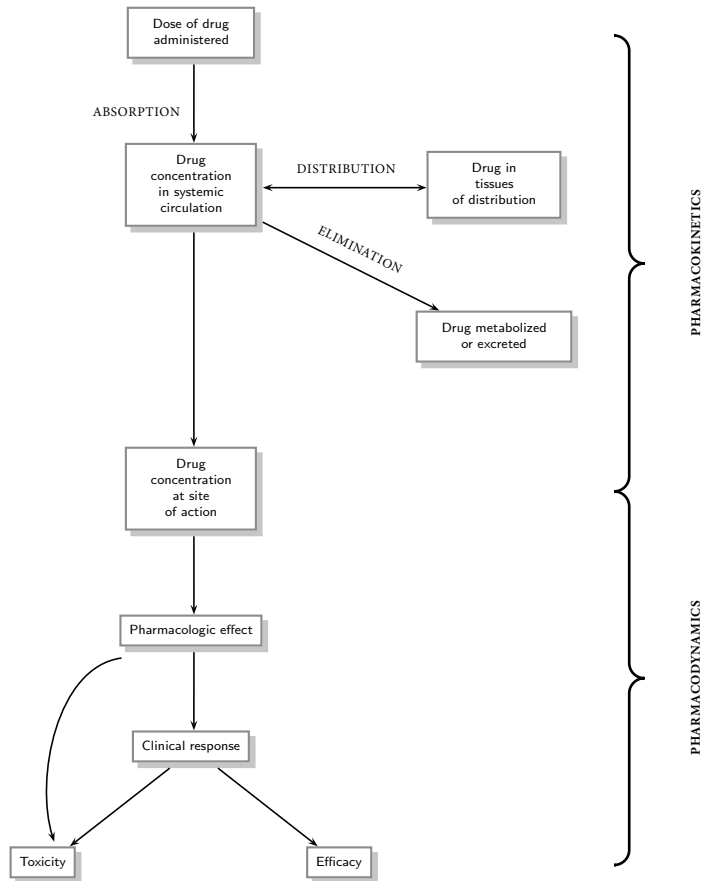


Figure 1.3: The relationship between dose and effect can be divided into pharmacokinetic (dose–concentration) and pharmacodynamic (concentration–effect) components. The concentration provides a link between pharmacokinetic and pharmacodynamic domains: It is the target quantity for standard dose assignments. The three primary processes of pharmacokinetics are absorption, distribution, and elimination.



## Chapter 2

### Characterizing the individual response to medical treatment

This chapter is devoted to presenting a selection of methods that we have developed to analyze different types of experimental data, as reported in the relevant medical literature. We shall here discuss their potential interest when aiming at quantifying the individual response to a specific medical treatment.

In the first section a deterministic model for the kinetics of tramadol is introduced. The model represents an example of a focused modelization grounded on the specific mechanisms which are essential elements of the dynamics of tramadol. As we shall see, by adjusting the theoretical curves to the experimentally measured concentrations, one can access an estimate of the chemical parameters which are then critically evaluated with reference to the metabolic profiles of the patients. The final aim of our work is to eventually obtain a quantitative indication on the required initial dose amount as a function of the phenotypic profile associated to the polymorphisms of CYP2D6.

Our deterministic formulation moves from the observation that most of the known polymorphisms of cytochrome CYP2D6 are equipped by a phenotypic metabolic profile. Characterization of other isoforms of cytochrome CYP450, for example the isoform CYP3A4, which metabolizes tramadol, have not yet completely investigated, and only some hypothetical enzyme activity has been reported<sup>1</sup>. It should be emphasized that scientists have been interested in characterizing the cytochrome CYP2D6 because this latter is involved in the metabolization of nearly every drugs. At variance, cytochrome CYP3A4, appears to be active along a few metabolic pathways, and, for these reasons, results less attractive.

Waiting for a detailed characterization of the cytochrome, one could, in principle, try to clusterize the genetic polymorphisms in order to hypothesize similarities in the corresponding enzyme activity. Standard clustering algorithm may result too rigid for being applied to this context, where, instead, one would need to dispose of efficient algorithms, suitable for the complex and variable concept of phenotypic distinction. Inspired to this rationale, we have developed an innovative procedure which is able to perform such tasks while resolving intermediate levels of the cluster structures. Section 2.2 presents a detailed account on our implementation. Despite the method is at present not optimized for sorting real data on genetic polymorphisms of human cytochromes, we do believe that it could represent a rather promising starting ground for defining a future platform of data screening.

<sup>1</sup> The reader can compare the updated news relative to CYP2D6 and CYP3A4 at the Human Cytochrome P450 (CYP) Allele home page (<http://www.cypalleles.ki.se>).

The last section of this chapter copes with a common problem of the microarray experiments, namely the missing values problem. The new method that we propose is inspired to analogous developments in the broad field of opinion formation. Shortly, it consists in measuring the distance among records based on the correlations of data stored in the corresponding database.

## 2.1 A comprehensive dynamical approach: Modeling the pharmacokinetics of Tramadol

As introduced in the first chapter, one of the new challenges of the post-genomic era is represented by personalized medicine. This concept arises from the evidence that the same administered dose of drug can result in a wide variability of effects. These differences can be caused by acquired or inherited variability of absorption, distribution, metabolism and excretion of a drug. Pharmacogenetics and pharmacogenomics are emerging fields which aim at processing these information so to develop innovative medical protocols targeted to the individual patient. Pharmacogenetics is in particular concerned with detecting the genetical variability in the metabolism of drugs, which might yield to adverse drug reaction, toxicity or therapeutic failure of pharmacotherapy. Pharmacogenomics techniques are instead meant to isolate new pharmacological agents on the basis of a detailed knowledge of the human genome [32, 33].

As emphasized in section 1.3, any attempt to a personalized pharmacological treatment should account for the pharmacogenetics of the drug metabolism. Many drugs, in fact, undergo a metabolic transformation that produces active metabolites, occasionally more effective than the parent drug. Numerous genetic polymorphisms in drug metabolizing hepatic enzymes have been reported and thoroughly characterized, in particular those belonging to the cytochrome P450 (CYP) superfamily, like cytochrome P450 2D6 (CYP2D6).

Moreover, we have already stressed that the conventional studies on the pharmacokinetics of drugs are often restricted to analyzing the recorded data set on drug concentration, bringing into evidence possible connection with pharmacodynamic aspects, such as the clinical response. These studies are in general not based on a rigorous mathematical modelization, fully justified from first principles. On the contrary, they tend to involve rather approximate formulae which are then benchmarked to the macroscopic traits of the concentration changes over time (e.g. position of the peaks). As we shall clarify in the forthcoming discussion, we here take a different viewpoint by identifying a selection of relevant microscopic processes that constitute the backbone of our formulation. In doing so we aim at resolving, at least partially, the intricate dynamical interplay which drives the evolution of the interacting (chemical) species. This would in turn allow us to match the experimental data via a fitting procedure and so returning a quantitative estimate of the main parameters entering the model. These latter are then inspected as function of the, independently assessed, patient's genetic variability.

Before turning to introduce the model, it is useful to recall again the characteristic of tramadol. Tramadol (hereafter T) is a synthetic opioid, commonly used in the treatment of acute and chronic pain, which is known to be metabolized by CYP2D6. It acts as central analgesic and follows a complex pathway which is not yet fully elucidated [25]. However, it is generally believed that tramadol has a weak affinity with the  $\mu$  opioid receptors, and it works through modulation of the noradrenergic and sero-

tonergic systems. Tramadol is administered as a racemic mixture of two enantiomers, (+)-T and (-)-T, which undergo hepatic metabolism via the cytochromes P450 forming five known metabolites [34]. Among the active ones, O-demethyltramadol (M1) is the most significant since it has 200 times the  $\mu$ -affinity of (+)-tramadol. The isoenzyme responsible for O-demethylation is CYP2D6, that leads to the formation of (+)-O-demethyltramadol ((+)-M1) and (-)-O-demethyltramadol ((-)-M1).

This cascade of reactions results in an underlying network of interactions which is still object of investigations. Once administered, tramadol diffuses in the blood circulation, where about 20% of the drug binds to the plasma proteins. Then tramadol molecules reach the liver where a fraction of it is metabolized by CYP2D6. The remaining amount abandons the liver and follows the circulation flux. The produced metabolites can be released in the circulation or, alternatively, may be further metabolized to secondary metabolites. Bloodstream drives the parent drug and metabolites to reach the target sites where they interact with receptors to produce analgesia. Elimination from the body is mainly due to the kidneys. As we shall see, the mathematical model here developed allows to track the time evolution of the main concentrations.

It is worth mentioning that the applicability of the proposed model extends beyond the case under scrutiny. In fact we here focus on rather general physical (biological) mechanisms that are to be considered as key elements in any grounded pharmacokinetics theory. In this respect our approach is fully predictive and the observed evolution of the concentration amount are reproduced on the basis of selected interaction patterns. This is at variance with previously proposed scenarios [35, 36] where analytical laws for the concentration time curves are a priori guessed.

We will proceed as follow. In section 2.1.1 we provide a short account on 1D spatial diffusion, a fundamental mechanism that certainly drives the process of homogenization and distribution of the drug in the blood. In section 2.1.2 we put forward our model for tramadol administered through an intravenous injection. The model results in a pair of coupled differential equations that govern the self-consistent evolution of tramadol and metabolites. Section 2.1.3 is focused on the validation of the model. First we present the experimental techniques and the measured data and then the theoretical model is fitted versus the measurements. Finally, we draw our conclusions and discuss a quantitative strategy for personalized drug treatment based on our findings.

### 2.1.1 A short account on one-dimensional diffusion

Once the drug is administered, for instance via intravenous infusion, it is transported by the bloodstream and eventually reaches the target tissue. This is a typical passive transport process, the random motion of constituents resulting in a net change of the associated concentration, on a macroscopic level. Diffusion rules the dynamics and thus needs to be properly incorporated into the model. We will here review some fundamental aspects of diffusion theory that we shall further elaborate in the following section to derive a phenomenological entry to the problem of drug transport.

Consider the case of a compound that diffuses along the  $x$  coordinate and suppose the distribution in the  $y - z$  plan to be uniform. We further assume a one-dimensional drifting velocity  $v$  in the  $x$  direction. The concentration at time  $t$  and position  $x$ , here-

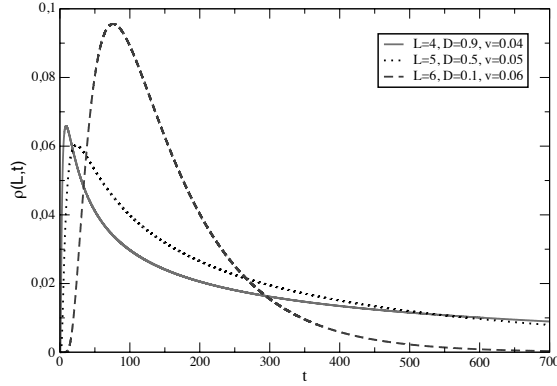


Figure 2.1: The concentration  $\rho(L, t)$  is plotted versus time. Different curves refers to different parameters (see legend). Here  $S_{yz} = 1$ .

after termed  $\rho(x, t)$ , obeys to the following transport equation:

$$\frac{\partial \rho}{\partial t} + v \frac{\partial \rho}{\partial x} = D \frac{\partial^2 \rho}{\partial x^2} \quad (2.1)$$

where  $D$  stands for the diffusion coefficient. The previous equation can be analytically solved, provided one specifies the initial and boundary conditions. For the sake of simplicity we shall here assume that initially ( $t = 0$ ) the diffusing species is spatially located at  $x = 0$ , which, in our setting, ideally corresponds to the injection point. Mathematically, this amounts to require  $\rho(x, 0) = \delta(x)$ , where  $\delta(\cdot)$  stands for the so-called Dirac distribution. Notice that we have implicitly assumed the concentration to be normalized to one. As concerns the boundary conditions, it sounds reasonable to require that the concentration vanishes asymptotically, which formally translates into  $\rho(-\infty, t) = \rho(\infty, t) = 0$ . Under these assumptions, the solution of equation (2.1) reads [37]:

$$\rho(x, t) = \frac{1}{S_{yz} \sqrt{4\pi Dt}} \exp\left(-\frac{(x - vt)^2}{4Dt}\right) \quad (2.2)$$

where the cross-sectional area  $S_{yz}$  of the system in the  $y - z$  plan has been introduced to convert the mathematical solution into real space (i.e. divide by the neglected dimension). Focus now on a specific observation point, located at  $x = L$ , and monitor the time evolution of the concentration  $\rho(L, t)$ . Equation (2.2) leads to:

$$\rho(L, t) = \frac{1}{S_{yz} \sqrt{4\pi Dt}} \exp\left(-\frac{(L - vt)^2}{4Dt}\right). \quad (2.3)$$

In Fig. 2.1  $\rho(L, t)$  is represented versus time, for different choices of the parameters. As expected, the initial concentration is zero. A monotonic growth is subsequently displayed, and corresponds to the intuitive picture that an increasing amount of material finds progressively its way through the check-point at  $x = L$ . A clear peak is observed

when the bulk material reaches the assigned spatial coordinates. The location of the maximum clearly relates to the diffusion properties of the medium ( $D, v$ ) and to the choice of  $L$ . For larger times, the concentration diminishes and eventually fade out asymptotically, as prescribed above.

Interestingly, the profiles reported in Fig. 2.1 bear an intriguing degree of similarity with the typical curves for the time evolution of drug concentration, as reported in a large number of experimental pharmacokinetics studies. This observation reinforces our belief that diffusion is indeed the key mechanism driving the process of drug absorption. In a typical experiment, in fact, the substance is injected at a given location and then visits the intricate network of veins. Blood samples are then drawn from a distinct extraction point, and the operation is repeated at different times. By examining the sample, one hence effectively monitors the time change of the concentration, as seen by a fixed reference control, a setting that closely resembles the scenario discussed above<sup>2</sup>. In reality, blood diffusion occurs in a closed, topologically complex, loop. However, the tramadol data here analyzed do not present any clear evidence of the repeated (peaked) structures that one would expect in presence of a periodic flux [37], thus suggesting that the relevant dynamical process takes place in the time span that encompasses the first passage.<sup>3</sup> To simplify the discussion we shall therefore invoke a simple one-dimensional formulation, directly inspired to equation (2.1). Moreover, as we shall clarify in the following, the diffusion enters the proposed model as an external, time dependent, contribution. This is a minimalist approach that has the merit of enabling us to formulate the dynamics in term of ordinary differential equations, without involving partial derivatives that need to be introduced in the framework of a rigorous description.

### 2.1.2 The mathematical model: Diffusion and time delay

As previously mentioned, the network of tramadol interaction is highly complex and a comprehensive picture that fully accounts for the underlying microscopic processes is still lacking. Here we isolate the main mechanisms in which T is involved, namely, the process of intravenous infusion, the biotransformation in  $M^4$  and elimination, and build up a minimalist formulation which is shown to accurately interpolate the experimental data. A compartmental model is hypothesized and depicted in Fig. 2.2a. These assumptions translate into the following differential equation for the concentration of

<sup>2</sup> Notice that also in the setting where injection and extraction points coincides, the drug has to ideally complete a full circulation tour, following the blood stream, before it can be detected in the sample drawn.

<sup>3</sup> Indeed, the paper by [37] cited above, solves the diffusion equation, in presence of drift, on a circular geometry. Within this setting, the time evolution of the resulting concentration, as measured at a given distance  $L$ , displays multiple peaks, which are originated from successive passages of the drifting pulse. For the case at hand, a direct inspection of the experimental data seems to exclude the existence of recurrent patterns of the type mentioned above. In other words, it can be reasonably assumed that the drug gets dispersed, before the first complete loop is eventually closed up. Under these conditions, there is hence no practical difference in assuming the process to occur on straight line, as we do here, instead of including the details of the relevant periodic geometry.

<sup>4</sup> Here  $M$  incorporates all types of metabolites related to cytochrome CP2D6, including the  $M1$  species for which data are available.

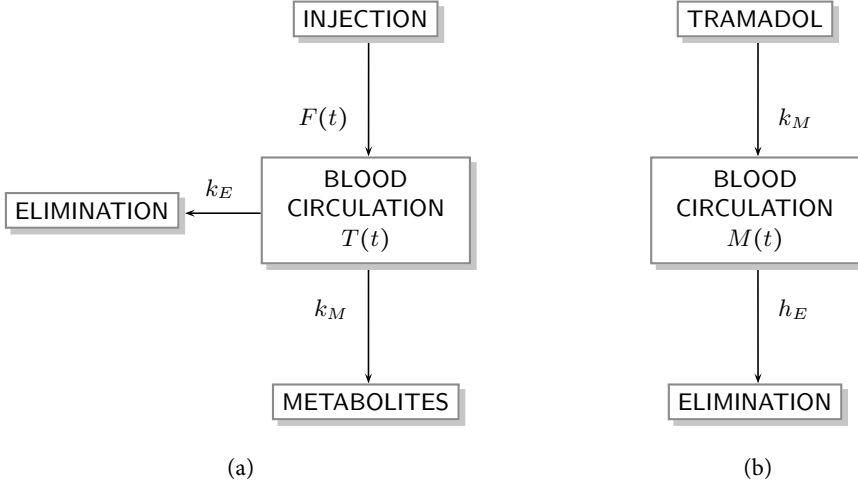


Figure 2.2: Schematic layout of tramadol (a) and metabolite  $M$  (b) dynamics. The local concentration of tramadol in the blood, here labeled with  $T(t)$ , changes as a result of diffusion through the circulation network. The time-dependent term  $F(t)$  is here introduced to account for such diffusive dynamics. The tramadol amount decreases due either to metabolization into  $M$  species (the rate of transformation being here  $k_M$ ) or to generic losses (quantified through the reaction rate  $k_E$ ). The latter include both renal elimination and binding to receptors. The metabolites concentration  $M(t)$  increases, as result of the biotransformation of tramadol. Analogously to the above,  $M$  molecules are expelled by the body or bind to the receptors, thus resulting in an effective loss here controlled by the reaction constant  $h_E$ .

tramadol  $T(t)$ , at the extraction point:

$$\frac{d}{dt}T = -k_M T(t) - k_E T(t) + F(t) \quad (2.4)$$

The term  $k_M T$  denotes the fraction of tramadol metabolized by CYP2D6 in  $M$ , while  $k_E T$  groups tramadol losses due, for instance, to the renal elimination, to the binding of the molecules to receptors and to the formation of the other kind of metabolites.  $F(t)$  is an externally imposed, time-dependent, contribution which effectively mimics the role of diffusion, following the lines of the preceding discussion. The complex network that constitutes the pathway of blood circulation is here mapped into an idealized one-dimensional circuit. Practically, this assumption corresponds to neglect the occurrence of periodic cycles of the diffusing substance, an event that can be excluded upon inspection of the recorded data. Mathematically,

$$F(t) = T_0 \frac{d\rho(L, t)}{dt}$$

where  $\rho(L, t)$  is given by equation (2.3).  $T_0$  labels the administered  $\mu \cdot mol$  of tramadol, thus providing the correct normalization. The drawing are assumed to be instantaneous and therefore we avoid to introduce further corrections to account for the time needed to complete the operation.

Metabolites  $M$  are produced from  $T$ , as schematically depicted in Fig. 2.2b. More specifically, at position  $L$ , we expect to measure an amount of metabolites which represents the net balance between two competing processes. On the one hand, metabolites originates from a fraction of chemically active tramadol molecules, which are not barely transported by the above, purely diffusive, dynamics. On the other hand, metabolites may bind receptors and get also eliminated via the kidney, both mechanisms determining a reduction of the detectable concentration  $M(t)$ . One can hence hypothesize:

$$\frac{d}{dt}M = +k_M T(t - \tau) - h_E M(t) \quad (2.5)$$

where the delay  $\tau$  is here introduced to account for the finite time needed in the chemical conversion from  $T$  to  $M$  species<sup>5</sup>.

Let us now focus again on the explicit expression for  $\rho(L, t)$ . We shall introduce the variables  $\alpha = L/\sqrt{4D}$  and  $\beta = v/\sqrt{4D}$  and recast  $\rho(L, t)$  in the form:

$$\rho(t) = T_0 \frac{\alpha}{V_{Tot} \sqrt{\pi t}} \exp\left(-\frac{(\alpha - \beta t)^2}{t}\right) \quad (2.6)$$

where  $V_{Tot} = S_{yz}L$  represents the total volume associated to the circulation network,  $S_{yz}$  labeling here an averaged estimate of the cross-section surface. In the following we shall fit the above model to a set of experimental data, by properly adjusting the free parameters involved. By choosing the appropriate values that enable for an accurate matching between theory and experiments, we shall obtain a quantitative measure of the kinetic constants and eventually correlate our findings with the typology of patients under scrutiny.

Finally, it should be emphasized that the simple model here discussed does not accommodate for a degree of negative interference among different species, (+)-T, (-)-T, (+)-M and (-)-M, a dynamical effect which arises when competing for available binding sites (receptors). For this reason, we shall proceed with an independent analysis of data relative to the (+)-enantiomers and then to the (-)-enantiomers. The estimated parameters will be labeled with the corresponding symbols preceded by the prefix (+) or (-) (e.g. (+)- $k_M$  stands for the kinetic rate of metabolites production relative to the (+)-enantiomers).

### 2.1.3 Validation of the model

To validate the consistency of the model, we used data from [38]. Here we shall briefly discuss the experiments: The reader can refer to the original publication for further details on the procedures. In particular, we limit our discussion to the intravenous injection setting (termed phase C in [38]). Sixteen healthy volunteers, eight poor metabolizers and eight extensive metabolizers, took part in the clinical trial. The EMs had a median age of 26 years (range 25–28) and a median weight of 78 kg (range 71–85 kg); the PMs had a median age of 25 years (range 22–31) and a median weight of 76 kg (range 65–87 kg). The CYP2D6 phenotype was determined with sparteine and tramadol as probes,

<sup>5</sup> It is worth mentioning that the time delay  $\tau$  is an essential ingredient, which proves crucial to establish a quantitative agreement between theory and experiments.

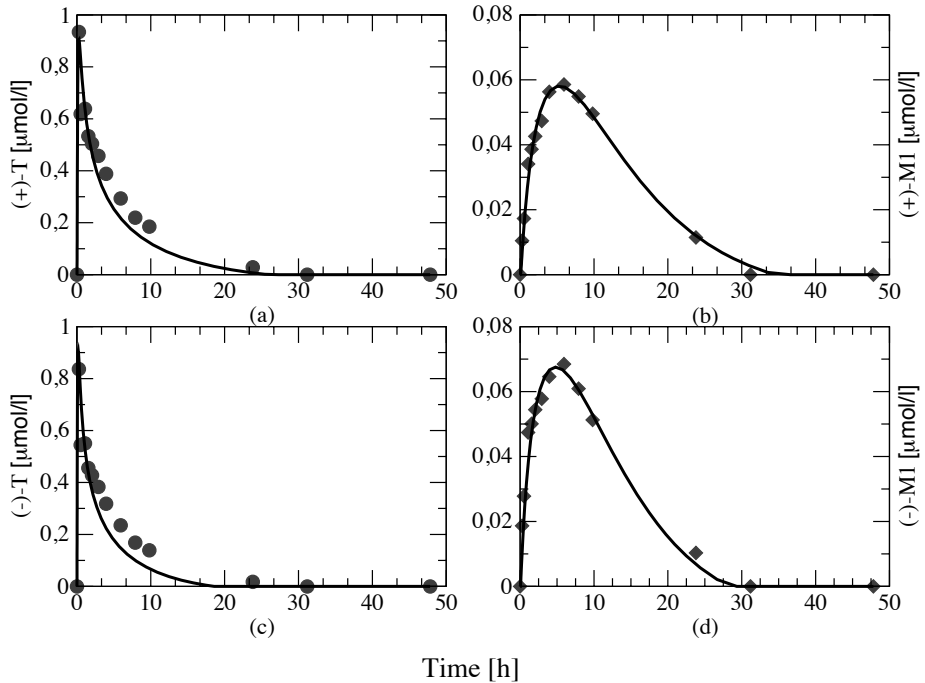


Figure 2.3: Plots of experimental points (symbols) and numerical solution of the model (lines) for an extensive metabolizer. Plot (a) and (b) are relative to (+)-enantiomers, while (c) and (d) refer (–)-enantiomers.

while Taqman technology was used to genotype four selected SNPs: the three known inactivation mutations *CYP2D6*\*3 [39, 40], *CYP2D6*\*4 [41, 42], *CYP2D6*\*6 [43, 44] and the low activity allele *CYP2D6*\*9 [45, 46]. The volunteers received 100 mg tramadol hydrochloride in solution as an intravenous injection. Blood samples were drawn from an intravenous cannula in a forearm vein 0, 1/4, 1/2, 1, 1 1/2, 2, 3, 4, 6, 8, 10, 24, 34 and 48 h after administration. The plasma samples were analyzed by the validated HPLC method [47].

Note that the (+)-tramadol time series from 3 subjects classified as PM were excluded from the analysis. In those cases in fact the metabolites concentration was always found to be zero.

The system of coupled differential equations (2.4) and (2.5) is integrated numerically using the matlab function `dde23`. The latter is designed to solve systems of differential equations with constant delays. In our scheme, the free parameters are tuned so to interpolate the experimental time series for, respectively, the tramadol and metabolite concentrations. A recursive algorithm is hence implemented to minimize an error function, defined as the sum of the differences between the theoretical and experimental curves, weighted according to their peak concentration to ensure a correct balance between the

	Poor metabolizers		Extensive metabolizers	
	mean	SD	mean	SD
(+)- $\alpha$ [ $\sqrt{\text{min}}$ ]	$2.5 \cdot 10^{+0}$	$1.5 \cdot 10^{+0}$	$1.9 \cdot 10^{+0}$	$4.5 \cdot 10^{-1}$
(-)- $\alpha$ [ $1/\sqrt{\text{min}}$ ]	$1.7 \cdot 10^{+0}$	$1.3 \cdot 10^{-1}$	$1.9 \cdot 10^{+0}$	$2.8 \cdot 10^{-1}$
(+)- $\beta$ [ $1/\sqrt{\text{min}}$ ]	$8.1 \cdot 10^{-4}$	$5.4 \cdot 10^{-4}$	$7.9 \cdot 10^{-4}$	$9.0 \cdot 10^{-4}$
(-)- $\beta$ [ $1/\sqrt{\text{min}}$ ]	$1.8 \cdot 10^{-3}$	$2.6 \cdot 10^{-3}$	$1.1 \cdot 10^{-3}$	$1.8 \cdot 10^{-3}$
(+)- $v_{Tot}$ [ $\text{m}^3$ ]	$2.8 \cdot 10^{+1}$	$1.0 \cdot 10^{+1}$	$2.2 \cdot 10^{+1}$	$1.4 \cdot 10^{+1}$
(-)- $v_{Tot}$ [ $\text{m}^3$ ]	$2.2 \cdot 10^{+1}$	$4.5 \cdot 10^{+0}$	$2.4 \cdot 10^{+1}$	$1.4 \cdot 10^{+1}$
(+)- $k_E$ [ $1/\text{min}$ ]	$9.9 \cdot 10^{-4}$	$2.1 \cdot 10^{-4}$	$1.9 \cdot 10^{-3}$	$1.7 \cdot 10^{-3}$
(-)- $k_E$ [ $1/\text{min}$ ]	$2.0 \cdot 10^{-3}$	$1.5 \cdot 10^{-3}$	$2.4 \cdot 10^{-3}$	$2.8 \cdot 10^{-3}$
(+)- $k_M$ [ $1/\text{min}$ ]	$3.7 \cdot 10^{-5}$	$2.0 \cdot 10^{-5}$	$5.2 \cdot 10^{-4}$	$2.8 \cdot 10^{-4}$
(-)- $k_M$ [ $1/\text{min}$ ]	$3.5 \cdot 10^{-4}$	$1.5 \cdot 10^{-4}$	$8.7 \cdot 10^{-4}$	$4.0 \cdot 10^{-4}$
(+)- $h_E$ [ $1/\text{min}$ ]	$1.9 \cdot 10^{-3}$	$1.6 \cdot 10^{-3}$	$1.4 \cdot 10^{-3}$	$1.4 \cdot 10^{-3}$
(-)- $h_E$ [ $1/\text{min}$ ]	$1.1 \cdot 10^{-3}$	$9.0 \cdot 10^{-4}$	$2.0 \cdot 10^{-3}$	$1.9 \cdot 10^{-3}$

Table 2.1: Average and associated standard deviation of the main parameters as obtained from the numerical fitting procedure. The (+) and (-) labels that precede the parameter symbol recall that values are calculated either from the (+)-enantiomers or the (-)-enantiomers experimental data set. Notice that the parameters  $\alpha$  and  $\beta$  bear no immediate interpretation, being merely rescaled quantities introduced to simplify the fitting scheme.

two contributions<sup>6</sup>. The values of the parameters  $\alpha$ ,  $\beta$ ,  $V_{Tot}$ ,  $k_M$ ,  $h_E$  and  $k_E$  are updated until convergence. The procedure is repeated for different values of the time delay<sup>7</sup>  $\tau$  and the final global error monitored: The value of  $\tau$  that results in the smallest deviation is selected, and the corresponding set of fitted parameters stored. For each patient, one can therefore access an estimate of the constants that control the process of kinetics of (+)-tramadol (resp. (-)-tramadol) and (+)-metabolites (resp. (-)-metabolites). This procedure results eventually in quantitative estimates for the fitted parameters. Average of the best fit values for the classes here considered are enclosed in Tab. 2.1 together with the associated error.

In Fig. 2.3 we report a visual comparison between measured points (symbols) and theoretical profiles (solid lines). The curves refer to an extensive metabolizer and clearly confirm the adequacy of the proposed scenario.

The rates of metabolization and elimination play an important role in the kinetic of tramadol. A statistical analysis over a large population of patients would certainly contribute to shed light onto the crucial differences among PMs and EMs categories, and possibly to reveal the relative importance of the microscopic processes involved. Despite the fact that the statistical ensemble here analyzed is limited, we are however in a position to draw some general conclusion.

Figure 2.4 reports the  $k_M$  values as resulting from the above fitting procedure for respectively (a) the (+)-enantiomers experimental data, and (b) the (-)-enantiomers

<sup>6</sup> The code is constructed in matlab and can be made available upon request. The matlab function *fminsearch* is used to perform an unconstrained nonlinear minimization (Nelder-Mead).

<sup>7</sup> The minimal change in  $\tau$  occurs in step  $10^{-4}$ . The best fit value results  $\tau = 0.001$  for all analyzed cases.

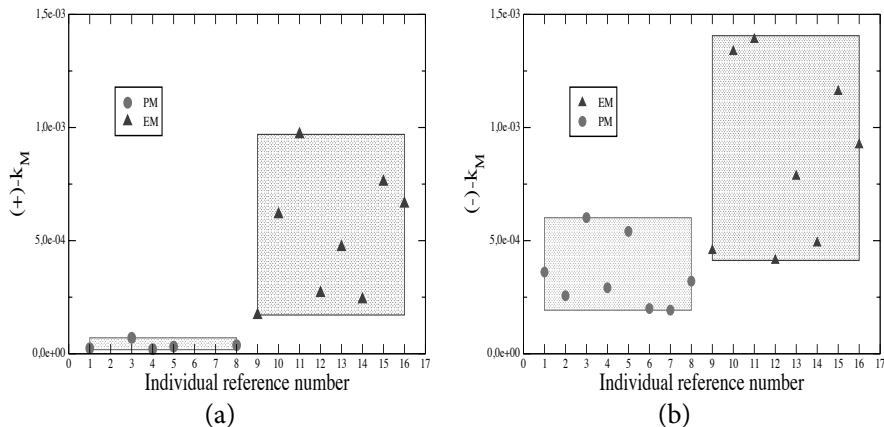


Figure 2.4: Values of  $k_M$  obtained from numerical fit. Panel (a) refers to the (+)-enantiomers experimental data ((+)- $k_M$ ), while panel (b) to the (-)-enantiomers ((-)- $k_M$ ). The wire-framed rectangular patches define the region spanned by the data and it is solely drawn as a guide for the eye.

data. The parameters  $k_M$  are plotted vs an integer number that labels the individual.

Figure 2.4a displays a clear clusterization tendency of  $k_M$ : The two groups of subjects segregate, the extensive metabolizers being associated to a sensibly larger value of  $k_M$ . More quantitatively, the rate of metabolization in EMs is about 10 times greater than the corresponding analogue in PMs. This result agrees with the intuitive picture that the main difference between PMs and EMs is the ability to metabolize the drug. As clearly testified in Fig. 2.4b, such difference is less pronounced for (-)-T: The data cover patches which are only approximately disjoint. This finding points to the fact that biotransformation of tramadol varies within the phenotypic population of extensive metabolizers depending on the genotype of CYP2D6 [48]. In order to obtain the evidence of a more clustered distribution, one should probably enhance the statistics, i.e. accessing a larger set of experimental data.

Notice that the above scenario is compatible with the scores of the t-Test. The null hypothesis, i.e. the assumption that the means relative to the compared ensembles are identical, is in both cases rejected, but with different p-values: The value associated to the (+)- $k_M$  data set (0.003), is lower than the one extracted from (-)- $k_M$  (0.007). This in turn implies that in the former case poor and extensive metabolizers are more clearly trackable to independent portions of the parameter space.

Importantly, having accessed a quantitative estimate of the metabolization rate  $k_M$  might enable us to define a therapy protocol which is tuned on the genetic profile of the patient. According to [49] in fact (+)-M1 molecules display higher affinity for the  $\mu$  opioid receptor, being about 700-fold more potent than the affinity measured for ( $\pm$ )-tramadol. In this respect, metabolites molecules, simply  $M$  in the present discussion, seem to result in more effective chasers of target receptors, when compared to their tramadol analogue. It can be consequently argued that the metabolite concentration in the blood is to be maximized, so to enhance the chances of a persistent and sensible

screening of the available receptor sites. Following this line of reasoning, we set down to calculate the initial dose of tramadol that is required to produce the same amount of metabolites in PMs and EMs individuals. To this end, we now disregard the transport of the drug<sup>8</sup> and restrict ourselves to a linearized version of the proposed model. For relatively short times  $t$  (tens of minutes), the metabolite quota  $M$  scales approximately as  $k_M T_0 t$ , a formal relation which holds for both EMs and PMs patients with, respectively,  $k_M = k_M^{EM}$  and  $k_M = k_M^{PM}$ . Using the values reported in the Tab. 2.1<sup>9</sup>, one immediately deduces an estimate for the relative dose of tramadol administered to EM and PM subjects, which is required to produce an identical concentration of metabolites, at a generic time  $t$ . More specifically, labeling with  $T_0^{EM}$  (resp.  $T_0^{PM}$ ) the initial dose prescribed to EMs (resp. PMs), yields:

$$T_0^{PM} \simeq 14T_0^{EM} \quad (2.7)$$

for (+)-enantiomers and

$$T_0^{PM} \simeq 2.5T_0^{EM} \quad (2.8)$$

for (–)-enantiomers<sup>10</sup>. This conclusion quantifies the importance of including information on the kinetics of the two enantiomers when planning for personalized drug therapy. It is however worth emphasizing that the above conclusions are reached on the basis of a rather limited set of case studies. Increasing the number of patients, so to enhance current statistics, represents a crucial leap forward, when aiming at confirming the correctness of our findings<sup>11</sup>.

Moreover, we can speculate on the difference between (+)- $k_M$  and (–)- $k_M$ . Acting as an index of metabolization,  $k_M$  can be associated to stereoselective property of O-demethylation in favour of (–)-tramadol. In *in vitro* experiments O-demethylation of tramadol was determined to be greater for the (–)-enantiomer than for the (+)-enantiomer [50]. Our analysis indicates that (–)- $k_M$  is always greater than (+)- $k_M$  in every subject. This result confirms therefore the above scenario, thus providing an indirect evidence for the stereoselective property of O-demethylation.

The distribution of  $h_E$  is rather sparse. The values of (+)- $h_E$  range from  $3.1 \cdot 10^{-4}$  to  $3.2 \cdot 10^{-3}$ , while (–)- $h_E$  ranges from  $3.5 \cdot 10^{-4}$  to  $4.5 \cdot 10^{-3}$ . An exception is detected for subject 12, whose values of (+)- $h_E$  and (–)- $h_E$  are close to zero. This may correspond to a slow process of elimination, or can be alternatively interpreted invoking a low affinity of the M molecules to the receptors.

For what concerns  $k_E$ , we could not identify a significant difference between poor and extensive metabolizers: (+)- $k_E$  is found in the interval  $[7.3 \cdot 10^{-4}, 3.6 \cdot 10^{-3}]$ , while (–)- $k_E$  scans  $[3.4 \cdot 10^{-5}, 6.7 \cdot 10^{-3}]$ . For subjects 11, 13 and 16 we found instead (+)- $k_E \simeq$

<sup>8</sup> The latter is instead a crucial ingredient when aiming at extract an estimate of the kinetic constants involved via numerical fit of the experimental data.

<sup>9</sup> As documented in Tab. 2.1, the (+)-enantiomers (resp. (–)-enantiomers) case corresponds to  $k_M^{EM} = (5.2 \pm 2.8) \cdot 10^{-4}$  (resp.  $k_M = k_M^{EM} = (8.7 \pm 4) \cdot 10^{-4}$ ) and  $k_M = k_M^{PM} = (3.7 \pm 2) \cdot 10^{-5}$  (resp.  $k_M = k_M^{EM} = (3.5 \pm 1.5) \cdot 10^{-4}$ ).

<sup>10</sup> In both case the error on the estimated ratio  $T_0^{PM}/T_0^{EM}$  is less then 5%.

<sup>11</sup> It should be again stressed that the above conclusion are reached by putting forward several simplifying assumptions (small time regime, disregard the role of diffusion) which could in principle heavily reflect on the final outcome. The estimated dose falls however within a reasonable range as e.g reported in <http://en.wikipedia.org/wiki/Tramadol>.

0 and for subjects 3, 9, 11 and 16(  $-$ )- $k_E \simeq 0$ . We here recall that the term  $k_E$  controls the fraction of tramadol that binds to receptors, the quota eventually eliminated and the amount which is metabolized into other types of metabolites. To gain a comprehensive understanding on the overall process, and interpret these findings, it would be crucial to access the nociception and look for positive correlation with the low affinity of tramadol with receptors.

Furthermore, we notice from Tab. 2.1 that, as expected, the entries relative to  $\alpha$ ,  $\beta$  and  $v_{Tot}$  are rather sparse, the latter being essentially related to diffusion and transport properties.

As a possible extension of the current work, we plan to develop a more detailed scheme of reactions that includes the distinction between (+)-enantiomers and (-)-enantiomers. Moreover, we stress the importance of incorporating into the theory the competition of (+)-T, (-)-T, (+)-M, (-)-M for the receptors' binding sites, so to reproduce the difference in affinity that have been reported in experiments [49, 25]. Another interesting extension concerns constructing a realistic, compartment-based model: This latter could eventually allow for a proper inclusion of the relevant diffusive mechanism, here incorporated via an effective term.

Finally, we emphasize that M1 is just one out 23 known metabolites [51]. It would be therefore important to enrich the analysis by disposing at least of data relative to the second active metabolite produced through an hepatic cytochrome, namely N-desmethyltramadol (M2). To this end, it would be particularly attractive to perform experiments aimed at registering the concentration of T, M1, M2, for patients whose genotype has been determined, and monitor, at the same time, the perception of pain.

In conclusion, as outlined above, the phenotype plays an important role in determining the optimal medical strategy. However a complete characterization of the enzymatic activity and its relation with the genetic polymorphisms are far to be fully clarified. More extensive investigations are needed to gain a comprehensive understanding of the whole process. In the long run one will eventually dispose of a large gallery of complementary information. Processing this information clearly implies developing robust and reliable methods for their classification. Clusterization algorithms constitute a viable tool, which certainly deserve further analysis. In the following section we shall discuss a novel procedure that we have outlined to perform such a delicate operation.

## 2.2 Unbiased tools for data processing: Emergence of homogeneous clusters

Cluster analysis is used to classify a set of items into two or more mutually exclusive groups based on combinations of internal variables. The goal of cluster analysis is to organize items into groups in such a way that the degree of similarity is maximized for the items within a group and minimized between groups.

The need of data clustering is common in many problem. In particular, we can consider an abstract system represented as an unweighted graph, composed of  $N$  nodes. The nodes are connected by a variable number of links. A set of nodes is considered a cluster if, *in some sense*, the nodes belonging to it are *more connected* among them rather than among the rest of the system.

The previous statement is rather vague: it is in fact very rare that one can unambiguously identify an isolated cluster. In general, one needs to impose a cut-off, and therefore the cluster structure has a certain degree of arbitrariness. If one knows with

a sufficient precision the model underlying data generation, and therefore the expected data distribution, then the problem of clustering reduces to the minimization of distance between the measured and expected distribution, using the cluster number, coordinates and size as tuning parameters. In general, however, this is not possible, and so generic methods can only give a range of possible clusters, according to the variation of a given parameter. When there are extended regions of the parameters for which the cluster structure is stable, one may say that, for a given “coarse graining”, there is clustering. Let us consider the case of an adjacency matrix, with blocks with a given probability of ones (links) along the diagonal, and a smaller probability outside. Let us call these probabilities  $p_1$  and  $p_2$ , respectively. In the case  $p_2 = 0$  and  $p_1$  sufficiently high (above a percolation threshold), the only clusters are those linking the nodes in the block. However, as soon as  $p_2 > 0$ , there are links connecting the previous clusters. In the limit of infinite sizes of the blocks, one gets a clear distinction between blocks, but for finite systems, and without the possibility of performing ensemble averaging, fluctuations may well cause a site to be more linked to a “wrong” cluster than to the “right” one. In any case, even in the most ideal scenario, there is a certain degree of arbitrariness in deciding that the blocks form clusters. The situation is obviously worse when there is a continuum variation of the density of links.

Most of clustering methods rely on performing walks on the graph, marking visited nodes or links, and measuring graph-distances. This is a rather heavy task, especially for large graphs. More efficient algorithms are probably those not based on path counting. Among these, one of the most promising clustering method in bioinformatics is the Markov Cluster Algorithm (MCL). Although this method is rather effective and really simple to implement, it lacks a precise physical meaning.

Starting from MCL, we developed a new method based on a biological background. More precisely, we are interested in how to find community structures with patches of populations in competition. We choose to refer to this method as to Ecological Clustering (EC).

In the next section we briefly describe the Markov Cluster Algorithm, while in the last one we introduce our model and compare it with MCL.

### 2.2.1 Markov cluster algorithm

The Markov Cluster algorithm (MCL) is a method to find community structure developed by Stijn van Dongen in his PhD thesis [52]. The algorithm essentially simulates a process of diffusion on a graph. It works alternating two operations called expansion and inflation, on a  $N \times N$  transition Markov matrix  $T$  obtained by dividing each element  $C_{ij}$  of the adjacency matrix by the degree of node  $j$ . The element  $T_{ij}$  of the stochastic matrix represents the probability that a random walker goes from node  $i$  to node  $j$ . In the first step, the left stochastic matrix of the graph is squared, so that every element of the resulting matrix gives the probability that a random walker, starting from node  $i$ , reaches  $j$  in 2 steps. The second step consists in raising each single entry of the matrix  $T$  to some power  $\alpha$ , where  $\alpha$  is a real value. This operation, called inflation, increases the weights between pairs of vertices with large values of the diffusion flow, which therefore have a high probability to belong to the same community. The final step is to divide each element of every column by their sum, such that the sum of the elements of the column equals one and a new stochastic matrix is recovered. The

corresponding algorithm for MCL is the following:

$$\begin{aligned} T_{ij}(0) &= \frac{C_{ij}}{\sum_k C_{kj}} \\ \tilde{T}(t + \Delta t) &= T(t)^2 \\ T_{ij}(t + \Delta t) &= \frac{(\tilde{T}_{ij}(t + \Delta t))^\alpha}{\sum_k (\tilde{T}_{kj}(t + \Delta t))^\alpha} \end{aligned}$$

After some iterations, the process converges to a stationary matrix whose elements are either zero or one. According with the value of  $\alpha$ , the graph represented by this matrix may be disconnected, and in this case its connected components are the communities of the original graph. Practically, the clusters are the few lines with some nonzero elements. The final partition is clearly dependent of the parameter  $\alpha$  used in the inflation step. Therefore the method may converge to several different partitions and there is no way to decide which are the most meaningful or representative.

### 2.2.2 Ecological clustering

Our idea is to develop an algorithm to find community structure based on a biological approach. In particular we start from a very simple model for the selection process of two species labeled A and B. We hypothesize that the number of elements of each populations, denoted by  $x$  and  $y$  respectively, obey to

$$\begin{aligned} \dot{x} &= ax^c - \phi x \\ \dot{y} &= by^c - \phi y \end{aligned} \quad (2.9)$$

where  $a$  and  $b$  denote the fitness value of A and B, while  $\phi$  is a density limitation that keeps the total population  $x + y$  constant. The exponent  $c$  is the parameter which quantifies the non-linearity of the growth. It is easy to show (see for example [53]) that for  $c < 1$  there is a stable mixed equilibrium between A and B even if one population is characterized by a growth rate bigger than the other one. For  $c > 1$  there is an unstable mixed equilibrium between A and B, and the case where only one population is present is stable. This means that if, for example, the space is populated only by species A, B cannot invade also if it has a higher growth parameter.

We are interested in investigating what happens if we simulate a similar scenario on an undirected graph with  $N$  nodes, where every node has enough room for  $N$  different species, all with the same fitness. Denote by  $P_{ij}(t)$  the probability that at time  $t$  in the  $i$ -th node there is the  $j$ -th specie. We initialize the graph populating each node  $i$  with only individuals of species  $i$ , namely  $P_{ij}(0) = 0 \quad \forall i \neq j$  and  $P_{ii}(0) = 1$ . Without any interaction among individuals, we can hypothesize a simple rule: At each time step the algorithm is based on two processes, namely diffusion and selection. During the process of diffusion, in each node  $i$  a fraction  $p$  of individuals decides to emigrate, where  $p \in \mathbb{R}$  and  $0 \leq p \leq 1$ . They choose a link  $l$  according to  $C_{ij} / \sum_l C_{il}$ , where  $C$  is the adjacency matrix, and move to that node. The other  $1 - p$  fraction of individuals remains in the original node. Then a new selection phase takes place, since nodes that received more than  $N$  individuals are pruned, and nodes with less than  $N$  individuals are repopulated

by reproduction. This mechanism translates into the following algorithm:

$$\begin{aligned}
 Q_{ij}(t + \Delta t) &= (1 - p)P_{ij}(t) + p \sum_l \frac{C_{il}P_{lj}(t)}{\sum_k C_{kl}} \\
 P_{ij}(t + \Delta t) &= \frac{(Q_{ij}(t + \Delta t))^\alpha}{\sum_j (Q_{ij}(t + \Delta t))^\alpha}
 \end{aligned}$$

Therefore, in the EC method we have two parameters, exponent  $\alpha$  and diffusion  $p$ . Time also could be considered a parameter, since the convergence to the asymptotic status is enough slow that several structures appear during relaxation. However, here we concentrate only in the asymptotic state.

To test this model and to compare it with MCL, we followed the idea described in [54] and we applied the algorithms to a network with a known fixed community structure. For this purpose, we generated a network with  $N = 128$  nodes, split into four communities containing 32 nodes each. Pairs of nodes belonging to the same community are linked with probability  $p_{in}$ , while pairs belonging to different communities are joined with probability  $p_{out}$ . The value of  $p_{out}$  is taken so that the average number of links a node has to members of any other community,  $z_{out}$ , can be controlled. While  $p_{out}$  (and therefore  $z_{out}$ ) is varied freely, the value of  $p_{in}$  is chosen to keep the total average node degree,  $k$ , constant, and set to 16.

Instead of focussing only in correctly classifying the nodes, we preferred to put attention on the ability to detect different levels of clusterization. For this reason, we did not test the sensitivity of the two algorithms measuring the quantities suggested in [54], but we preferred to monitor the entropy.

We defined the entropy  $S(t)$  as

$$S(t) = -\frac{\sum_k z_k \ln z_k}{\ln N}$$

where  $z_k(t)$  is the global distribution of  $k$ -th specie, namely  $z_k(t) = \sum_j T_{kj}/N$  for MCL and  $z_k(t) = \sum_i P_{ik}/N$  for our model.

The entropy  $S(t)$  of both methods converges to a stationary level that assumes values between 0 and 1. The steady state of entropy is 0 when only one big community is detected, while it is 1 when every node is classified as a single cluster.

Fig. 2.5 shows the stationary entropy as function of the exponent  $\alpha$ , relative to the two model tested on networks with different  $p_{out}$ . As we can see from this Fig. the MCL algorithm seems to work in a standard way. We can observe that there are two critical values,  $\alpha_1$  and  $\alpha_2$  that identify the regions in which the method finds different number of communities. More precisely, MCL converges to a single cluster for  $1 < \alpha < \alpha_1$ , it finds four clusters for  $\alpha$  between  $\alpha_1$  and  $\alpha_2$ , and it detects 128 communities for  $\alpha > \alpha_2$ . Even though  $\alpha_1$  and  $\alpha_2$  depend on the characteristics of the network, usually  $\alpha_1 \simeq 1.5$  and  $\alpha_2 \simeq 2$ . It is interesting to notice that in this case, the parameter  $\alpha$  acts as the parameter  $c$  in model (2.9): The value  $\alpha = 1$ , like  $c = 1$ , is a critical value which separates the region which leads to a stable mixed equilibrium among the species (128 clusters), to the one where other equilibrium configurations are allowed.

Although some of the previous features may be found also in our model, the EC algorithm exhibits an important difference. In fact we can notice that the stationary

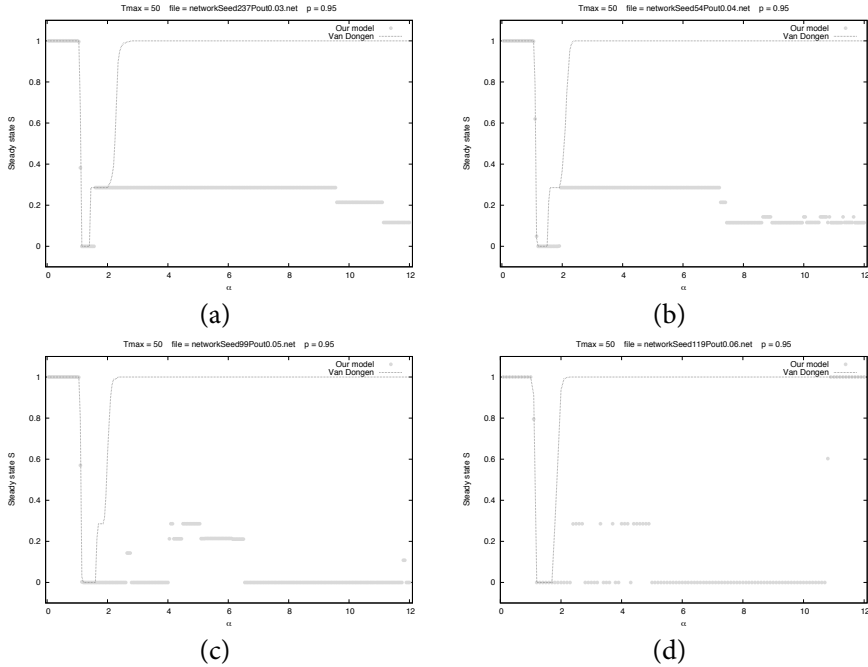


Figure 2.5: Steady state of entropy  $S$  as function of the parameter  $\alpha$ . Cyan dots are points relative to our model, while the magenta lines refer to the van Dongen's model. For the plot in panel (a) we used a network with  $p_{out} = 0.03$ , in panel (b)  $p_{out} = 0.04$ , in panel (c)  $p_{out} = 0.05$  and in the last panel  $p_{out} = 0.06$ . In all cases, we used  $p = 0.95$ .

values of the entropy are not only three as for the MCL. Consider, for example, Fig. 2.5b. The entropy relative to our model follows the behavior of MCL only for small values of  $\alpha$ . As  $\alpha$  increases the entropy does not reach the boundary value 1 but assumes mostly two values, namely 0.1 and 0.28. To visualize how entropy is related to the final structure of communities, we can have a look at Fig. 2.6. This figure reports the stationary state of the network and the communities found by the two algorithm, for the same parameters of Fig. 2.5b, but with different values of  $\alpha$ . The blue dots are the final structure of the network, while the continuous vertical red segments and the continuous horizontal green segments identify the communities found by EC and van Dongen's method respectively. We can see that while the MCL converges essentially to three kinds of structures (one big cluster, 128 single clusters, and four clusters), the EC algorithm is able to detect intermediate clusters. In conclusion we can say that the main feature of EC algorithm is the ability to recognize different levels of clusterization. These levels are found monitoring the behavior of the entropy.

In many applications bioinformatics deals with another crucial problem, the so called missing data problem. This is reviewed in the following where a possible approach to overcome its limitations are discussed.

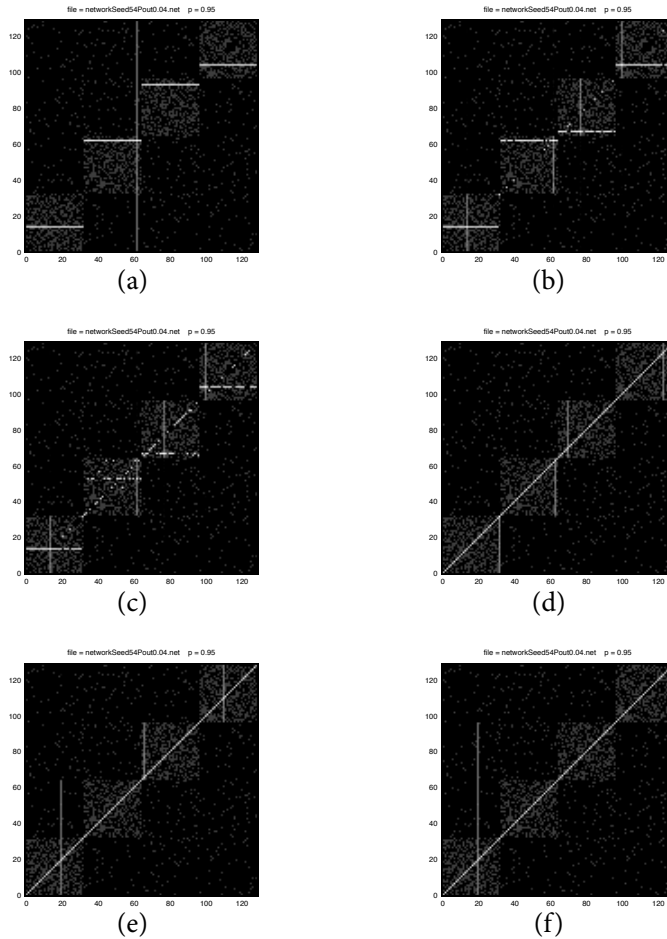


Figure 2.6: Blue dots represent the stationary structure of the network, green segments are communities detected by the van Dongen algorithm, while the red segments are the ones found with EC model. All plots refers to the same network generated with  $p_{out} = 0.04$ , while  $\alpha$  varies. In panel (a)  $\alpha = 1.9$ , in panel (b)  $\alpha = 2.0$ , in panel (c)  $\alpha = 2.1$ , in panel (d)  $\alpha = 4.0$ , in panel (e)  $\alpha = 7.4$  and in the last panel  $\alpha = 8.0$ .

### 2.3 The problem of missing data: Filling the gaps

As introduced in section 1.5 a DNA microarray is a collection of microscopic DNA spots of probes, commonly complementary to some region of a gene, arrayed on a solid surface by covalent attachment to a chemical matrix. DNA arrays are commonly used for expression profiling, namely monitoring expression levels of thousands of genes simultaneously, or for comparative genomic hybridization. Despite their wide use, gene expression microarray experiments, frequently generate data sets with multiple missing expression values. This may be due to a production flaw, a mistake during the sensible procedure of preparation, or the final image may be corrupted or may have an insufficiently resolution. Some researchers overcome the problem proceeding with the analysis omitting missing values and data relative to suspected spots, like spots with dust particles, irregularities or other bad features.

The presence of missing values implies loss of information, and the practice to ignore this would lead to an unbalanced experimental design. Moreover, many algorithms for gene expression analysis require a complete matrix of gene array values as input, and may lose effectiveness even with a few missing values.

Methods for imputing missing data are needed, therefore, to minimize the effect of incomplete data sets on analyzes, and to increase the range of data sets to which these algorithms can be applied [55]. Moreover, comparison between a “forecasted” value based on correlations in the dataset, and the measured one, can be considered a consistency “check” of the dataset itself.

Here we propose a new method for inferring missing data which takes the cue from the field of opinion formation. In opinion formation, one can assume that one’s opinion on a certain item is given by the characteristics of the item, weighted by individual “tastes”. The tastes result from past experiences, but they do not change abruptly from time to time. In principle, tastes can be decomposed into independent “dimensions”. It is rather difficult to identify such dimensions, as testified by the limited success of market campaigns. However, it can be shown [56] that exploiting the correlations among the expressed opinions, it is possible to deduce the distance between the tastes of two individuals.

We start from the original method described in [56] to derive a new way for measuring the distance among records based on the correlations of data stored in the corresponding database entries. In this work the opinions expressed over a set of topics originate a “knowledge network” among individuals, where two individuals are nearer the more similar their expressed opinions are. Assuming that individuals’ opinions are stored in a database, the authors show that it is possible to anticipate an opinion using the correlations in the database. This corresponds to approximating the overlap between the tastes of two individuals with the correlations of their expressed opinions. Here we extend this model to nonlinear matching functions, inspired by biological problems such as microarray (probe–sample pairing). We investigate numerically the error between the correlation and the overlap matrix for eight sequences of reference with random probes. Results show that this method is particularly robust for detecting similarities in the presence of translocations.

Let us first illustrate the problem summarizing the main results reported in [56]. Consider a population of  $M$  individuals experiencing a set of  $N$  products. Assume that each product is characterized by an  $L$ -dimensional array  $\mathbf{a} = (a^{(1)}, a^{(2)}, \dots, a^{(L)})$  of

features, while each individual has the corresponding list of  $L$  personal tastes on the same features  $\mathbf{b} = (b^{(1)}, b^{(2)}, \dots, b^{(L)})$ . The opinion of individual  $m$  on product  $n$ , denoted by  $s_{m,n}$ , is defined proportional to the scalar product between  $\mathbf{b}_m$  and  $\mathbf{a}_n$ :  $s_{m,n} = \lambda(L) \mathbf{b}_m \cdot \mathbf{a}_n$ , where  $\lambda(L)$  is a suitably chosen normalization factor. In general,  $\lambda(L)$  should scale as  $L^{-1}$  and depend on the ranges of  $\mathbf{a}$  and  $\mathbf{b}$ .

In order to predict whether the person  $j$  will like or dislike a certain product  $\mathbf{a}_n$ , assuming to know  $\mathbf{a}_n$ , it is sufficient to obtain the individual tastes of that individual, i.e. the vector  $\mathbf{b}_j$ . The similarity between tastes of two individuals  $i$  and  $j$  is defined by the overlap  $\Omega_{ij} = \mathbf{b}_i \cdot \mathbf{b}_j$  between the preferences  $\mathbf{b}_i$  and  $\mathbf{b}_j$ .

One can build a knowledge network among people, using the vectors  $\mathbf{b}_m$  as nodes and the overlaps  $\Omega_{ij}$  as edges. Maslov and Zhang [57] (MZ) assume that a fraction  $p$  of these overlaps are known. They show that there are two important thresholds for  $p$  in order to be able to reconstruct the missing information. The first one is a percolation threshold, reached when the fraction of edges  $p$  is greater than  $p_1 = 1/M - 1$  where  $M$  is the number of people. This means that there must be at least one path between two randomly chosen nodes, in order to be able to predict the second node starting from the first one.

Since vectors  $\mathbf{b}_n$  lie in an  $L$  dimensional space, and a single link ‘‘kills’’ only one degree of freedom, a reliable prediction needs more than one path connecting two individuals. Maslov and Zhang show that there is a ‘‘rigidity’’ threshold  $p_2$ , of the order of  $2L/M$ , such that for  $p > p_2$  the mutual orientation of vectors in the network is fixed, and the knowledge of the preferences of just one person is sufficient to reconstruct those of all the other individuals.

In general one does not have access to individuals’ preferences, nor one knows the dimensionality  $L$  of this space. In order to address this problem, the authors define the correlation  $C_{ij}$  between the opinions of agents  $i$  and  $j$  by

$$C_{ij} = \frac{\sum_{n=1}^N (s_{in} - \bar{s}_i)(s_{jn} - \bar{s}_j)}{\sqrt{\sum_{n=1}^N (s_{in} - \bar{s}_i)^2 \sum_{n=1}^N (s_{jn} - \bar{s}_j)^2}}, \quad (2.10)$$

where  $\bar{s}_i$  is the average of the opinion matrix  $S$  over column  $i$ . The elements  $C_{ij}$  can be conveniently stored in a  $M \times M$  opinion correlation matrix  $C$ .

One can compute an accurate opinion anticipation  $\tilde{s}_{mn}$  of a true value  $s_{mn}$  using this formula:

$$\tilde{s}_{mn} = \frac{k}{M} \sum_{i=1}^M C_{mi} s_{in} \quad (2.11)$$

where  $k$  is a factor that in general depends on  $L$  and on the statistical properties of the hidden components. However, if the components of  $\mathbf{a}_n$  and  $\mathbf{b}_m$  are independent random variables,  $k$  is independent of  $n$  and  $m$ , so it can be simply chosen in order to have  $\tilde{s}_{mn}$  defined over the same interval as  $s_{mn}$ .

For large values of  $N$  and  $M$ , the factor  $k$  can be identified with the number of components  $L$ , and obtain an estimate for the average prediction error

$$\varepsilon = \sqrt{\frac{1}{MN} \sum_{mn} (\tilde{s}_{mn} - s_{mn})^2} \simeq \gamma L^{3/2} \frac{\sqrt{M} + \sqrt{N}}{\sqrt{MN}}, \quad (2.12)$$

where

$$\gamma = \lambda(L) \sqrt{\langle a^2 \rangle \langle b^2 \rangle}. \quad (2.13)$$

Formula (2.12) implies that the predictive power of equation (2.11) grows with  $MN$  and diminishes with  $L$ . This fact is a consequence of the decay of the correlations among opinions with  $L$ , so that more amount of information is needed in order to perform a prediction as  $L$  grows. This condition can be compared with the ‘‘rigidity’’ threshold  $p_2$  in the MZ analysis.

### 2.3.1 Test case microarray inspired

In order to investigate the introduction of nonlinearities in the function used to model the process of opinion formation, we considered the case of a microarray.

As mentioned before, microarray experiments can suffer from the missing values, and this fact represents a problem for many data analysis methods, which require a complete data matrix. Although existing missing value imputation algorithms have shown good performance to deal with missing values, they also have their limitations. For example, some algorithms have good performance only when strong local correlation exists in data, while some provide the best estimate when data is dominated by global structure [58].

Here we modified the model described in the previous section to investigate the relationship between the correlation and the overlap between sequences.

To do this we considered an alphabet of four symbols, namely A, T, G, C, corresponding to the four nucleotides that constitute the DNA. We used this alphabet to generate randomly  $M$  sequences of length  $L$  representing the probes of the microarray<sup>12</sup>. Then we generated  $N$  samples of length  $W$  representing the sequences to be hybridized on the microarray.

The correlation  $C_{ij}$  between sample  $i$  and sample  $j$  is defined by

$$C_{ij} = \frac{\sum_{k=1}^M (m_{ik} - \bar{m}_i)(m_{jk} - \bar{m}_j)}{\sqrt{\sum_{k=1}^M (m_{ik} - \bar{m}_i)^2 \sum_{k=1}^M (m_{jk} - \bar{m}_j)^2}} \quad i, j = 1, \dots, N, \quad (2.14)$$

where  $m_{ik}$  is the maximum complementary match between sample  $i$  and probe  $k$  without gaps.

The aim is to test the relationship between the correlation matrix  $C$  and the overlap matrix  $\Omega$  constructed using the following idea of similarity. We hypothesized to infer the similarity between sequences based on the number of subsequences of length  $L$  in common. For this reason we defined the overlap  $\Omega_{ij}$  between sequence  $i$  and sequence  $j$  as the number of subsequences of length  $L$  that appear in the both sequences, divided by  $W - L + 1$  for normalization. This matching function is nonlinear since the effect of a mismatch depends on its position in the subsequence.

To test our hypothesis, we considered eight referential sequences:

**Seq. 0:** This is the first reference sequence, completely random of length  $W$ .

**Seq. 1:** Equal to sequence 0, except for a mutation in the middle (this mimics the Afimatrix central mismatch mechanism for measuring the level of random pairing).

<sup>12</sup> The probes in real microarray are discriminated generally carefully chosen in order to genes of interest.

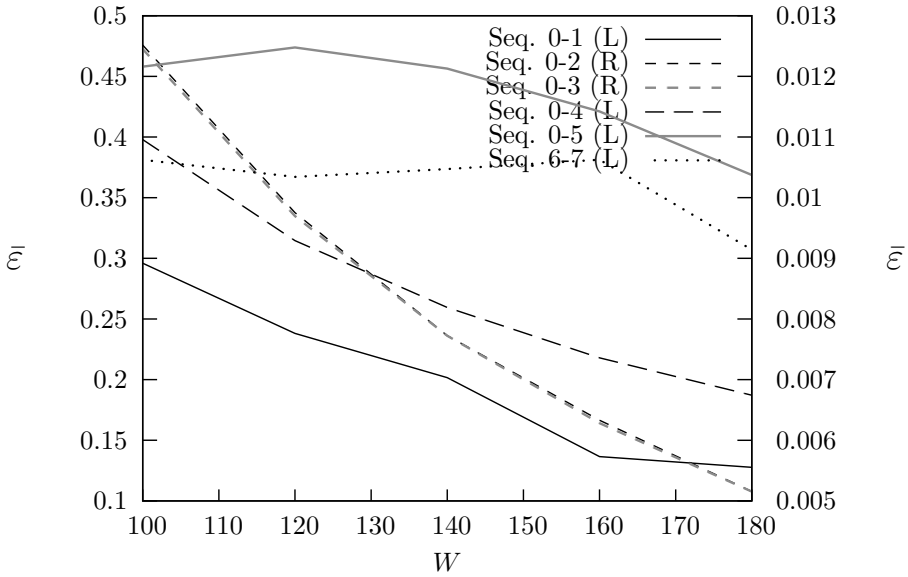


Figure 2.7: The error  $\bar{\varepsilon}$  as a function of the length  $W$  of the samples, averaged over 40 realizations,  $N = 10$ ,  $L = 30$ ,  $M = 500$ . The plots of sequences 0-2 and 0-3 refer to the right y-axis. One can observe that all errors diminish with  $W$ .

- Seq. 2:** Equal to sequence 0, but shifted of one basis.
- Seq. 3:** Equal to sequence 0, with shift and central mutation.
- Seq. 4:** First half of sequence 4 is equal to the second half of sequence 0, and vice versa.
- Seq. 5:** First half of sequence 0 is equal to the second half of sequence 0, the rest is random.
- Seq. 6:** Another reference sequence.
- Seq. 7:** Sequences 6 and 7 contains the same “gene”, of length  $W/3$ , in different positions.

To check the validity of the model described in the previous section, we measured the error  $\varepsilon_{ij}$  for the pair of sequences  $i$  and  $j$  defined as the absolute value of the difference between the correlation and the overlap, namely  $\varepsilon_{ij} = |C_{ij} - \Omega_{ij}|$ . We performed various simulations and then we calculated the average of the error denoted by  $\bar{\varepsilon}$ .

In Fig. 2.7 we plotted the error  $\bar{\varepsilon}$  vs  $W$ . One can see that for all the analyzed cases the error decreases, and this result agrees with those reported in [56] (the parameter  $W$  here corresponds to  $M$  in the opinion formation model).

Figure 2.8 shows the behavior of  $\bar{\varepsilon}$  with respect to  $M$ . The curves are approximately constant, showing that the error is independent of  $M$ .

As one can see from Fig. 2.9, where we plotted the error vs  $L$ ,  $\bar{\varepsilon}$  does not follow a monotonous trend, except for the pair of sequences 0-4 for which the value of  $\bar{\varepsilon}$  is almost constant and next to zero, and for  $\bar{\varepsilon}_{01}$  which increases. For what concerns the

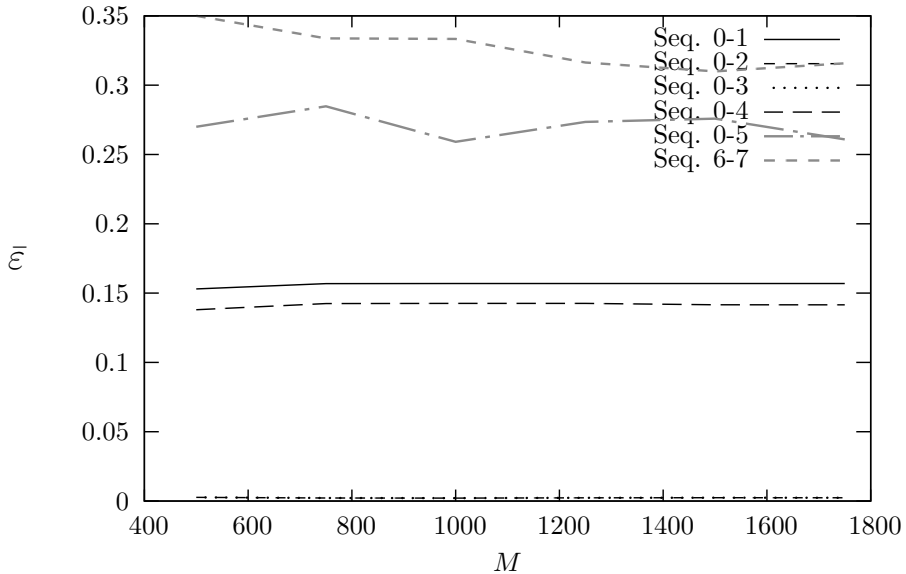


Figure 2.8: The error  $\bar{\epsilon}$  as a function of the number of probes  $M$ , averaged over 40 realizations,  $N = 10$ ,  $L = 20$ ,  $W = 150$ . One can observe that errors do not vary with  $M$ .

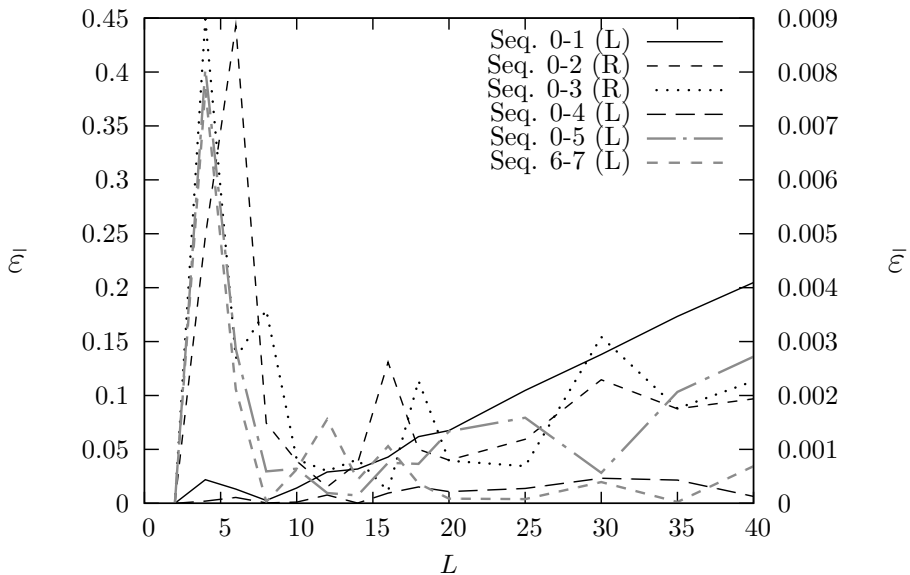


Figure 2.9: The error  $\bar{\epsilon}$  as a function of the length  $L$  of the probes, averaged over 100 realizations,  $N = 10$ ,  $W = 200$ ,  $M = 1000$ . The plots of  $\bar{\epsilon}_{02}$ ,  $\bar{\epsilon}_{03}$  and  $\bar{\epsilon}_{04}$  refer to the right y-axis.

values of  $\bar{\varepsilon}_{02}$ ,  $\bar{\varepsilon}_{03}$  and  $\bar{\varepsilon}_{05}$ , one can detect that the errors decrease until  $L \simeq 10$ , because probes too short can hybridize in many positions without a high specificity. Then they oscillate until  $L \simeq 35$ , and for larger  $L$  the errors increase. This last increase is due to the small coverage of the probes in the sequence space, since we kept the number of sequences  $M$  fixed while the sequence space grows as  $4^L$ .

To sum up, the monitoring of the error for the eight sequences of reference, with respect to  $M$ ,  $W$ , and  $L$ , allows us to assert that the error is low in all cases, decreasing when  $W$  increase, and independent of  $M$ . With respect to  $L$  we find that the model is more robust for traslocation.

In conclusion we can say that the correlation matrix of our model can be used to estimate the distance between sequences. Moreover we point out that the same result can be found following the idea of “negative database”, namely using the subsequences of length  $L$  not in common between two sequences. This idea arises from the antibody-antigens domain which is commonly affected by the missing values problem.

Antibodies are proteins that are used by the immune system to identify and neutralize foreign objects, such as bacteria and viruses. Classifying antibodies, based on the similarity of their binding to the antigens, is essential for progress in immunology and clinical medicine. A striking feature of the natural immune system is its use of negative detection in which “self” is represented (approximately) by the set of circulating lymphocytes that fail to match self. This suggests the idea of a negative representation, in which a set of data elements is represented by its complement set. That is, all the elements not in the original set are represented (a potentially huge number), and the data itself are not explicitly stored. This representation has interesting information-hiding properties when privacy is a concern and it has implications for intrusion detection. One of the example where this idea has been concretized is exactly the case of a negative database [59].

In a negative database, the negative image of a set of data records is represented rather than the records themselves. Negative databases have the potential to help prevent inappropriate queries and inferences. Under this scenario, it is desirable that the database supports only the allowable queries while protecting the privacy of individual records, say from inspection by an insider. A second goal involves distributed data, where one would like to determine privately the intersection of sets owned by different parties. For example, two or more entities might wish to determine which of a set of possible “items” (transactions) they have in common without revealing the totality of the contents of their database or its cardinality.

Since in our model a datum is essentially stored as the set of matching items plus the set of non-matching ones, our results can be applied both to positive and negative representation of data.



## Chapter 3

### Role of fluctuations in the experienced pain perception

In the first chapter we have reviewed the main features of pain, focussing on the cascade of successive reactions which are activated by the so called noxious stimuli: The peripheral terminals of primary sensory neurons launch the signal, which is then transmitted to the spinal and supraspinal nuclei and eventually yields to the activation of a matrix of cortical areas that are deputed to the conscious experience of pain.

More specifically, the stimulus originating from a bodily harming menace can be directly processed through transduction by the receptors located on the nerve terminals. Alternatively, an indirect pathway can take over through the activation of transient receptor potentials on keratinocytes or the release of intermediate molecules which, in turn, act on sensory neurons receptors. In the following we shall assume the first scenario to hold, and, though certainly important, disregard other mechanisms that might be simultaneously in play. In other words, we simplistically imagine that pain receptors act as effective gates, channeling the route to the involved cortical circuits.

Analgesic drugs relieve the pain by interfering with the peripheral and central nervous system. Drug molecules bind in fact their target receptors, and consequently inhibit the pain perception. To grasp and visualize the essence of the process, one can hypothesize that the bound chemical element occludes the path, by impeding the signal transduction through the channel envisioned above.

Analgesic are commonly used in basic research and clinical practice, but their interaction with nociceptory and normal sensory processing remains to be fully unraveled. In section 1.5 of the first chapter we mentioned that analgesics are for instance known to modify the electrical recordings measured via evoked potentials (ERPs) responses [60], a powerful diagnostic tools employed to monitor and characterize a large variety of central nervous system disorders. ERPs are elicited by a specific stimulus applied to the e.g. pain receptors and consist in recording the induced electrical brain activity, as detected by localized electrodes placed on the surface of the head. Furthermore, ERPs are also useful in documenting objective response to pain [61, 62] and can thus prove fundamental to elucidate the molecular processes that control analgesic absorption and metabolism.

As shown by Fig. 2 of [28] discussed in section 1.5, different analgesic agents have been shown to produce intriguingly distinct effects at the level of the ERPs. Recorded time series of the solicited electric activity display in fact remarkably different patterns, which are generically attributed to the chemical specificity of the analgesic compound. Qualitatively, large, regular, oscillations of the electric response manifest, latency and amplitude being peculiar traits, supposedly related to the molecular characteristic of

the administered drug.

Furthermore, cycles in the perception of pain have been also reported which might be hypothetically driven by similar microscopic processes, the interaction between the anaesthetic molecules and their targets playing certainly a role of paramount importance. Clearly, the individual experience of pain is also influenced by psychological and cultural factors, unfortunately difficult to deconvolve when aiming at resolving the objective picture.

The issue of developing a unique interpretative framework to account for the presence of such oscillatory regimes has catalyzed vigorous discussions. The puzzle of their existence remains however to be fully understood.

Current mathematical models approach the problem via deterministic paradigms, thus neglecting the crucial role which is certainly played by the noise, intrinsic to the phenomenon under scrutiny [63]. These aspects become particularly important when accounting for the presence of diverse chemical species, which populate the stream flow in a spatially diffusive environment. Different chemical entities may compete with the drug molecules and occupy the sites located in close vicinity of the receptors, thus effectively hindering the binding event. Under specific conditions, such competition sustained by the stochastic component of the dynamics might result in large temporal oscillations for the amount of bound receptors, a mechanism which could explain the emergence of macroscopic cycles for the sensation of pain in response to medicaments.

In this chapter, we shall speculate on the above scenario by putting forward a network of chemical reactions and performing a system-size expansion through the celebrated van Kampen theory [64]. This enables us to derive a set of linear equations for the fluctuations, with coefficients related to the steady-state concentrations predicted from the first-order theory (i.e. the deterministic rate equations). Solutions are identified for which the deterministic steady-state occurs via damped oscillations: the inclusion of second-order fluctuations leads then to the amplification of sustained oscillations. These conclusions are briefly discussed with reference to the existing medical literature.

### 3.1 The chemical equations governing the microscopic process

Within the simplified scenario depicted above, we shall model the chemical interaction between a large, though finite, number of drug molecules (analgesics), hereby termed  $T$ , and free receptors  $R_F$  which represent their binding target. Following a successful binding event, a molecule of the species  $T$  disappears, leaving an empty case, hereafter labeled  $E$ . The population of bound receptor  $R_T$  is in turn increased by one unit. These assumptions formally translate into the compact chemical notation:



where  $\alpha$  stands for the associated reaction rate. The inverse reaction corresponding to the spontaneous detachment of the bound component may occur<sup>1</sup> with a certain

<sup>1</sup> We here assume that the free  $T$  molecule is still chemically active and can thus potentially chase for unscreened targets. This working hypothesis can be relaxed leading to conclusions qualitatively similar to the ones highlighted below.

probability  $\beta^2$ , which motivates the introduction of the dual relation:

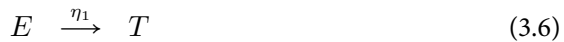


The analgesic molecules  $T$  surf in a densely packed environment and certainly experience collisions with several other microscopic chemical entities,  $H$ , which populate the streaming flow. Binary interactions between  $H$  and  $T$  elements, can occur in the close vicinity of the receptors ( $R_F$ ) location, potentially disturbing and eventually interfering with the binding event. As a result of an hypothetical collision, the active species  $T$  can be ejected by the spatial layer immediately adjacent to the receptor, leaving behind an empty case  $E$ . Beyond this effect, which stems from purely steric interactions, one has to account for possible chemical transformations, which might occur when individuals from the  $H$  and  $T$  species encounter: The active chaser  $T$  can lose its ability to bind the target<sup>3</sup> and it is thus mapped into an inactive  $H$  molecule. To incorporate these effects into the proposed description we postulate the following interaction rules, which are loosely inspired to the predator–prey competition mechanism:



The values of  $\sigma$  and  $\gamma$  characterize the effectiveness of the interaction, which is in turn sensitive to the choice of the compound  $T$ . The idealized cartoons of Fig. 3.1 are aimed at visualizing the above reaction schemes.

To complete the model we introduce an effective migration, by requiring that the  $T$  and  $H$  molecules can enter (resp. leave) the region deputed to the interaction. The latter assumption yields to the following set of chemical relations:



The population, namely the ensemble of elements belonging to an homologous species  $X$ , will be labeled in the following with the symbol  $n_X$ . Notice that the number of receptors  $N_1 = n_{R_T} + n_{R_F}$  and the total amount of molecules (including the empties)  $N_2 = n_T + n_H + n_E$  are conserved quantities. This observation enables us to reduce the complexity of the problem by setting:

$$n_{R_F} = N_1 - n_{R_T} \quad n_E = N_2 - n_T - n_H$$

<sup>2</sup> In principle it would be extremely useful to dispose of experimental estimates for the reaction rates, so to define a realistic range of variability for the free parameters in the model. The most reliable data concern the so-called (equilibrium) affinity constant for the case of e.g. the Tramadol. Depending on the target receptor (and on the specificity of the chaser's molecule) the affinity constant is reported to vary of a large amount which scans two orders of magnitude (from fraction of unity to hundreds) [25, 49].

<sup>3</sup> Note that this can happen both due to a mechanical stress or via chemical combination of the colliding species, see for instance [30] where the plasma protein binding is discussed. For a specific application relative to the case of tramadol refer to [65].

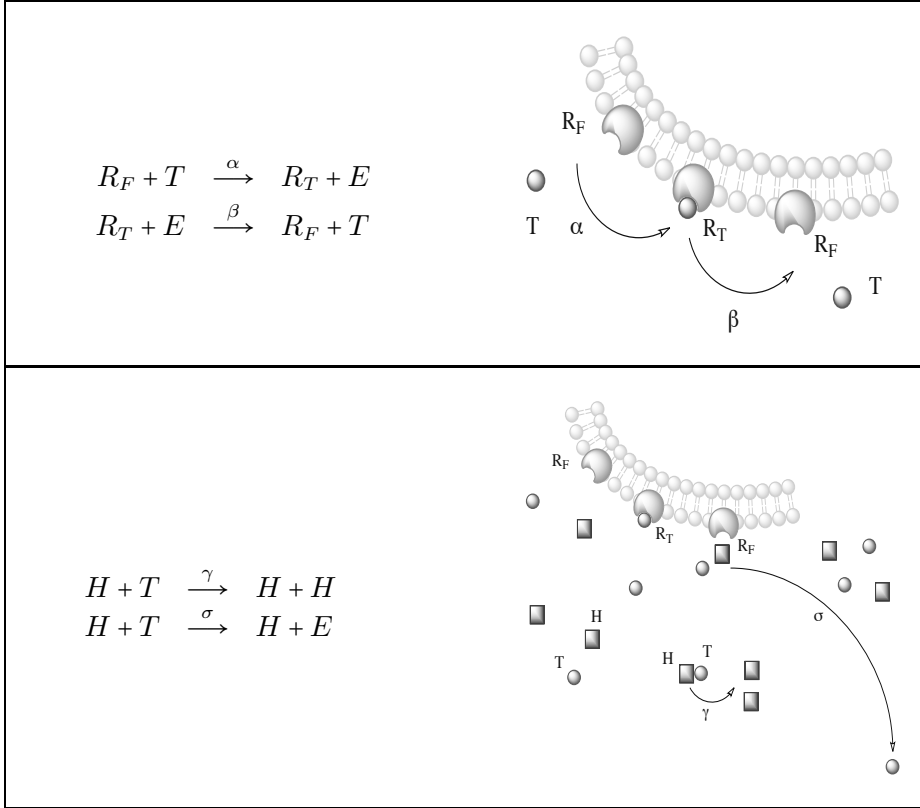


Figure 3.1: The main reaction schemes are depicted. The squares stand for the inactive species, while the circles represent the drug molecules. The model is then complemented with a set of additional reactions (see equations (3.5)–(3.8)), which accounts for the possibility that  $T$  and  $H$  enter (resp. leave) the region deputed for the interaction.

In the following we shall use the vectorial notation  $\underline{n} = (n_T, n_{R_T}, n_H)$  to help keeping the mathematical developments compact.

If we denote by  $n_X$  the number of elements belonging to an homologous species  $X$ , it is reasonable to assume that number of receptors  $N_1 = n_{R_T} + n_{R_F}$  and the total amount of molecules (including the empties)  $N_2 = n_T + n_H + n_E$  are conserved quantities. The inherent complexity of the problem is hence reduced by setting:

$$n_{R_F} = N_1 - n_{R_T} \quad n_E = N_2 - n_T - n_H$$

so that the system is completely specified by the vector  $\underline{n} = (n_T, n_{R_T}, n_H)$ .

We assume that the two populations are homogeneous, where all individuals have the same chance of interacting. In this case, the probability of an events happening only depends on the probabilities of choosing the various elements from the total corresponding population and the rates at which they take place. So we can define transition rates  $T(\underline{n}'|\underline{n})$  from state  $\underline{n}$  to a new state  $\underline{n}'$ , where  $\underline{n}'$  is one of the admissible state defined by the chemical equations (3.1)–(3.8). In our case,  $\underline{n}'$  can only be

$(n_T \pm 1, n_{R_T} \mp 1, n_H)$ ,  $(n_T - 1, n_{R_T}, n_H + 1)$ ,  $(n_T \pm 1, n_{R_T}, n_H)$  or  $(n_T, n_{R_T}, n_H \pm 1)$ , and so just seven transition probabilities differ from zero, namely:

$$\begin{aligned}
 T(n_T - 1, n_{R_T} + 1, n_H | \underline{n}) &= \alpha \frac{n_T}{N_2} \frac{N_1 - n_{R_T}}{N_1} \\
 T(n_T + 1, n_{R_T} - 1, n_H | \underline{n}) &= \beta \frac{N_2 - n_T - n_H}{N_2} \frac{n_{R_T}}{N_1} \\
 T(n_T - 1, n_{R_T}, n_H + 1 | \underline{n}) &= \gamma \frac{n_H}{N_2} \frac{n_T}{N_2} \\
 T(n_T - 1, n_{R_T}, n_H | \underline{n}) &= \sigma \frac{n_H}{N_2} \frac{n_T}{N_2} + \delta_1 \frac{n_T}{N_2} \\
 T(n_T + 1, n_{R_T}, n_H | \underline{n}) &= \eta_1 \frac{N_2 - n_T - n_H}{N_2} \\
 T(n_T, n_{R_T}, n_H - 1 | \underline{n}) &= \delta_2 \frac{n_H}{N_2} \\
 T(n_T, n_{R_T}, n_H + 1 | \underline{n}) &= \eta_2 \frac{N_2 - n_T - n_H}{N_2}
 \end{aligned}$$

With the above transition probabilities the master equation for the probability  $P(\underline{n}, t)$  to observe the system in the state  $\underline{n}$  at time  $t$ , may be written as

$$\begin{aligned}
 \frac{d}{dt} P(\underline{n}, t) &= T(\underline{n} | n_T + 1, n_{R_T} - 1, n_H) P(n_T + 1, n_{R_T} - 1, n_H, t) \\
 &+ T(\underline{n} | n_T - 1, n_{R_T} + 1, n_H) P(n_T - 1, n_{R_T} + 1, n_H, t) \\
 &+ T(\underline{n} | n_T + 1, n_{R_T}, n_H - 1) P(n_T + 1, n_{R_T}, n_H - 1, t) \\
 &+ T(\underline{n} | n_T + 1, n_{R_T}, n_H) P(n_T + 1, n_{R_T}, n_H, t) \\
 &+ T(\underline{n} | n_T - 1, n_{R_T}, n_H) P(n_T - 1, n_{R_T}, n_H, t) \\
 &+ T(\underline{n} | n_T, n_{R_T}, n_H + 1) P(n_T, n_{R_T}, n_H + 1, t) \\
 &+ T(\underline{n} | n_T, n_{R_T}, n_H - 1) P(n_T, n_{R_T}, n_H - 1, t) \\
 &- \left[ T(n_T - 1, n_{R_T} + 1, n_H | \underline{n}) + T(n_T + 1, n_{R_T} - 1, n_H | \underline{n}) \right. \\
 &+ T(n_T - 1, n_{R_T}, n_H + 1 | \underline{n}) + T(n_T - 1, n_{R_T}, n_H | \underline{n}) \\
 &+ T(n_T + 1, n_{R_T}, n_H | \underline{n}) + T(n_T, n_{R_T}, n_H - 1 | \underline{n}) \\
 &\left. + T(n_T, n_{R_T}, n_H + 1 | \underline{n}) \right] P(\underline{n}, t) \tag{3.9}
 \end{aligned}$$

Multiplying both sides of equation (3.9) by  $n_X$ , summing over all states, and remem-

bering that by definition  $\langle n_x \rangle = \sum_{\underline{n}} n_X P(\underline{n}, t)$ , we obtain

$$\begin{aligned} \frac{d}{dt} \langle n_T \rangle &= -\alpha \left\langle \frac{n_T}{N_2} \frac{N_1 - n_{RT}}{N_1} \right\rangle - (\gamma + \sigma) \left\langle \frac{n_H}{N_2} \frac{n_T}{N_2} \right\rangle - \delta_1 \left\langle \frac{n_T}{N_2} \right\rangle \\ &\quad + \beta \left\langle \frac{N_2 - n_T - n_H}{N_2} \frac{n_{RT}}{N_1} \right\rangle + \eta_1 \left\langle \frac{N_2 - n_T - n_H}{N_2} \right\rangle \\ \frac{d}{dt} \langle n_{RT} \rangle &= \alpha \left\langle \frac{n_T}{N_2} \frac{N_1 - n_{RT}}{N_1} \right\rangle - \beta \left\langle \frac{N_2 - n_T - n_H}{N_2} \frac{n_{RT}}{N_1} \right\rangle \\ \frac{d}{dt} \langle n_H \rangle &= \gamma \left\langle \frac{n_H}{N_2} \frac{n_T}{N_2} \right\rangle + \eta_2 \left\langle \frac{N_2 - n_T - n_H}{N_2} \right\rangle - \delta_2 \left\langle \frac{n_H}{N_2} \right\rangle \end{aligned}$$

In the limit  $N_1, N_2 \rightarrow \infty$ , we can replace  $\langle n_X n_Y \rangle$  with  $\langle n_X \rangle \langle n_Y \rangle$ , and  $\langle n_T \rangle / N_2$ ,  $\langle n_{RT} \rangle / N_1$ ,  $\langle n_H \rangle / N_2$  become the deterministic variables  $\phi_T$ ,  $\phi_{RT}$  and  $\phi_H$  of the mean-field system

$$\begin{aligned} \frac{d}{d\tau} \phi_T &= -\hat{\alpha} \phi_T (1 - \phi_{RT}) + \hat{\beta} \phi_{RT} (1 - \phi_T - \phi_H) \\ &\quad - (1 + \hat{\sigma}) \phi_H \phi_T - \hat{\delta}_1 \phi_T + \hat{\eta}_1 (1 - \phi_T - \phi_H) \end{aligned} \quad (3.10)$$

$$\frac{d}{d\tau} \phi_{RT} = c \left[ \hat{\alpha} \phi_T (1 - \phi_{RT}) - \hat{\beta} \phi_{RT} (1 - \phi_T - \phi_H) \right] \quad (3.11)$$

$$\frac{d}{d\tau} \phi_H = \phi_H \phi_T + \hat{\eta}_2 (1 - \phi_T - \phi_H) - \hat{\delta}_2 \phi_H \quad (3.12)$$

where  $c = N_2 / N_1$ . In the previous equations we have absorbed the parameter  $\gamma$  in the definition of the rescaled time  $\tau = t\gamma / N_2$  and introducing additionally  $\hat{\alpha} = \alpha / \gamma$ ,  $\hat{\beta} = \beta / \gamma$ ,  $\hat{\sigma} = \sigma / \gamma$ ,  $\hat{\delta}_1 = \delta_1 / \gamma$ ,  $\hat{\eta}_1 = \eta_1 / \gamma$ ,  $\hat{\delta}_2 = \delta_2 / \gamma$ ,  $\hat{\eta}_2 = \eta_2 / \gamma$ .

Having specified the mathematical context that defines the problem at hand, we can proceed following two different, though complementary, approaches. On the one hand one can simulate the full stochastic process, via the celebrated Gillespie algorithm. On the other, analytical tools can be invoked to grasp the essential traits of the underlying dynamics.

Stochastic effects fade off for an infinite population amount and the system of equations (3.1)–(3.8) tends to its deterministic mean-field solution, as remarked above. For a moderate number of individuals, the intrinsic noise due to the discrete nature of the individuals can instead play an important role. In some cases, indeed, the stochastic process may result in large persistent fluctuations which, with reference to this specific case, can drive significant repercussion on e.g. the effect of a chosen pharmacological therapy. As we stated in the introductory section, cycles do emerge at the level of the electric brain activity, as registered via the ERPs for patients under pharmacological treatment. The claim substantiated in [66] is that such oscillatory behaviors might appear due to finite size corrections to the mean-field dynamics, being hence intimately related to the intrinsic molecular granularity. Different qualitative patterns might be associated to peculiar chemical properties of the drugs, an information which is here incorporated into the assigned rates.

The onset of these oscillations depends on the nature of the equilibrium points of the mean-field equations. Finite size induced fluctuations may give rise to persistent cycles

when the equilibrium point is a stable focus: Intrinsic noise perturbs the systems, and prevents it from approaching its natural asymptotic solution, via damped oscillations. Under this condition, a resonance may develop which yields to oscillations at a given, dynamically selected, frequency<sup>4</sup>. Aiming at identifying the necessary condition for these oscillatory regimes to develop about the mean-field equations (3.10)–(3.12), one needs to single out the parameters' values which correspond to complex eigenvalues of the Jacobian matrix associated to the mean-field systems. In our case the elements of the Jacobian matrix reads

$$\begin{aligned}
 J_{11}(\underline{\phi}^*) &= -\hat{\alpha}(1 - \phi_{RT}^*) - \hat{\beta}\phi_{RT}^* - (1 + \hat{\sigma})\phi_H^* - \hat{\delta}_1 - \hat{\eta}_1 \\
 J_{12}(\underline{\phi}^*) &= \hat{\alpha}\phi_T^* + \hat{\beta}(1 - \phi_T^* - \phi_H^*) \\
 J_{13}(\underline{\phi}^*) &= -\hat{\beta}\phi_{RT}^* - (1 + \hat{\sigma})\phi_T^* - \hat{\eta}_1 \\
 J_{21}(\underline{\phi}^*) &= c[\hat{\alpha}(1 - \phi_{RT}^*) + \hat{\beta}\phi_{RT}^*] \\
 J_{22}(\underline{\phi}^*) &= -c[\hat{\alpha}\phi_T^* + \hat{\beta}(1 - \phi_T^* - \phi_H^*)] \\
 J_{23}(\underline{\phi}^*) &= c\hat{\beta}\phi_{RT}^* \\
 J_{31}(\underline{\phi}^*) &= \phi_H^* - \hat{\eta}_2 \\
 J_{32}(\underline{\phi}^*) &= 0 \\
 J_{33}(\underline{\phi}^*) &= \phi_T^* - \hat{\eta}_2 - \hat{\delta}_2
 \end{aligned} \tag{3.13}$$

where  $\underline{\phi}^* = (\phi_T^*, \phi_{RT}^*, \phi_H^*)$  denotes the equilibrium point of system (3.10)–(3.12). To analytically addressing the full problem proves rather cumbersome. For this reason, in the next section, we start by discussing a simpler case study, and eventually move towards the general settings.

### 3.2 On the case with $\hat{\eta}_2 = 0$ : Neglecting the inward migration of inactive molecules

Molecules of species  $H$  can appear the region of the interaction, as resulting from two independent mechanisms: Diffusion may occur as prescribed by equation (3.8) as well as chemical inactivation (3.4). Imagine this latter to dominate over the former, an assumption which we here exemplifies by setting to zero the migration contribution, i.e.  $\eta_2 = 0$ . This working ansatz enables us to write down closed analytical expressions for the two equilibrium points  $\underline{\phi}_1^*$  and  $\underline{\phi}_2^*$ . A straightforward algebraic manipulation leads to:

$$\begin{aligned}
 \underline{\phi}_1^* &= \left( \frac{\hat{\eta}_1}{\hat{\delta}_1 + \hat{\eta}_1}, \frac{\hat{\alpha}\hat{\eta}_1}{\hat{\beta}\hat{\delta}_1 + \hat{\alpha}\hat{\eta}_1}, 0 \right) \\
 \underline{\phi}_2^* &= \left( \hat{\delta}_2, \frac{\hat{\alpha}[\hat{\delta}_2(1 + \hat{\sigma}) + \hat{\eta}_1]}{\hat{\alpha}[\hat{\delta}_2(1 + \hat{\sigma}) + \hat{\eta}_1] + \hat{\beta}[(1 + \hat{\sigma})(1 - \hat{\delta}_2) + \hat{\delta}_1]}, \frac{\hat{\eta}_1(1 - \hat{\delta}_2) - \hat{\delta}_1\hat{\delta}_2}{\hat{\delta}_2(1 + \hat{\sigma}) + \hat{\eta}_1} \right)
 \end{aligned}$$

<sup>4</sup> The importance of this, rather general, property is being addressed in [6, 7] and will be touched upon in the forthcoming discussion.

As previously mentioned, a stability analysis represents the first mandatory step to identifying the parameters range which yields to the oscillations. As concerns  $\underline{\phi}_1^*$ , one can easily calculate the three eigenvalues  $\lambda_i$  ( $i = 1, 2, 3$ ) of  $J(\underline{\phi}_1^*)$  which respectively reads:

$$\begin{aligned}\lambda_1 &= \frac{\hat{\eta}_1}{\hat{\eta}_1 + \hat{\delta}_1} - \hat{\delta}_2 \\ \lambda_{2,3} &= \frac{-\left[\hat{\eta}_1 + \hat{\delta}_1 + \frac{\hat{\alpha}\hat{\beta}(\hat{\eta}_1 + \hat{\delta}_1)}{\hat{\alpha}\hat{\eta}_1 + \hat{\beta}\hat{\delta}_1} + c\frac{\hat{\alpha}\hat{\eta}_1 + \hat{\beta}\hat{\delta}_1}{\hat{\eta}_1 + \hat{\delta}_1}\right] \pm \sqrt{D_1}}{2}\end{aligned}$$

where

$$D_1 = (\hat{\eta}_1 + \hat{\delta}_1)^2 \left[ 1 + \frac{\hat{\alpha}^2\hat{\beta}^2(c^2 + 1)}{(\hat{\alpha}\hat{\eta}_1 + \hat{\beta}\hat{\delta}_1)^2} + \frac{2\hat{\alpha}\hat{\beta}(1 - c)}{\hat{\alpha}\hat{\eta}_1 + \hat{\beta}\hat{\delta}_1} \right] + 2c\hat{\alpha}\hat{\beta}$$

Eigenvalues  $\lambda_2$  and  $\lambda_3$  are always real and negative, so that  $\underline{\phi}_1^*$  is globally stable if  $\lambda_1 < 0$ , a condition which immediately translates into:

$$\hat{\delta}_2 > \frac{\hat{\eta}_1}{\hat{\eta}_1 + \hat{\delta}_1} \quad (3.14)$$

The stability of the second equilibrium point  $\underline{\phi}_2^*$  cannot be handled analytically and it is hence carried out numerically. To this end we notice that the characteristic polynomial associated to the Jacobian matrix (3.13) is a cubic equation of the type:

$$a\lambda^3 + b\lambda^2 + c\lambda + d = 0 \quad (3.15)$$

$a, b, c$  being implicit function of the relevant chemical parameters. One can hence introduce the so called discriminant  $\Delta$  defined as  $\Delta = -4b^3d + b^2c^2 - 4ac^3 + 18abcd - 27a^2d^2$ . It is well known that the cubic equation admits a pair of complex conjugate roots if  $\Delta < 0$ . One can then scan over the available parameters space, looking those combination which implies a negative discriminant, namely the potential signature of an oscillatory stochastic dynamics. In the next subsections we shall report on our numerical and analytical findings.

### 3.2.1 Considering the case $\hat{\delta}_1 = \hat{\eta}_1$

In the proposed model, chemical reactions (3.5) and (3.6) stem for the local diffusion from the inspected target region. As a first working hypothesis, one can equate incoming and outgoing contributions and hence assume the simplifying setting where  $\hat{\delta}_1 = \hat{\eta}_1$ . In practice this amount to sampling the interesting parameter region along a preferential direction.

Under this assumption, we set down to study the sign of the discriminant  $\Delta$  associated to  $\underline{\phi}_2^*$ , when scanning the plane  $(\hat{\delta}_1, \hat{\delta}_2)$  for fixed  $N_1, N_2, \hat{\alpha}, \hat{\beta}$  and  $\hat{\sigma}$  (values as in the caption of Fig. 3.2). The colored region shown in Fig. 3.2 corresponds to pair  $(\hat{\delta}_1, \hat{\delta}_2)$  which yields to complex eigenvalues of the Jacobian  $J(\underline{\phi}_2^*)$ . The colorcode refers to the (absolute) values of the corresponding complex eigenvalues. A visual inspection allows

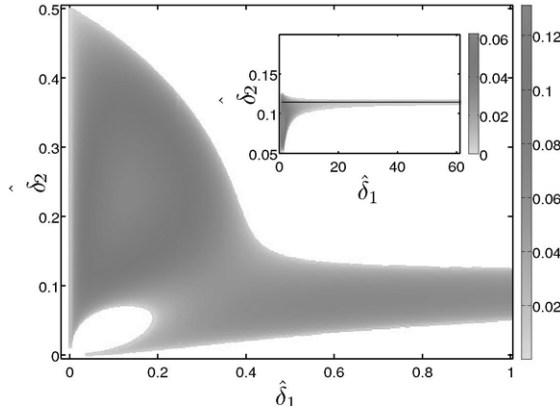


Figure 3.2: We report a projection of the admissible parameter space: Here  $\hat{\delta}_1$  and  $\hat{\delta}_2$  are allowed to vary.  $\hat{\eta}_1$  also changes under the constraint  $\hat{\eta}_1 = \hat{\delta}_1$ . The other parameters are kept fixed:  $\hat{\alpha} = 0.9$ ,  $\hat{\beta} = 0.6$ ,  $\hat{\sigma} = 0.5$ ,  $\hat{\eta}_1 = \hat{\delta}_1$  and  $\hat{\eta}_2 = 0$ . The number of simulated molecules is  $N_1 = 4000$ ,  $N_2 = 9000$ . Points falling in the colored region, are characterized by complex eigenvalues associated to the stable equilibrium point  $\phi_2^*$ . This implies an oscillatory (damped) convergence to fixed point. Colorcoding measures the magnitude of the absolute value of the eigenvalues' imaginary part. The insert shows an enlargement of the main panel to fully appreciate the region for  $\hat{\delta}_1 > 1$ . A critical  $\hat{\delta}_2^{crit}$  exists where complex eigenvalues are found for any  $\delta_1$  amount. The black line represents the theoretical prediction (3.17) which accurately locates the singularity in the parameter space.

us to highlight two interesting features. First, we notice that for  $\hat{\delta}_2 > 0.5$ , no values of  $\hat{\delta}_1$  are found that satisfy the sought condition  $\Delta < 0$ . This conclusion, reached on the basis of a purely numerical evidence, is also confirmed by a simple analytical argument which is developed in the following. Consider the condition  $\hat{\delta}_1 \ll 1$ , and so focus on the leftmost region of the plane in Fig. 3. 2. Performing a power series expansion of  $\Delta$  in  $\hat{\delta}_1$ , and retaining only first order terms, one immediately obtains:

$$\Delta = \frac{\left[ c\hat{\beta}^2(\hat{\delta}_2 - 1)^2 + c\hat{\alpha}^2\hat{\delta}_2^2 + \hat{\alpha}\hat{\beta}(1 - 2c(\hat{\delta}_2 - 1)\hat{\delta}_2) \right]^3}{\left[ \hat{\beta}(\hat{\delta}_2 - 1) - \hat{\alpha}\hat{\delta}_2 \right]^2} \cdot 4c\hat{\delta}_1(2\hat{\delta}_2 - 1) + \mathcal{O}(\hat{\delta}_1^2)$$

An exact calculation allows one to prove that  $\Delta$  is negative for  $\hat{\delta}_2 < 0.5$ . Notice that this conclusion holds for any chosen parameters' setting and has to be regarded as a general property of the model at hand<sup>5</sup>. It is worth emphasizing that condition  $\hat{\delta}_2 > 0.5$  also arises when looking for positive real eigenvalues associated to  $\phi_1^*$ : In other words  $\hat{\delta}_2 = 0.5$  sets the frontier for the global stability of  $\phi_1^*$ , as it follows by inserting  $\hat{\eta}_1 = \hat{\delta}_1$  in equation (3.14).

<sup>5</sup> Numerical simulations show that this result holds also when  $\hat{\eta}_1 \neq \hat{\delta}_1$ . More specifically, there are no complex eigenvalues for  $\hat{\delta}_2 > \hat{\eta}_1/(\hat{\eta}_1 + \hat{\delta}_1)$ .

The second aspect which is brought to our attention when analyzing the scenario depicted in Fig.3. 2 has to do with the pronounced peak which emerges at a specific, critical value of  $\hat{\delta}_2$ . Let us label such a value with  $\hat{\delta}_2^{crit}$  and notice that it corresponds to requiring  $\Delta < 0 \forall \hat{\delta}_1$ . This latter observation results in a straightforward strategy for analytically evaluating  $\hat{\delta}_2^{crit}$ . We start by rearranging the expression of  $\Delta$  as a fractional polynomial of  $\hat{\delta}_1$ . In formulae we get:

$$\Delta = \frac{\Delta_{num}}{\Delta_{den}} = \frac{\sum_{i=0}^{14} a_i \hat{\delta}_1^i}{\sum_{k=0}^{10} b_k \hat{\delta}_1^k}$$

where the coefficients  $a_i$  and  $b_k$  are defined as functions of the chemical parameters of the model<sup>6</sup>.

Aiming at calculating  $\hat{\delta}_2^{crit}$ , one can consider  $\hat{\delta}_1$  large. Under this assumption,  $\Delta_{num} \simeq a_{14}\hat{\delta}_1^{14} + a_{13}\hat{\delta}_1^{13}$ , which can be cast in the explicit form:

$$\begin{aligned} \frac{\Delta_{num}}{\hat{\delta}_1^{13}} \simeq & -4(\hat{\alpha} + \hat{\beta})^3 \left[ -1 + 2(1 + c\hat{\alpha} + c\hat{\beta})\hat{\delta}_2 \right] \left[ 2c^2\hat{\beta}^3\hat{\delta}_2^2 \right. \\ & + 2c\hat{\beta}^2\hat{\delta}_2 \left( 4\hat{\delta}_2 - 7 - \hat{\delta}_1 + \hat{\alpha}(-2 + 3c\hat{\delta}_2) - 8\hat{\sigma} + 6\hat{\delta}_2\hat{\sigma} \right) \\ & + \hat{\alpha} \left( \hat{\delta}_1(1 - 2\hat{\delta}_2 - 2c\hat{\alpha}\hat{\delta}_2) + \hat{\sigma} + 2\hat{\delta}_2^2(-10 - 8c\hat{\alpha} + c^2\hat{\alpha}^2 \right. \\ & \left. - 8\hat{\sigma} - 6c\hat{\alpha}\hat{\sigma}) - 2\hat{\delta}_2(-5 + c\hat{\alpha} - 3\hat{\sigma} + 2c\hat{\alpha}\hat{\sigma}) \right) \\ & \left. + \hat{\beta} \left( 2c\hat{\alpha}^2\hat{\delta}_2(3c\hat{\delta}_2 - 2) - (2\hat{\delta}_2 - 1)(4 + \hat{\delta}_1 + 2\hat{\delta}_2 + 5\hat{\sigma}) \right. \right. \\ & \left. \left. - 4\hat{\alpha}(-1 + 2c\hat{\delta}_2^2 + \hat{\delta}_2(2 + 4c + c\hat{\delta}_1 + 5c\hat{\sigma})) \right) \right] \end{aligned}$$

As clearly displayed in Fig. 3.2, the boundaries of the two curves which enclose the domain for  $\Delta > 0$ , tend to merge asymptotically ( $\hat{\delta}_2^{crit} \rightarrow \infty$ ) and approach the horizontal line that goes through  $\hat{\delta}_2^{crit}$ . As the aforementioned boundaries are found by imposing the discriminant to zero, we argue that  $\hat{\delta}_2^{crit}$  can be estimated by setting  $\Delta = 0$  in the limit for large  $\hat{\delta}_1$  amount. This fact is also confirmed by looking at the inset of Fig. 3.2: As  $\hat{\delta}_1$  is increased the imaginary part of the eigenvalues progressively reduces (the color contrast fades), which again implies  $\Delta \rightarrow 0$ . In formulae, equating expression (3.16) to

<sup>6</sup> The explicit expressions of coefficients  $a_i$  and  $b_k$  has been worked out with Mathematica and involve hundreds of terms. It is hence not explicitly reported in the body of the paper but can be supplied upon request.

zero and solving for  $\hat{\delta}_1$  yields:

$$\begin{aligned} \hat{\delta}_1 = & \frac{1}{(\hat{\alpha} + \hat{\beta})(-1 + 2\hat{\delta}_2 + 2c\hat{\alpha}\hat{\delta}_2 + 2c\hat{\beta}\hat{\delta}_2)} \\ & \times \left( 4\hat{\beta} + 4\hat{\alpha}\hat{\beta} + 10\hat{\alpha}\hat{\delta}_2 - 2c\hat{\alpha}^2\hat{\delta}_2 - 6\hat{\beta}\hat{\delta}_2 - 8\hat{\alpha}\hat{\beta}\hat{\delta}_2 \right. \\ & - 16c\hat{\alpha}\hat{\beta}\hat{\delta}_2 - 4c\hat{\alpha}^2\hat{\beta}\hat{\delta}_2 - 14c\hat{\beta}^2\hat{\delta}_2 - 4c\hat{\alpha}\hat{\beta}^2\hat{\delta}_2 - 20\hat{\alpha}\hat{\delta}_2^2 \\ & - 16c\hat{\alpha}^2\hat{\delta}_2^2 + 2c^2\hat{\alpha}^3\hat{\delta}_2^2 - 4\hat{\beta}\hat{\delta}_2^2 - 8c\hat{\alpha}\hat{\beta}\hat{\delta}_2^2 + 6c^2\hat{\alpha}^2\hat{\beta}\hat{\delta}_2^2 \\ & + 8c\hat{\beta}^2\hat{\delta}_2^2 + 6c^2\hat{\alpha}\hat{\beta}^2\hat{\delta}_2^2 + 2c^2\hat{\beta}^3\hat{\delta}_2^2 + \hat{\alpha}\hat{\sigma} + 5\hat{\beta}\hat{\sigma} + 6\hat{\alpha}\hat{\delta}_2\hat{\sigma} \\ & - 4c\hat{\alpha}^2\hat{\delta}_2\hat{\sigma} - 10\hat{\beta}\hat{\delta}_2\hat{\sigma} - 20c\hat{\alpha}\hat{\beta}\hat{\delta}_2\hat{\sigma} - 16c\hat{\beta}^2\hat{\delta}_2\hat{\sigma} \\ & \left. - 16\hat{\alpha}\hat{\delta}_2^2\hat{\sigma} - 12c\hat{\alpha}^2\hat{\delta}_2^2\hat{\sigma} + 12c\hat{\beta}^2\hat{\delta}_2^2\hat{\sigma} \right) \end{aligned} \quad (3.16)$$

Large value of  $\hat{\delta}_1$ , i.e. the asymptotic condition we eventually wish to recover, are obtained by setting the above denominator to zero, which immediately implies:

$$\hat{\delta}_2^{crit} = \frac{1}{2 \left[ 1 + c(\hat{\alpha} + \hat{\beta}) \right]} \quad (3.17)$$

The above prediction is plotted in Fig. 3.2 and proves accurate in interpreting the numerics. As a final remark, we stress that, though calculated with reference to a specific selection of the involved parameters, the patterns displayed in Fig. 3. 2 are typical for the model under scrutiny. In particular, the dependence of equation (3.17) on both  $\hat{\alpha}$  and  $\hat{\beta}$  has been tested in a dedicated series of simulations which confirmed its excellent predictive adequacy.

### 3.2.2 Mean field vs. stochastic numerical computations

Numerical simulations of both the the mean–field equations and the original stochastic model are performed and compared to the scenario depicted above.

Figure 3. 3 shows a typical simulation for a set of parameters which is predicted to yield complex eigenvalues of  $J(\underline{\phi}_2^*)$ . Dashed lines in panels (a)–(c) represent the numerical solution of system (3.10)–(3.12): The mean–field equations exhibit damped oscillations when approaching the equilibrium point  $\underline{\phi}_2^*$ . Panel (d) reports a typical mean–field trajectory projected in the  $(\phi_T, \phi_{RT})$  plane:  $\underline{\phi}_2^*$  is indeed a stable focus, as one can appreciate visually.

Alternatively, one can perform a full stochastic simulation based on chemical equations (3.1)–(3.8). This is achieved through the Gillespie algorithm introduced in appendix A, which is equivalent to solving the underlying master equation (3.9). At variance with the mean–field system, which formally holds for  $N \rightarrow \infty$ , stochastic simulations (continuous lines in Fig. 3.3 ) display large and persistent oscillations about the stationary state. These oscillations emerge due to the discreteness of the simulated medium and are hence a typical finite size effect, which is deliberately forgotten in the realm of deterministic approaches.

The qualitative comparison between mean–field and full stochastic solutions points to the importance of properly accounting for the effect of granularity in any sensible

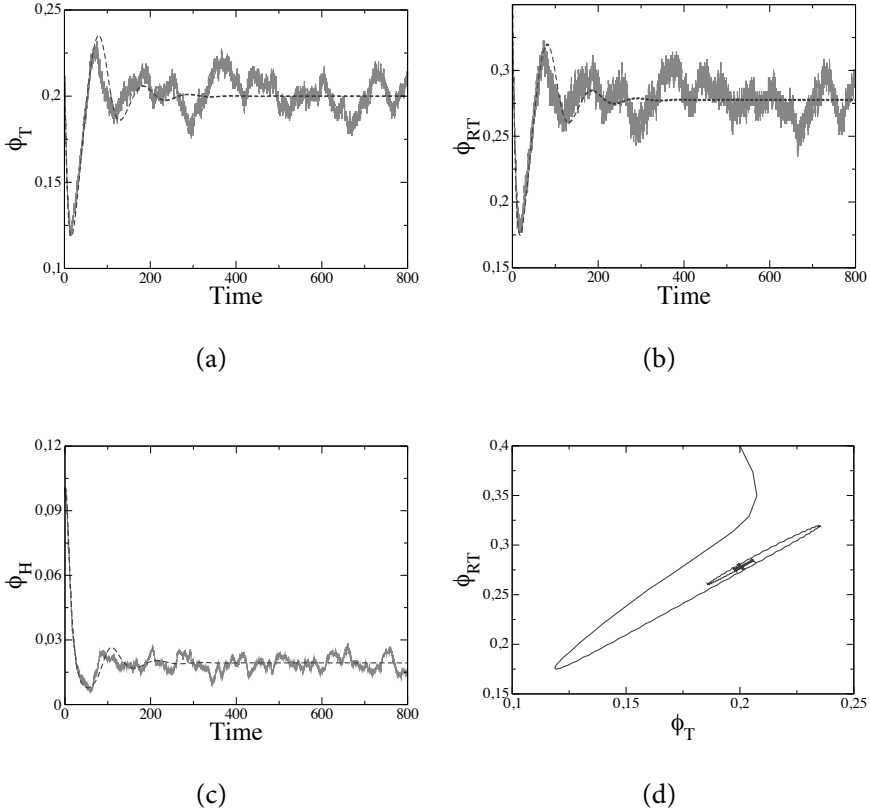


Figure 3.3: Panels (a)–(c) represent a typical solution of the mean–field system (dashed blue line) and the stochastic simulation (continuous magenta line). Panel (d) shows the projection of the above solution onto the plane  $(\phi_T, \phi_{RT})$ . Parameters used in the simulations are  $N_1 = 4000$ ,  $N_2 = 9000$ ,  $\hat{\alpha} = 0.9$ ,  $\hat{\beta} = 0.6$ ,  $\hat{\sigma} = 0.5$ ,  $\hat{\delta}_1 = \hat{\eta}_1 = 0.01$  and  $\hat{\delta}_2 = 0.2$ .

biomedical model. Traditional pharmacology, in fact, takes the mean–field viewpoint and cannot reproduce those collective behavior that might develop as an instability driven by the stochastic component to the dynamics. As imagined in our model, oscillations in the number of  $R_T$  molecules reflect in a modulation of the experienced perception of pain (and of the associated electrical indicators).

As already stated, the request for a complex eigenvalue of the linearized dynamics constitute a necessary condition for the existence of stochastic induced cycle. The contrary is not a priori guaranteed and dedicated computation tools are to be put in place so to access an estimate of the subset of parameters which might drive the resonant effect. This is for instance the case of the finite  $N$  perturbative expansion pioneered by Van Kampen. In the following section we revisit the main step of the derivation (already discussed in [66]), and exploit the conclusion to gain some insight into the role played by the parameters.

### 3.2.3 Parameters for the resonance condition: The large $N$ expansion

The conditions for the resonant instability reported in Fig. 3.3 are investigated via the perturbative expansion, termed after Van Kampen [64, 67], which applies to moderate value  $N$  of the population ensemble.

The method relies on the introduction of new set of stochastic (and continuous) variables, namely  $\underline{\xi} = (\xi_T, \xi_{R_T}, \xi_{R_H})$ , related to their discrete homologous via

$$\begin{aligned} n_T &= N_2 \phi_T(t) + \sqrt{N_2} \xi_T \\ n_{R_T} &= N_1 \phi_{R_T}(t) + \sqrt{N_1} \xi_{R_T} \\ n_H &= N_2 \phi_H(t) + \sqrt{N_2} \xi_H \end{aligned}$$

A new probability distribution  $\Pi(\underline{\xi}, \tau) = P(\underline{n}, t)$  can be hence defined which obeys to the master equation (3.9) now re-written in term of the new variables. In doing this we bring into the equation an explicit dependence on the amount of molecules (resp.  $N_1$  and  $N_2$ ). This fact enables us to perform a perturbative analysis inspired to the seminal work by Van Kampen [64], where  $N_1^{-1}$  (Eq.  $N_2^{-1}$ ) plays the role of a small parameter. At the lowest order of approximation, one recovers the deterministic mean-field equations (3.10), see [66].

The first technical point of the van Kampen expansion concerns the introduction of the so-called shift operators,  $\mathbb{E}_T^{\pm 1}, \mathbb{E}_{R_T}^{\pm 1}, \mathbb{E}_H^{\pm 1}$  which obey:

$$\begin{aligned} \mathbb{E}_T^{\pm 1} f(\underline{n}, t) &= f(n_T \pm 1, n_{R_T}, n_H) \\ \mathbb{E}_{R_T}^{\pm 1} f(\underline{n}, t) &= f(n_T, n_{R_T} \pm 1, n_H) \\ \mathbb{E}_H^{\pm 1} f(\underline{n}, t) &= f(n_T, n_{R_T}, n_H \pm 1). \end{aligned}$$

The master equation (3.9) is hence cast in the form:

$$\begin{aligned} &\frac{1}{N_2} \frac{\partial \Pi}{\partial \tau} - \frac{1}{\sqrt{N_2}} \frac{d}{d\tau} \phi_T \frac{\partial \Pi}{\partial \xi_T} - \frac{c^{-1}}{\sqrt{N_1}} \frac{d}{d\tau} \phi_{R_T} \frac{\partial \Pi}{\partial \xi_{R_T}} - \frac{1}{\sqrt{N_2}} \frac{d}{d\tau} \phi_H \frac{\partial \Pi}{\partial \xi_H} = \\ &+ (\mathbb{E}_T^{+1} \mathbb{E}_{R_T}^{-1} - 1) \left[ \alpha \left( 1 - \phi_{R_T} - \frac{\xi_{R_T}}{\sqrt{N_1}} \right) \left( \phi_T + \frac{\xi_T}{\sqrt{N_2}} \right) \Pi \right] \\ &+ (\mathbb{E}_T^{-1} \mathbb{E}_{R_T}^{+1} - 1) \left[ \beta \left( \phi_{R_T} + \frac{\xi_{R_T}}{\sqrt{N_1}} \right) \left( 1 - \phi_T - \frac{\xi_T}{\sqrt{N_2}} - \phi_H - \frac{\xi_H}{\sqrt{N_2}} \right) \Pi \right] \\ &+ (\mathbb{E}_T^{+1} \mathbb{E}_H^{-1} - 1) \left[ \gamma \left( \phi_T + \frac{\xi_T}{\sqrt{N_2}} \right) \left( \phi_H + \frac{\xi_H}{\sqrt{N_2}} \right) \Pi \right] \\ &+ (\mathbb{E}_T^{+1} - 1) \left[ \sigma \left( \phi_T + \frac{\xi_T}{\sqrt{N_2}} \right) \left( \phi_H + \frac{\xi_H}{\sqrt{N_2}} \right) \Pi + \delta_1 \left( \phi_T + \frac{\xi_T}{\sqrt{N_2}} \right) \Pi \right] \\ &+ (\mathbb{E}_T^{-1} - 1) \left[ \eta_1 \left( 1 - \phi_T - \frac{\xi_T}{\sqrt{N_2}} - \phi_H - \frac{\xi_H}{\sqrt{N_2}} \right) \Pi \right] \\ &+ (\mathbb{E}_H^{+1} - 1) \left[ \delta_2 \left( \phi_H + \frac{\xi_H}{\sqrt{N_2}} \right) \Pi \right] \end{aligned} \quad (3.18)$$

The advantage of using the shift operators relies in that they admit a simple expansion in the limit for  $N_1$  (resp.  $N_2$ ) large:

$$\mathbb{E}_T^{\pm 1} = 1 \pm N_2^{-1/2} \frac{\partial}{\partial \xi_T} + \frac{1}{2} N_2^{-1} \frac{\partial^2}{\partial \xi_T^2} \pm \dots \quad (3.19)$$

$$\mathbb{E}_{R_T}^{\pm 1} = 1 \pm N_1^{-1/2} \frac{\partial}{\partial \xi_{R_T}} + \frac{1}{2} N_1^{-1} \frac{\partial^2}{\partial \xi_{R_T}^2} \pm \dots \quad (3.20)$$

$$\mathbb{E}_H^{\pm 1} = 1 \pm N_2^{-1/2} \frac{\partial}{\partial \xi_H} + \frac{1}{2} N_2^{-1} \frac{\partial^2}{\partial \xi_H^2} \pm \dots \quad (3.21)$$

Plugging (3.19)–(3.21) into (3.18), after some algebraic manipulation, one recovers at the leading order the mean–field equations, formally identical to the ones reported above, see equations (3.10)–(3.12). The next-to–leading order result in a Fokker Planck equation for the probability distribution  $\Pi(\underline{\xi}, t)$ :

$$\frac{\partial \Pi}{\partial \tau} = - \sum_i \frac{\partial}{\partial \xi_i} (A_i(\underline{\xi}) \Pi) + \frac{1}{2} \sum_{ij} B_{ij} \frac{\partial^2 \Pi}{\partial \xi_i \partial \xi_j} \quad (3.22)$$

where  $A_i(\underline{\xi}) = \sum_j M_{ij} \xi_j$  (hence linear in  $\xi_i$ ). The elements of the matrix  $M$  are

$$\begin{aligned} M_{11} &= -\hat{\alpha}(1 - \phi_{R_T}^*) - \beta \phi_{R_T}^* - (1 + \hat{\sigma}) \phi_H^* - \hat{\delta}_1 - \hat{\eta}_1 \\ M_{12} &= c^{1/2} [\hat{\alpha} \phi_T^* + \hat{\beta}(1 - \phi_T^* - \phi_H^*)] \\ M_{13} &= -\hat{\beta} \phi_{R_T}^* - (1 + \hat{\sigma}) \phi_T^* - \hat{\eta}_1 \\ M_{21} &= c^{1/2} [\hat{\alpha}(1 - \phi_{R_T}^*) + \hat{\beta} \phi_{R_T}^*] \\ M_{22} &= -c [\hat{\alpha} \phi_T^* + \hat{\beta}(1 - \phi_T^* - \phi_H^*)] \\ M_{23} &= c^{1/2} \hat{\beta} \phi_{R_T}^* \\ M_{31} &= \phi_H^* \\ M_{32} &= 0 \\ M_{33} &= \phi_T^* - \hat{\delta}_2 \end{aligned} \quad (3.23)$$

while the noise correlation matrix  $B$  is symmetric and it is given by

$$\begin{aligned} B_{11} &= \hat{\alpha} \phi_T^* (1 - \phi_{R_T}^*) + \hat{\beta} \phi_{R_T}^* (1 - \phi_T^* - \phi_H^*) \\ &\quad + (1 + \hat{\sigma}) \phi_T^* \phi_H^* + \hat{\delta}_1 \phi_T^* + \hat{\eta}_1 (1 - \phi_T^* - \phi_H^*) \\ B_{12} &= -c^{1/2} [\hat{\alpha} \phi_T^* (1 - \phi_{R_T}^*) + \hat{\beta} \phi_{R_T}^* (1 - \phi_T^* - \phi_H^*)] \\ B_{13} &= -\phi_T^* \phi_H^* \\ B_{22} &= c [\hat{\alpha} \phi_T^* (1 - \phi_{R_T}^*) + \hat{\beta} \phi_{R_T}^* (1 - \phi_T^* - \phi_H^*)] \\ B_{23} &= 0 \\ B_{33} &= \phi_T^* \phi_H^* + \hat{\delta}_2 \phi_H^* \end{aligned} \quad (3.24)$$

Here we have set  $\xi_1 = \xi_T$ ,  $\xi_2 = \xi_{R_T}$ ,  $\xi_3 = \xi_H$ . In principle, by solving equation (3.22) one can quantify the deviation from the ideal mean–field dynamics. As we aim at elucidating

the emergence of regular cycles induced by stochasticity, it is convenient to map the problem into an equivalent setting of Langevin type, which takes the explicit form:

$$\frac{d\xi_i}{d\tau} = A_i(\underline{\xi}) + \eta_i(\tau) \quad (3.25)$$

where the term  $\eta_i$  is a Gaussian noise with zero mean and with correlation given by

$$\langle \eta_i(\tau) \eta_j(\tau') \rangle = B_{ij} \delta(\tau - \tau')$$

Here  $i, j = 1, \dots, 3$  with  $1 = T$ ,  $2 = R_T$  and  $3 = H$ .

To bring into evidence any possible oscillatory regime, we perform a Fourier analysis and calculate the associated power spectrum. Following [7], we take the Fourier transform of (3.25) obtaining

$$-i\omega \tilde{\xi}_i(\omega) = \sum_j M_{ij} \tilde{\xi}_j(\omega) + \tilde{\eta}_i(\omega)$$

where we have denoted by the tilde the Fourier transform. Introducing the matrix  $\Phi = -i\omega I - M$ , the previous relation may be written as

$$\sum_j \Phi_{ij}(\omega) \tilde{\xi}_j(\omega) = \tilde{\eta}_i(\omega) \quad (3.26)$$

and the Fourier transform of  $\eta_i(\omega)$  has the following correlation function

$$\langle \tilde{\eta}_i(\omega) \tilde{\eta}_j(\omega') \rangle = B_{ij} (2\pi) \delta(\omega + \omega')$$

Equation (3.26) gives

$$\tilde{\xi}_i(\omega) = \sum_j \Phi_{ij}^{-1} \tilde{\eta}_j(\omega)$$

and averaging the squared modulus of  $\tilde{\xi}_i(\omega)$  we obtain the analytical expression of the power spectrum

$$P_i(\omega) = \langle |\tilde{\xi}_i(\omega)|^2 \rangle = \sum_j \sum_k \Phi_{ij}^{-1}(\omega) B_{jk} (\Phi_{ij}^\dagger)^{-1}(\omega) \quad (3.27)$$

where  $\Phi_{ij}^\dagger(\omega) = \Phi_{ji}(-\omega)$ .

Bound receptors might be assumed as quantifying the drug compound action: The largest the number of bound receptor, here labeled  $R_T$ , the more effective the analgesic in reducing the pain. This is of course a simplistic picture which does not weight the certainly relevant contribution associated to the subsequent cascade of reactions (signal transduction) engendered by a successful binding event. As we shall be discussing in a separate contribution, the model can be made more realistic by accounting for such an additional effect.

Motivated by the willing of unraveling regular patterns in the population of bound receptors, we calculate the power spectrum defined by (3.27) for the case of interest  $i = 2$ . After some algebraic manipulations,  $P_2(\omega)$  can be put in the form of a fractional polynomial of the type

$$P_2(\omega) = \frac{c_0 + c_2\omega^2 + c_4\omega^4}{d_0 + d_2\omega^2 + d_4\omega^4 + d_6\omega^6} \quad (3.28)$$

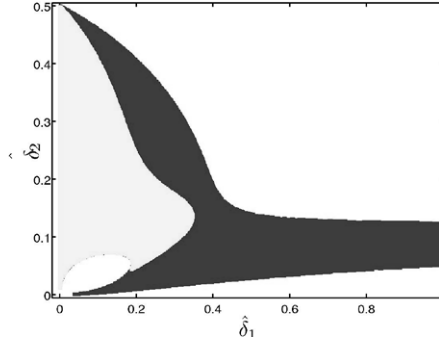


Figure 3.4: A subset of point (lighter region) is identified which leads to an oscillatory behavior of the acquired stochastic series for  $R_T$ . Such a region is delimited on the basis of an analytical perturbative treatment, see equation (3.27).

where  $c_i$  and  $d_i$  depends on the parameters of the model and on the equilibrium point  $\phi_2^*$ <sup>7</sup>. This is a symmetric function with respect to the axis  $\omega = 0$ , and goes to zero when  $\omega \rightarrow \infty$ . At most two maxima (peaks) are possible, depending on the number of real roots admitted by its derivative. Scanning the parameter space of Fig. 3.2 we discover that only a subset of pairs  $(\hat{\delta}_1, \hat{\delta}_2)$  yielding to damped oscillations in the mean field regime, do admit a peak in  $P_2(\omega)$ . The (in principle possible) two peaked profile is not being found within the explored parameters range. The lighter region in Fig. 3.4 highlights the portion of space corresponding to the predicted oscillatory behavior for  $R_T$ .

To validate our finding we turn to direct, Gillespie based, stochastic simulations and choose the parameters that are expected to lead to a peaked power spectrum. This latter is calculated averaging over many independent stochastic runs and then compared to the theoretical curve (3.27), in Fig. 3.5. A good agreement is found. The existence of a pick in the power spectrum implies that the concentration of bound receptors will undergo significant time oscillations induced by the graininess intrinsic to the medium being simulated.

### 3.3 On the general case where $\hat{\eta}_2 \neq 0$

Let us consider the general scenario where renewing of  $H$  molecules is also allowed, implying  $\hat{\eta}_2 \neq 0$ . In this case the mean-field system (3.10)–(3.12) admits only one equi-

<sup>7</sup> Also in this case we do not report the explicit expressions of the coefficients  $c_i$  and  $d_i$  as they do involve hundreds of terms.

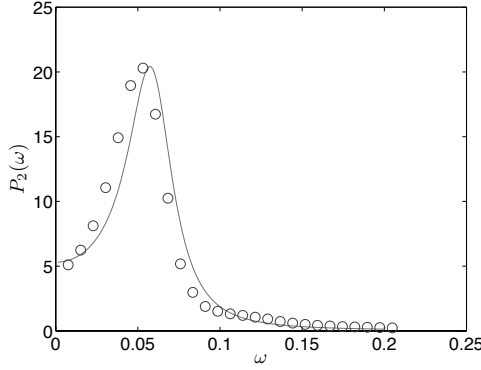


Figure 3.5: A plot of the power spectrum relative to species  $R_T$  as a function of frequency  $\omega$ . The symbols represent the profile calculated from 500 independent runs of the stochastic simulations, while the solid line stands for the theoretical prediction based on equation (3.27). Parameters are those listed in the caption of Fig. 3.3.

librium point  $\underline{\phi}^* = (\phi_T^*, \phi_H^*, \phi_{RT}^*)$  with:

$$\begin{aligned}\phi_T^* &= \frac{(1 + \hat{\sigma})\hat{\eta}_2 + \hat{\eta}_1 - D_1}{2 \left[ (1 + \hat{\sigma})\hat{\eta}_2 + \hat{\delta}_1 + \hat{\eta}_1 \right]} \\ \phi_H^* &= \frac{(1 + \hat{\sigma})\hat{\eta}_2 + \hat{\eta}_1 + D_1}{2 \left[ (1 + \hat{\sigma})(\hat{\delta}_2 + \hat{\eta}_2) + \hat{\eta}_1 \right]} \\ \phi_{RT}^* &= \left\{ 1 - \frac{\hat{\beta}\hat{\alpha}^{-1} \left[ (1 + \hat{\sigma})\hat{\delta}_2 - \hat{\delta}_1 \right] \left[ (1 + \hat{\sigma})\hat{\eta}_2 + \hat{\eta}_1 + D_1 \right]}{\left[ (1 + \hat{\sigma})(\hat{\delta}_2 + \hat{\eta}_2) + \hat{\eta}_1 \right] \left[ D_1 - (1 + \hat{\sigma})\hat{\eta}_2 - \hat{\eta}_1 \right]} \right. \\ &\quad \left. - \frac{2\hat{\beta}\hat{\alpha}^{-1}\hat{\delta}_1 \left[ (1 + \hat{\sigma})(\hat{\delta}_2 + \hat{\eta}_2) + \hat{\eta}_1 \right]}{\left[ (1 + \hat{\sigma})(\hat{\delta}_2 + \hat{\eta}_2) + \hat{\eta}_1 \right] \left[ D_1 - (1 + \hat{\sigma})\hat{\eta}_2 - \hat{\eta}_1 \right]} \right\}^{-1}\end{aligned}$$

where

$$D_1 = -\hat{\delta}_1\hat{\delta}_2 - \hat{\eta}_1\hat{\delta}_2 - \hat{\delta}_1\hat{\eta}_2 + \sqrt{A^2 + 4\hat{\eta}_2\hat{\delta}_1 \left[ (1 + \hat{\sigma})(\hat{\delta}_2 + \hat{\eta}_2) + \hat{\eta}_1 \right]}$$

and  $A = (1 + \hat{\sigma})\hat{\eta}_2 + \hat{\eta}_1 - \hat{\delta}_1\hat{\delta}_2 - \hat{\eta}_1\hat{\delta}_2 - \hat{\delta}_1\hat{\eta}_2$ .

Also in this case we are interested in studying the emergence of cycles and so we follow the procedure outlined above. Due to technical difficulties in carrying out algebraic manipulations within the generalized formulation, we proceed with a numerically assisted investigation. It shall be however emphasized that the van Kampen calculation can be straightforwardly extended to the case where  $\hat{\eta}_2 \neq 0$ . This case, in fact, is immediately recovered by replacing  $M_{31} \rightarrow M_{31} - \hat{\eta}_2$  and  $M_{33} \rightarrow M_{33} - \hat{\eta}_2$  in matrix (3.23), and  $B_{33} \rightarrow B_{33} + \hat{\eta}_2(1 - \phi_T^* - \phi_H^*)$  in matrix 3.24. Analytical prediction for the peak

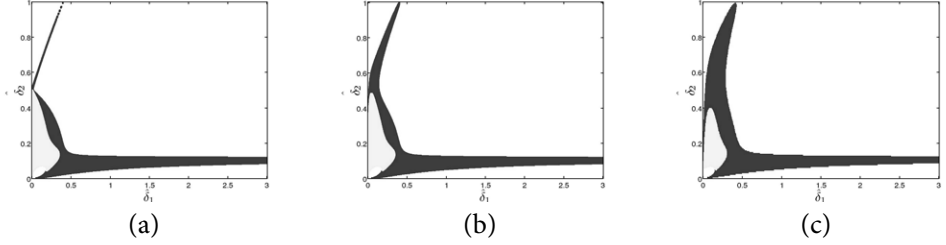


Figure 3.6: Scanning the parameters space  $(\hat{\delta}_1, \hat{\delta}_2)$ : Dark patches are associated to complex eigenvalues for  $\underline{\phi}^*$ , while a lighter color is used to trace the subdomain where a peaked power spectrum is found for the  $R_T$  species. Here  $N_1 = 4000$ ,  $N_2 = 9000$ ,  $\hat{\alpha} = 0.9$ ,  $\hat{\beta} = 0.6$ ,  $\hat{\sigma} = 0.5$ ,  $\hat{\eta}_1 = \hat{\delta}_1$ ,  $\hat{\eta}_2 = 0.000001$  for panel (a),  $\hat{\eta}_2 = 0.001$  for panel (b), and  $\hat{\eta}_2 = 0.0099$  for panel (c). We notice that also in this case the numerically calculated power spectrum is correctly interpolated by the theoretical curve obtained within the van Kampen expansion (data not shown).

profile are hence obtained and here used to discriminate the parameters' values which lead to an amplification of the stochastic oscillations. The results of this study are discussed in the following: First we start by considering,  $\hat{\eta}_1 = \hat{\delta}_1$ , in analogy with the above analysis. Then we relax this latter condition and allow  $\hat{\eta}_1, \hat{\eta}_2, \hat{\delta}_1, \hat{\delta}_2$  to change freely.

### 3.3.1 Assuming $\hat{\eta}_1 = \hat{\delta}_1$

To make contact with the analysis of Section 3.2.1 we start by imposing  $\hat{\eta}_1 = \hat{\delta}_1$ . Using the explicit van Kampen prediction for the power spectrum profile, we scanned the parameter plan  $(\hat{\delta}_1, \hat{\delta}_2)$ , looking for the presence of a peaked profile. Results are displayed in 3.6 where three different values of the  $\hat{\eta}_2$  are being considered. Dark patches identify region where complex eigenvalues are found for the dynamics linearized around  $\underline{\phi}^*$ . The superimposed lighter domains define instead the parameters' range where a peak is observed for the power spectrum relative to the molecules of type  $R_T$ .

For small values of  $\hat{\eta}_2$ , the obtained diagrams resembles pretty closely that reported in Fig. 3.6. Increasing the value of  $\hat{\eta}_2$ , the region which yields to complex eigenvalues expands, while the subdomain corresponding to a cyclic dynamics shrinks.

### 3.3.2 General case

As anticipated we now consider the general setting where the parameters  $\hat{\eta}_1, \hat{\eta}_2, \hat{\delta}_1, \hat{\delta}_2$  can be independently adjusted. Results are reported in Fig. 3.7, where now a three dimensional plot is introduced. The other reaction parameters are frozen to the values employed before. The qualitative conclusions reached holds, however, in general, as confirmed by a campaign of simulations, not reported here. A significant, densely connected, region of the parameter space is systematically detected for which oscillations induced by the stochastic component of the dynamics are present.

Panels (d)–(f) represents the projections of the three–dimensional plots on the plane

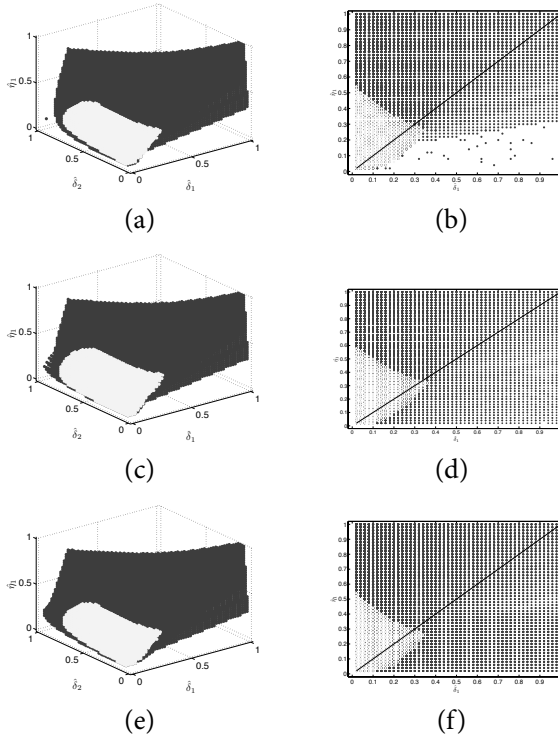


Figure 3.7: Analyzing the three-dimensional parameters space  $(\hat{\delta}_1, \hat{\delta}_2, \hat{\eta}_1)$ . Dark domain is associated to complex eigenvalues for  $\underline{\phi}^*$ , while the lighter region represents the subset where oscillations in the  $R_T$  time series are present. Here  $N_1 = 4000$ ,  $N_2 = 9000$ ,  $\hat{\alpha} = 0.9$ ,  $\hat{\beta} = 0.6$ ,  $\hat{\sigma} = 0.5$ ,  $\hat{\eta}_1 = \hat{\delta}_1$ ,  $\hat{\eta}_2 = 0.000001$  for panel (a) and (b),  $\hat{\eta}_2 = 0.001$  for panel (c) and (d),  $\hat{\eta}_2 = 0.0099$  for panel (e) and (f).

$\hat{\delta}_1 \hat{\eta}_1$ . Oscillations in the number of bound receptors are frequently occurring when  $\hat{\eta}_1 > \hat{\delta}_1$ , a condition that corresponds to having the incoming rate of active species, larger than the associated removal probability. In other words, translating this conclusion into a sound medical interpretation, we might be inclined to expect large oscillations in the experienced perception of pain when exceedingly massive doses of analgesic are administered. To illustrate the phenomenon, we report in Fig. 3.8 a typical stochastic simulation, together with the corresponding mean-field solution.

Indeed, the above discussion applies to relatively large population amount. When instead  $N_2$  gets smaller (the threshold being sensitive to the actual value of  $\hat{\eta}_2$ ), the system approaches a so called absorbing boundary, and the van Kampen ansatz breaks down. More specifically, the system switches between the two attractive states of the dynamics (the stationary state  $\underline{\phi}^*$ , and the equilibrium point  $\underline{\phi}_1^*$  characteristic of the model for  $\hat{\eta}_2 = 0$ ), the number of  $\bar{H}$  molecule becoming occasionally zero. This process is responsible for continuous, though unpredictable swing in the number of bound receptor, yet another dynamical regimes where analgesic might prove substantially ineffective.

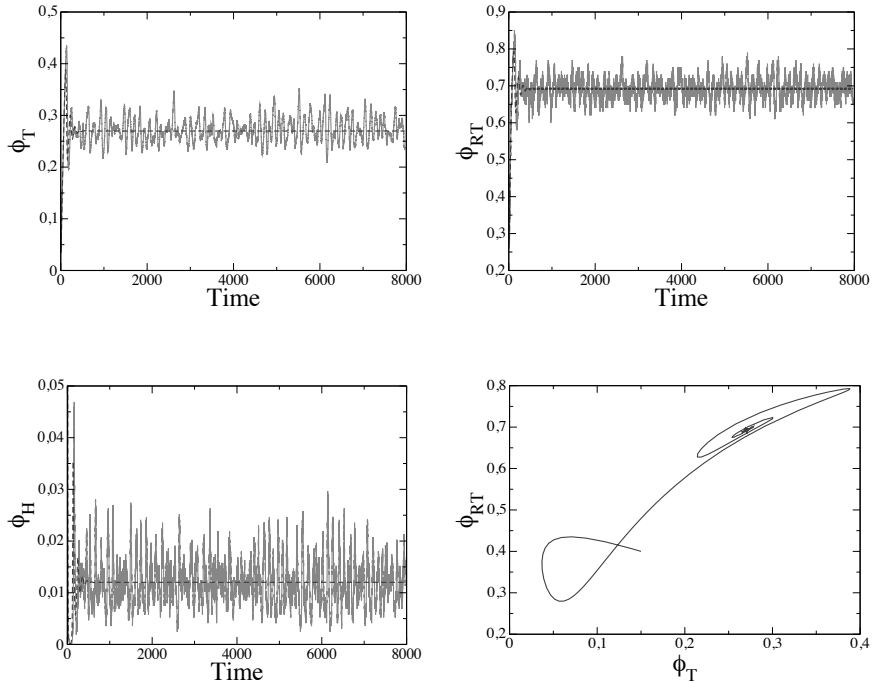


Figure 3.8: Comparison of stochastic simulations (solid lines) and the mean-field numerical solution (dashed line). Parameters used for the simulations are  $N_1 = 1000$ ,  $N_2 = 9000$ ,  $\hat{\alpha} = 0.1$ ,  $\hat{\beta} = 1.67 \cdot 10^{-2}$ ,  $\hat{\sigma} = 0.2$ ,  $\hat{\eta}_1 = 6.67 \cdot 10^{-3}$ ,  $\hat{\eta}_2 = 3.33 \cdot 10^{-6}$ ,  $\hat{\delta}_1 = 3.33 \cdot 10^{-3}$  and  $\hat{\delta}_2 = 0.27$ .

We notice that this is a general property of the model, which can be encountered also in the simplified settings discussed above. To report on this intriguing phenomenon we represent in Fig. 3.10 two typical realizations (resp. for  $\hat{\eta}_1 \neq \hat{\delta}_1$  and  $\hat{\eta}_1 = \hat{\delta}_1$ ) for which it is found to occur.

As a final remark, let us stress that the process of signal transduction can be further detailed by elaborating on the receptors activity, following the lines of [68]. It can be shown (data not displayed) that the main conclusions here reached still hold under such general, and more realistic, conditions.

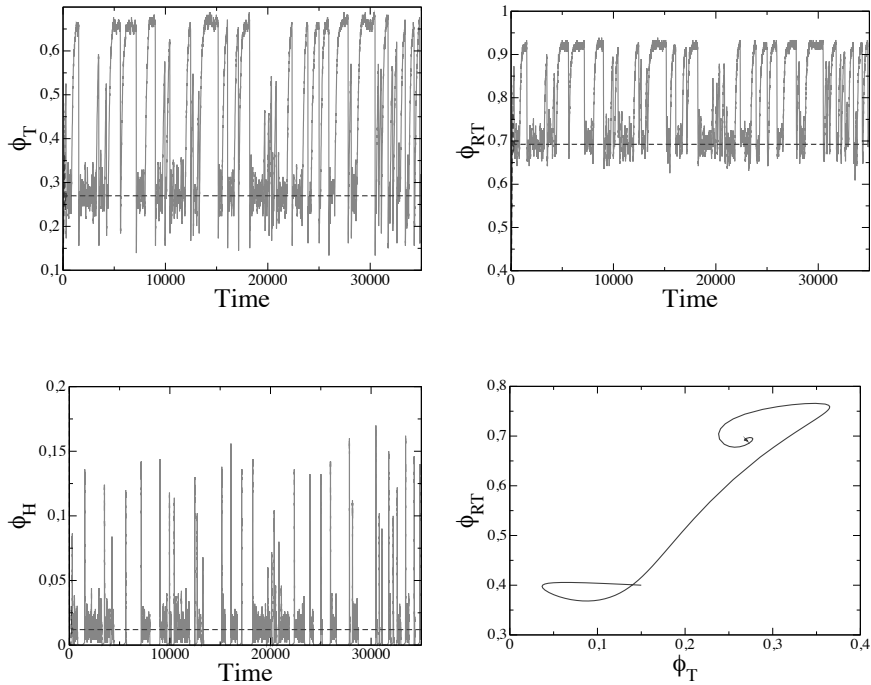


Figure 3.9: Comparison of stochastic simulations (solid lines) and the mean-field numerical solution (dashed line). Parameters used for the simulations are  $N_1 = 2000$ ,  $N_2 = 2500$ ,  $\hat{\alpha} = 0.1$ ,  $\hat{\beta} = 1.67 \cdot 10^{-2}$ ,  $\hat{\sigma} = 0.2$ ,  $\hat{\eta}_1 = 6.67 \cdot 10^{-3}$ ,  $\hat{\eta}_2 = 3.33 \cdot 10^{-6}$ ,  $\hat{\delta}_1 = 3.33 \cdot 10^{-3}$  and  $\hat{\delta}_2 = 0.27$ . The stochastic simulations display a switching between the equilibrium point of the system and the trivial equilibrium point of the system for  $\hat{\eta}_2 = 0$ . In this case,  $\underline{\phi}_1^* = (0.667, 0.923, 0)$ .

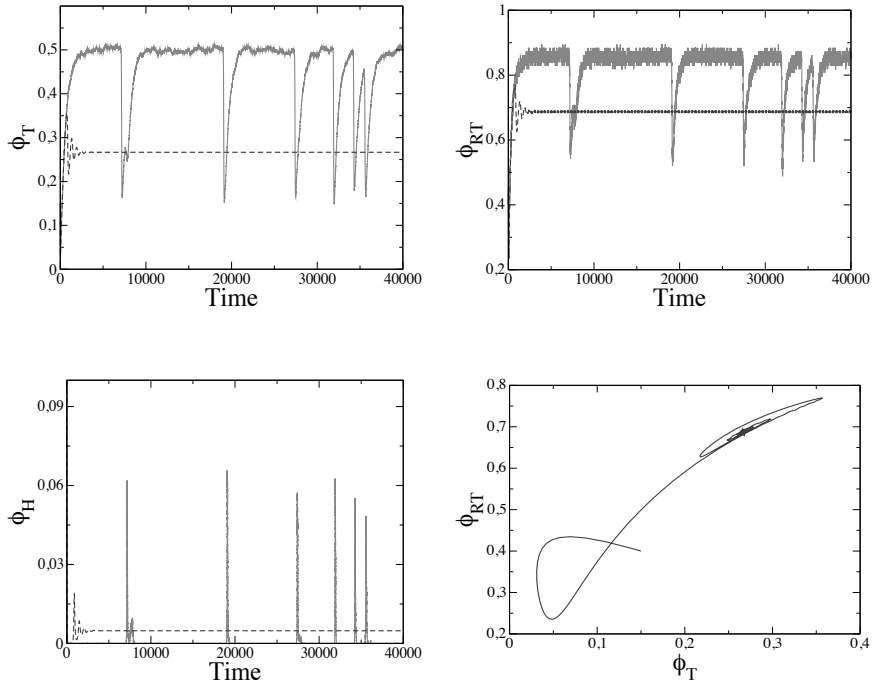


Figure 3.10: Comparison of stochastic simulations (solid lines) and the mean-field numerical solution (dashed line). Parameters used for the simulations are  $N_1 = 1000$ ,  $N_2 = 9000$ ,  $\hat{\alpha} = 0.1$ ,  $\hat{\beta} = 1.67 \cdot 10^{-2}$ ,  $\hat{\sigma} = 0.2$ ,  $\hat{\eta}_1 = \hat{\delta}_1 = 3.33 \cdot 10^{-3}$ ,  $\hat{\eta}_2 = 3.33 \cdot 10^{-7}$  and  $\hat{\delta}_2 = 0.27$ . The stochastic simulations display a switching between the equilibrium point of the system and the trivial equilibrium point of the system for  $\hat{\eta}_2 = 0$ . In this case,  $\underline{\phi}_1^* = (0.5, 0.86, 0)$ .

## Chapter 4

### A stochastic approach to the coupled parent drug and metabolite dynamics

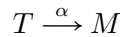
As outlined in the previous chapter, stochastic effects might be important when interested at describing the interaction between molecules. In particular, we have so far analyzed the interplay between analgesics and the corresponding target receptors. In this chapter we take one loop forward by developing a model which includes the possibility for the analgesic to undergo a biotransformation into metabolites, a distinct family of molecules which competes with the parent drug for the same receptors. More specifically, it is important to account for the peculiar role of different metabolites, which can arise from the genetic variability of the enzymes responsible for the biotransformation. These variations may substantially affect the individual response to the therapy, as commonly experienced in the medical practice. Detecting genetic variations in drug-metabolizing enzymes becomes e.g. essential for identifying individuals for which adverse drug reactions to standard doses of certain medications are expected. Individuals carrying cytochrome poor metabolizer variants exhibit different pharmacokinetics properties as compared to control subjects. As a result, non-conventional doses of medications are to be eventually required so to sustain the involved cytochrome activity for biotransformation. Conversely, medications that are not processed via cytochrome biotransformation, can be preferentially selected for those patients with potentially impaired cytochrome metabolic capacity. Although we here make specific reference to the case of tramadol, the model here discussed is rather general and can be hence invoked within other contexts where metabolization and ligand-receptors interactions do occur.

In the next section we introduce the stochastic model in term of the associated chemical equations. The underlying master equation is also specified. In section 4.2, we recover the mean-field system which formally applies to the limit of infinite microscopic constituents. The fixed points of the mean-field model are studied, as well as their associated stability. As we shall pinpoint in the following, depending on the chemical parameters the drug act with a different degree of effectiveness, that we here quantify. Also, the transient dynamics present intriguing features, that we bring into evidence. Section 4.3 is devoted to investigating the role of fluctuations which are analytically studied via the van Kampen's expansion already applied in the previous chapter. Numerical simulations are performed to corroborate our findings.

#### 4.1 Description of the model

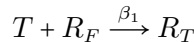
The bloodstream in the vicinity of the target receptor is assumed to be populated by two species of molecules, the parent drug tramadol and the main metabolite M1. Notice that, in general, metabolization and binding events occur in different parts of the body. Diffusion between sequentially ordered compartments should be in principle considered. In the present formulation space is however not explicitly incorporated and the reactions happen, according to their associated probability, within a unique bulk where molecules are uniformly stirred. As anticipated the solely biological processes here addressed are hence the metabolization and the reversible chemical reactions between the molecules and the free target receptors. As a side comment, we also emphasize that competition with other molecular entities dispersed in the medium could be possibly included in the picture. This important aspects are discussed in [66, 69], as well as the preceding chapter.

The process of biotransformation through the cytochromes gives rise to the metabolites. Here we hypothesize that the cytochromes are present in great quantity in the body, so that metabolization does not depend on their associated concentration, and proceeds as a spontaneous transformation at constant rate. Denoting with  $T$  the molecule of tramadol, and assuming  $M$  to label the metabolite of type M1, the process of metabolization is re-conducted to the following chemical reaction

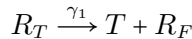


where  $\alpha$  is the reaction constant. This is the parameter which quantifies the ability of the body to metabolize the drug and can be hence supposed to be intimately connected to the genetic polymorphisms of the cytochrome CYP2D6.

Tramadol sailing in the bloodstream can eventually encounter a free target receptor, hereafter labeled  $R_F$ . Following a successful binding event the receptor  $R_F$  changes into an occupied element  $R_T$ . In formulae:

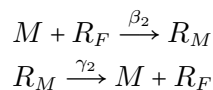


We further assume that during the binding the chemical properties of  $T$  remain unaltered. It may hence occasionally occur that  $R_T$  undergoes the inverse transformation by realizing a, still active,  $T$  molecule. This assumption translates into



The two parameters  $\beta_1$  and  $\gamma_1$  are the constant reaction rates.

To complete the model, we have to include the interaction between metabolites and receptors. The medical literature reports on the specificity of tramadol and metabolites to the different classes of receptors involved in pain mechanism, and their role in achieving analgesia. Here, we set down to consider a simplified scenario, where the parent drug and metabolite bind to the same type of receptors. More specifically, we shall assume, in analogy with the above, the following reactions' scheme for  $M$ :



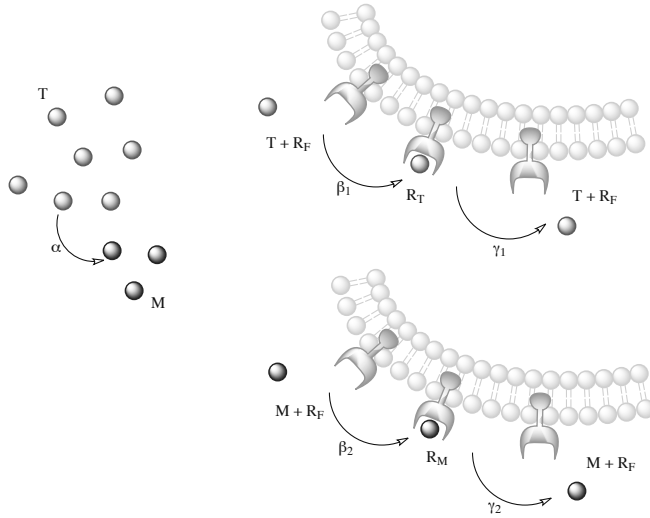


Figure 4.1: Chemical equations and schematic representation of the model. A tramadol molecule ( $T$ ) turns into metabolite ( $M$ ) with rate  $\alpha$ , and it can bind to a free receptor  $R_F$  with rate  $\beta_1$ . The spontaneous detachment of the compound  $R_T$  occurs with rate  $\gamma_1$ . Molecules of type  $M$  bind and unbind to  $R_F$  with rate  $\beta_2$  and  $\gamma_2$ .

where now  $R_M$  is the compound receptor–metabolite, and  $\beta_2$  and  $\gamma_2$  stand for the associated (forward and backward) rates.

The cartoon in Fig. 4.1 depicts the reactions network that we imagine to characterize our model.

How to quantify the sensation of pain within the proposed picture? As already remarked in chapter 3, we imagine that the more the bound receptors the less the experienced pain. In other words, the ideal condition where all available receptors were screened by a pool of injected drug ( $T$  or  $M$ ) molecules, would correspond to achieving complete analgesia. In future perspective the model could be complemented by accommodating for the signal transduction pathway, and so accurately representing the neural activity steps involved in the process.

Another comment is mandatory at this point. We have in fact deliberately decided to disregard the elimination of tramadol and metabolites from the body. Elimination is indeed crucial and leads to the final absorbing state where the concentration of  $T$  and  $M$  are both zero. However, and being at present interested with elucidating the local interaction of drugs and receptors, we hypothesized the elimination to proceed on a different (sensibly longer) time scale. Under this working assumption we do imagine to focus on a sequence of snapshots of the (relatively faster) interaction dynamics, where the global number of microscopic actors can be assumed as constant.

Moreover, we can certainly assume that the total number of receptors does not change with time (degradation is also happening with a different characteristic time). Denoting with  $n_i$  the number of molecules belonging to the  $i$ -th species, for  $i = T, M, R_T, R_M$ ,

$R_F$ , the following constrains are in conclusion put forward:

$$\begin{aligned} n_T + n_M + n_{R_T} + n_{R_M} &= N_1 \\ n_{R_F} + n_{R_T} + n_{R_M} &= N_2 \end{aligned}$$

where  $N_1$  represents the total number of molecules, while  $N_2$  refers to the total number of receptors. We can use these relations to express  $n_{R_M}$  and  $n_{R_F}$  in terms of the other independent variables, namely  $n_{R_M} = N_1 - n_T - n_M - n_{R_T}$  and  $n_{R_F} = N_2 - N_1 + n_T + n_M$ , so that the state of the system is given by the three dimensional vector  $\underline{n} = (n_T, n_M, n_{R_T})$ .

Within this framework, we are able to write the transition probabilities for the system to go from initial state  $\underline{n}$  to the final (allowed) state  $\underline{n}'$ . Such a probability is labeled  $T(\underline{n}'|\underline{n})$ . In our system only transitions from  $\underline{n}$  to  $(n_T - 1, n_M + 1, n_{R_T})$ ,  $(n_T \pm 1, n_M, n_{R_T} \mp 1)$  and  $(n_T, n_M \pm 1, n_{R_T})$  can take place. The corresponding nonzero  $T(\underline{n}'|\underline{n})$  entries are

$$\begin{aligned} T(n_T - 1, n_M + 1, n_{R_T}|\underline{n}) &= \alpha n_T \\ T(n_T - 1, n_M, n_{R_T} + 1|\underline{n}) &= \beta_1 n_T \frac{(N_2 - N_1 + n_T + n_M)}{N} \\ T(n_T, n_M - 1, n_{R_T}|\underline{n}) &= \beta_2 n_M \frac{(N_2 - N_1 + n_T + n_M)}{N} \\ T(n_T + 1, n_M, n_{R_T} - 1|\underline{n}) &= 2\gamma_1 n_{R_T} \\ T(n_T, n_M + 1, n_{R_T}|\underline{n}) &= 2\gamma_2 (N_1 - n_T - n_M - n_{R_T}) \end{aligned}$$

where  $N = N_1 + N_2$ .

Transition probabilities allow us to write down a master equation which governs the time evolution of the probability  $P(\underline{n}, t)$ , namely the probability of having the system in state  $\underline{n}$  at time  $t$ . The rate of change of  $P(\underline{n}, t)$  is simply given by the sum of the transitions towards  $\underline{n}$ , minus the outward transitions propagating from that state. In mathematical notation:

$$\begin{aligned} \frac{d}{dt}P(\underline{n}, t) &= T(\underline{n}|n_T + 1, n_M - 1, n_{R_T})P(n_T + 1, n_M - 1, n_{R_T}, t) \\ &+ T(\underline{n}|n_T + 1, n_M, n_{R_T} - 1)P(n_T + 1, n_M, n_{R_T} - 1, t) \\ &+ T(\underline{n}|n_T, n_M + 1, n_{R_T})P(n_T, n_M + 1, n_{R_T}, t) \\ &+ T(\underline{n}|n_T - 1, n_M, n_{R_T} + 1)P(n_T - 1, n_M, n_{R_T} + 1, t) \\ &+ T(\underline{n}|n_T, n_M - 1, n_{R_T})P(n_T, n_M - 1, n_{R_T}, t) \\ &- \left[ T(n_T - 1, n_M + 1, n_{R_T}|\underline{n}) + T(n_T - 1, n_M, n_{R_T} + 1|\underline{n}) \right. \\ &+ T(n_T, n_M - 1, n_{R_T}|\underline{n}) + T(n_T + 1, n_M, n_{R_T} - 1|\underline{n}) \\ &\left. + T(n_T, n_M + 1, n_{R_T}|\underline{n}) \right] P(\underline{n}, t) \end{aligned} \quad (4.1)$$

with null initial and boundary conditions.

We have by now formulated our discrete stochastic model and specified the transition probabilities between the admissible states. The (exact) master equation could

be, in principle, solved to obtain a closed expression for the expected probability at time  $t$ . This task turns out impossible and one has to resort to approximate solution. In first place, as discussed in the next section, the mean-field limit (namely  $N_1 \rightarrow \infty$ ,  $N_2 \rightarrow \infty$ ) is recovered following the standard procedure applied in the previous chapter. Then fluctuations around the mean-field dynamics are considered via the perturbative techniques.

#### 4.2 The deterministic limit

Multiplying both sides of equation (4.1) by  $n_T$  and summing over all states, we obtain

$$\frac{d}{dt} \sum_{\underline{n}} n_T P(\underline{n}, t) = \sum_{\underline{n}} \left[ T(n_T + 1, n_M, n_{R_T} - 1 | \underline{n}) - T(n_T - 1, n_M + 1, n_{R_T} | \underline{n}) - T(n_T - 1, n_M, n_{R_T} + 1 | \underline{n}) \right] P(\underline{n}, t)$$

where the summation variables have been shifted to simplify the expression. Substituting in for the transition rates and remembering that by definition

$$\sum_{\underline{n}} n_T P(\underline{n}, t) = \langle n_T \rangle$$

we have

$$\frac{d}{dt} \langle n_T \rangle = -\alpha \langle n_T \rangle - \frac{\beta_1}{N} \langle n_T (N_2 - N_1 + n_T + n_M) \rangle + 2\gamma_1 \langle n_{R_T} \rangle. \quad (4.2)$$

Applying the same method to the two other variables, we obtain the following differential equations

$$\begin{aligned} \frac{d}{dt} \langle n_M \rangle &= \alpha \langle n_T \rangle - \frac{\beta_2}{N} \langle n_M (N_2 - N_1 + n_T + n_M) \rangle \\ &\quad + 2\gamma_2 \langle N_1 - n_T - n_M - n_{R_T} \rangle \end{aligned} \quad (4.3)$$

$$\frac{d}{dt} \langle n_{R_T} \rangle = \frac{\beta_1}{N} \langle n_T (N_2 - N_1 + n_T + n_M) \rangle - 2\gamma_1 \langle n_{R_T} \rangle. \quad (4.4)$$

In the limit  $N \rightarrow \infty$  we can replace  $\langle n_i n_j \rangle = \langle n_i \rangle \langle n_j \rangle$  for every  $i, j$  in equations (4.2)–(4.4). In this way  $\langle n_i \rangle / N$  becomes the deterministic variable  $\phi_i$ , and we can write the mean-field system as:

$$\begin{aligned} \frac{d}{dt} \phi_T &= -\alpha \phi_T - \beta_1 \phi_T (\sigma + \phi_T + \phi_M) + 2\gamma_1 \phi_{R_T} \\ \frac{d}{dt} \phi_M &= \alpha \phi_T + 2\gamma_2 (\varphi - \phi_T - \phi_M - \phi_{R_T}) - \beta_2 \phi_M (\sigma + \phi_T + \phi_M) \\ \frac{d}{dt} \phi_{R_T} &= \beta_1 \phi_T (\sigma + \phi_T + \phi_M) - 2\gamma_1 \phi_{R_T} \end{aligned} \quad (4.5)$$

where  $\sigma = (N_2 - N_1) / N$  and  $\varphi = N_1 / N$ .

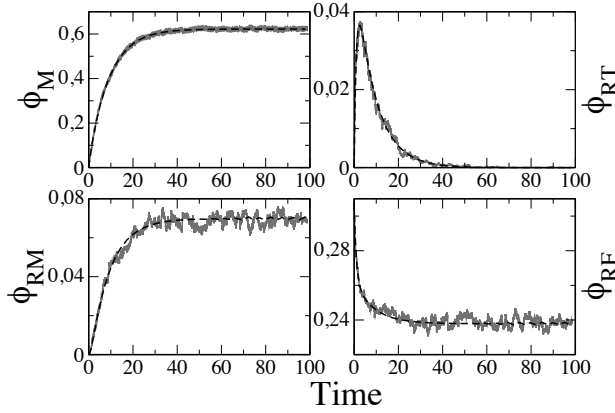


Figure 4.2: Metabolites and receptor densities as function of time. The solid (red) lines represent the stochastic simulation while the dashed (black) lines correspond to the numerical solution of the mean-field system. Parameters used are  $\alpha = 0.12$ ,  $\beta_1 = 0.23$ ,  $\beta_2 = 0.33$ ,  $\gamma_1 = 0.4$ ,  $\gamma_2 = 0.35$ ,  $N_1 = 4500$  and  $N_2 = 2000$ .

Figure 4. 2 shows the comparison between the stochastic behavior of the model and the mean-field one, as calculated by numerical integration of equations (4.5), dashed (black) line. The continuous (red) line is a typical stochastic simulation obtained through implementing the Gillespie algorithm (see appendix A). For each species, the two profiles overlap well: The approximate mean-field theory and the stochastic simulation agree, a part from corrections due to the finiteness of the simulated medium. As  $T$  is not continuously administered, its (number) concentration (as well that of  $R_T$ ) decays to zero. Conversely, the densities of the other species settle down to a steady-state value. This latter value and its stability properties are calculated in the following, where simple speculations on the medical relevance of our findings are also going to be addressed.

#### 4.2.1 Analysis of the macroscopic equations

To find the equilibrium point of the macroscopic equations, we set the time derivative to zero in system (4.5) and solve, obtaining the point  $\phi^* = (0, \phi_M^*, 0)$  where

$$\phi_M^* = \frac{-(2\gamma_2 + \beta_2\sigma) + \sqrt{(2\gamma_2 + \beta_2\sigma)^2 + 8\gamma_2\varphi\beta_2}}{2\beta_2}.$$

The stability of this point can be deduced from the Jacobian matrix

$$J(\phi^*) = \begin{pmatrix} -\alpha - \beta_1\sigma - \beta_1\phi_M^* & 0 & 2\gamma_1 \\ \alpha - 2\gamma_2 - \beta_2\phi_M^* & -2\gamma_2 - \beta_2\sigma - 2\beta_2\phi_M^* & -2\gamma_2 \\ \beta_1\sigma + \beta_1\phi_M^* & 0 & -2\gamma_1 \end{pmatrix}$$

whose eigenvalues are

$$\lambda_1 = -\sqrt{(2\gamma_2 + \beta_2\sigma)^2 + 8\gamma_2\varphi\beta_2} \quad (4.6)$$

$$\lambda_{2,3} = \frac{-(2\gamma_1 + \alpha + \beta_1\sigma + \beta_1\phi_M^*) \pm \sqrt{(2\gamma_1 + \alpha + \beta_1\sigma + \beta_1\phi_M^*)^2 - 8\gamma_1\alpha}}{2}. \quad (4.7)$$

These values are clearly negative and real, proving the system has a globally stable equilibrium point.

As explained in section 4.1, we here assess the effectiveness of the pharmacological treatment by measuring the number of bound receptors. However, recalling that the initial dose of tramadol is completely metabolized at equilibrium, we shall be solely interested with the quantity  $\phi_{R_M}^*$ . To visualize the asymptotic stage of the evolution we refer to the plan  $(\phi_{R_F}, \phi_{R_M})$  and therein trace the bisectrix (dashed line in Fig. 4.3a). Above the diagonal,  $\phi_{R_M}^* > \phi_{R_F}^*$ , the drug works better and the patient experience less pain. Such a condition realizes if

$$N_1 > \frac{\beta_2 + 4\gamma_2}{2(\beta_2 - 2\gamma_2)} N_2$$

and  $\beta_2 > 2\gamma_2$ . This means that the forward binding rate for the metabolite must be (at least) a factor two larger than the corresponding dissociation constant. Moreover, the initial dose of administered drug has to be chosen so that  $N_1$  is larger than (at least)  $N_2/2$ .

As it is shown in Fig. 4.3a, the equilibrium point is confined on the line  $N\phi_{R_M}^* + N\phi_{R_F}^* - N_2 = 0$ , which also defines the sub-domain of the plane which can be visited during the transient dynamics. Above that line in fact the positiveness of the variables is guaranteed. In Fig. 4.3b we project the numerical solutions of the system (4.5) in to the plane  $\phi_{R_F}^* \phi_{R_M}^*$ . The trajectories of the mean-field equations evolve towards the attractor. Starting from an arbitrary initial condition characterized by a generic value of  $n_{R_T}$  and  $n_{R_M}$ , the system gets apparently trapped into a transient phase which displays an almost constant number of bound receptors, sensibly different from that eventually achieved at equilibrium. Indeed, as testified by Fig. 4.3b, the number of bound receptors initially shrinks and only after, due to the action of newly injected chemicals, starts growing to approach the fixed point. This setting could correspond to mimicking the condition where a patient is exposed to a treatment which closely follows a preceding drug administration.

Furthermore, the characteristic time of equilibration can be estimated as the (absolute value of the) inverse of the maximum eigenvalue (4.6)–(4.7). This is an interesting indicator as it quantifies the ability of the system to eventually attain the asymptotic condition where the largest number of receptors is occupied. The data in Fig. 4.4 show that the relaxation time decreases as the metabolization rate increases, thus suggesting that the administered drug acts more rapidly for extensive.

### 4.3 The van Kampen expansion

Corrections to the mean-field dynamics can be calculated by resorting, with analogy to chapter 3, to the van Kampen's expansion. The main idea is to write the variables  $n_i$

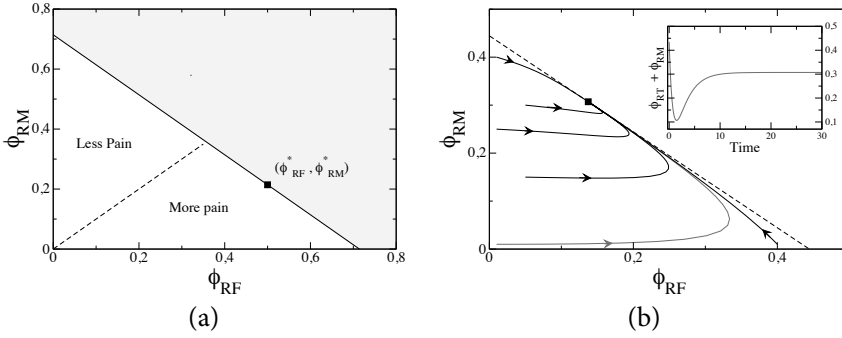


Figure 4.3: Panel (a) reports the projection of the equilibrium point into the plane  $\phi_{RF}\phi_{RM}$ . The two domains separated by the bisectrix are respectively labeled less/more pain, according to the prescriptions of the model (see main text) The colored (yellow) region denotes the portion of the plane where trajectories are not allowed. The solid black line correspond to the condition  $N\phi_{RM}^* + N\phi_{RF}^* - N_2 = 0$  (here  $N_1 = 2000$  and  $N_2 = 5000$ ) The equilibrium point (black square) belongs to this line. Panel (b) represents the projection of the trajectories on the plane  $\phi_{RF}\phi_{RM}$  for different initial conditions. Parameters used for the numerical integration of the mean-field system are  $\alpha = 0.7$ ,  $\beta_1 = 0.2$ ,  $\beta_2 = 0.9$ ,  $\gamma_1 = 0.8$ ,  $\gamma_2 = 0.05$ ,  $N_1 = 2500$  and  $N_2 = 2000$ . Inset: The time evolution of the total number of bound receptors,  $\phi_{RF} + \phi_{RM}$ , is reported. The curve is traced with reference to one specific initial condition, namely the red trajectory of the main panel.

as a sum of two contributions, namely  $n_i = N\phi_i(t) + \sqrt{N}\xi_i$ , where  $i = T, M, RT$ . Here  $\phi_i$  stands for the deterministic component, while  $\xi_i$  relates to the fluctuations. The new probability distribution function  $\Pi$  is hence defined as  $\Pi(\underline{\xi}, t) = P(\underline{n}, t)$  where  $\underline{\xi} = (\xi_T, \xi_M, \xi_{RT})$ . Moreover:

$$\frac{dP}{dt} = \frac{\partial \Pi}{\partial t} - \sqrt{N} \sum_{i=T, M, RT} \frac{d\phi_i}{dt} \frac{\partial \Pi}{\partial \xi_i}$$

To simplify the notation, it is practice to rewrite the master equation (4.1) in terms of step operators

$$\begin{aligned} \mathbb{E}_T^{\pm 1} f(\underline{n}, t) &= f(n_T \pm 1, n_M, n_{RT}) \\ \mathbb{E}_M^{\pm 1} f(\underline{n}, t) &= f(n_T, n_M \pm 1, n_{RT}) \\ \mathbb{E}_{RT}^{\pm 1} f(\underline{n}, t) &= f(n_T, n_M, n_{RT} \pm 1). \end{aligned}$$

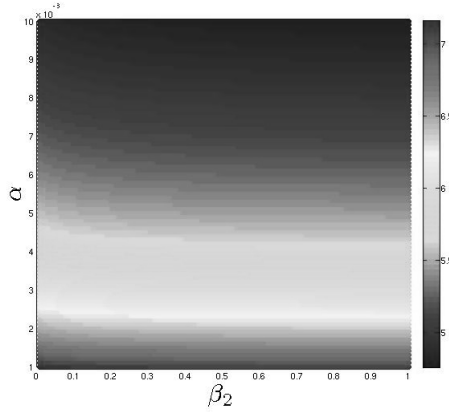


Figure 4.4: The color code (in logarithmic scale) refers to the slowest characteristic time of convergence to equilibrium as calculated from the linearized dynamics. We here scan the parameter plan  $(\alpha, \beta_2)$ . The other parameters are chose as  $\beta_1 = 0.3$ ,  $\gamma_1 = 0.5$ ,  $\gamma_2 = 0.1$ ,  $N_1 = 3000$ ,  $N_2 = 2500$

The master equation can be therefore cast in the form:

$$\begin{aligned}
\frac{d}{dt}P(\underline{n}, t) &= (\mathbb{E}_T^+ \mathbb{E}_M^- - 1) \alpha n_T P(\underline{n}, t) \\
&+ (\mathbb{E}_T^+ \mathbb{E}_{R_T}^- - 1) \frac{\beta_1}{N} n_T (N_2 - N_1 + n_T + n_M) P(\underline{n}, t) \\
&+ (\mathbb{E}_M^+ - 1) \frac{\beta_2}{N} n_M (N_2 - N_1 + n_T + n_M) P(\underline{n}, t) \\
&+ (\mathbb{E}_T^- \mathbb{E}_{R_T}^+ - 1) 2\gamma_1 n_{R_T} P(\underline{n}, t) \\
&+ (\mathbb{E}_M^- - 1) 2\gamma_2 (N_1 - n_T - n_M - n_{R_T}) P(\underline{n}, t) . \quad (4.8)
\end{aligned}$$

The operators  $\mathbb{E}_i^{\pm 1}$  change  $n_i$  in  $n_i \pm 1$  and so  $\xi_i$  in  $\xi_i \pm 1$ . They hence admit the following representation in terms of differential operators:

$$\mathbb{E}_i^{\pm 1} = 1 \pm N^{-1/2} \frac{\partial}{\partial \xi_i} + \frac{1}{2} N^{-1} \frac{\partial^2}{\partial \xi_i^2} \pm \dots . \quad (4.9)$$

Substituting relation (4.9) into (4.8) and collecting contributions of order  $\sqrt{N}$ , one recovers the mean-field system of coupled differential equations (4.5). Working out the next-to-leading order, namely  $N$ , one eventually obtains a Fokker Planck equation (FPE) which characterizes the fluctuations around the asymptotic mean-field solution. The FPE reads:

$$\frac{\partial \Pi}{\partial \tau} = - \sum_i \frac{\partial}{\partial \xi_i} (A_i(\underline{\xi}) \Pi) + \frac{1}{2} \sum_{ij} B_{ij} \frac{\partial^2 \Pi}{\partial \xi_i \partial \xi_j} \quad (4.10)$$

where

$$A(i\underline{\xi}) = \sum_j M_{ij} \xi_j .$$

The entries of matrix  $M$ , hereafter  $m_{ij}$ , those of  $B$ , labeled  $b_{ij}$ , are function of the chemical parameters of the model and read

$$\begin{aligned}
 m_{11} &= -[\alpha + 2\beta_1\phi_T + \beta_1\sigma + \beta_1\phi_M] \\
 m_{12} &= -\beta_1\phi_T \\
 m_{13} &= -2\gamma_1 \\
 m_{21} &= \alpha - \beta_2\phi_M - 2\gamma_2 \\
 m_{22} &= 2\beta_2\phi_M + \beta_2\sigma + \beta_2\phi_T + 2\gamma_2 \\
 m_{23} &= -2\gamma_2 \\
 m_{31} &= 2\beta_1\phi_T + \beta_1\sigma + \beta_1\phi_M \\
 m_{32} &= \beta_1\phi_T \\
 m_{33} &= -2\gamma_1
 \end{aligned} \tag{4.11}$$

and

$$\begin{aligned}
 b_{11} &= \beta_1\sigma\phi_T + \beta_1\phi_T^2 + \beta_1\phi_T\phi_M + \alpha\phi_T + 2\gamma_1\phi_{R_T} \\
 b_{12} &= -\alpha\phi_T \\
 b_{13} &= -[\beta_1\sigma\phi_T + \beta_1\phi_T^2 + \beta_1\phi_T\phi_M + 2\gamma_1\phi_{R_T}] \\
 b_{22} &= \beta_2\phi_M^2 + \beta_2\sigma\phi_M + \beta_2\phi_M\phi_T + 2\gamma_2\phi + (\alpha - 2\gamma_2)\phi_T - 2\gamma_2\phi_M - 2\gamma_2\phi_{R_T} \\
 b_{23} &= 0 \\
 b_{33} &= \beta_1\phi_T\sigma + \beta_1\phi_T^2 + \beta_1\phi_T\phi_M + 2\gamma_1\phi_{R_T}
 \end{aligned} \tag{4.12}$$

Equation (4.10) can be solved explicitly: The obtained probability distribution  $\Pi(\underline{\xi}, t)$  is a Gaussian and it is hence completely specified by its first and second moments. In the next section we shall calculate the associated moments explicitly and test the adequacy of the predictions versus direct simulations.

#### 4.3.1 Analysis of the fluctuations

To characterize the moments of the distribution we proceed as follows. We multiply both sides of the FPE (4.10) by  $\xi_i$  (resp.  $\xi_i\xi_j$ ) and integrate over all  $\underline{\xi}$ . One then recovers the equations for the mean value of the fluctuations  $\langle \xi_i \rangle$ , as well as for the associated correlations,  $\langle \xi_i \xi_j \rangle$ .

The evolution of the first moments is found to be governed by the following equations:

$$\begin{aligned}
 \frac{d}{dt} \langle \xi_T \rangle &= m_{11} \langle \xi_T \rangle + m_{12} \langle \xi_M \rangle + m_{13} \langle \xi_{R_T} \rangle \\
 \frac{d}{dt} \langle \xi_M \rangle &= m_{21} \langle \xi_T \rangle + m_{22} \langle \xi_M \rangle + m_{23} \langle \xi_{R_T} \rangle \\
 \frac{d}{dt} \langle \xi_{R_T} \rangle &= m_{31} \langle \xi_T \rangle + m_{32} \langle \xi_M \rangle + m_{33} \langle \xi_{R_T} \rangle
 \end{aligned} \tag{4.13}$$

while the the second moments obey to

$$\begin{aligned}
\frac{d}{dt}\langle \xi_T^2 \rangle &= 2m_{11}\langle \xi_T^2 \rangle + 2m_{12}\langle \xi_T \xi_M \rangle + 2m_{13}\langle \xi_T \xi_{RT} \rangle + b_{11} \\
\frac{d}{dt}\langle \xi_T \xi_M \rangle &= m_{21}\langle \xi_T^2 \rangle + (m_{11} + m_{22})\langle \xi_T \xi_M \rangle + m_{23}\langle \xi_T \xi_{RT} \rangle + m_{12}\langle \xi_M^2 \rangle \\
&\quad + m_{13}\langle \xi_M \xi_{RT} \rangle + b_{12} \\
\frac{d}{dt}\langle \xi_T \xi_{RT} \rangle &= m_{31}\langle \xi_T^2 \rangle + m_{32}\langle \xi_T \xi_M \rangle + (m_{11} + m_{33})\langle \xi_T \xi_{RT} \rangle \\
&\quad + m_{12}\langle \xi_M \xi_{RT} \rangle + m_{13}\langle \xi_{RT}^2 \rangle + b_{13} \\
\frac{d}{dt}\langle \xi_M^2 \rangle &= 2m_{21}\langle \xi_T \xi_M \rangle + 2m_{22}\langle \xi_M^2 \rangle + 2m_{23}\langle \xi_M \xi_{RT} \rangle + b_{22} \\
\frac{d}{dt}\langle \xi_M \xi_{RT} \rangle &= m_{31}\langle \xi_T \xi_M \rangle + m_{21}\langle \xi_T \xi_{RT} \rangle + m_{32}\langle \xi_M^2 \rangle \\
&\quad + (m_{22} + m_{33})\langle \xi_M \xi_{RT} \rangle + m_{23}\langle \xi_{RT}^2 \rangle \\
\frac{d}{dt}\langle \xi_{RT}^2 \rangle &= 2m_{31}\langle \xi_T \xi_{RT} \rangle + 2m_{32}\langle \xi_M \xi_{RT} \rangle + 2m_{33}\langle \xi_{RT}^2 \rangle + b_{33} \quad (4.14)
\end{aligned}$$

where the elements  $m_{ij}$  and  $b_{ij}$  are the entries of matrices (4.11) and (4.12).

The above system cannot be solved analytically (indeed we cannot even cast the mean-field solution in a closed analytic form). However, being interested in the fluctuations around the equilibrium point, once the initial transient has damped out, one sets to zero the time derivatives in system (4.13) and evaluates the coefficients  $m_{ij}$  at the equilibrium point  $\underline{\phi}^*$ . It turns out that  $\langle \xi_T \rangle^{st} = \langle \xi_M \rangle^{st} = \langle \xi_{RT} \rangle^{st}$ . Proceeding in a similar fashion with system (4.14), one readily finds that all the second moments are zero but  $\langle \xi_M^2 \rangle^{st}$  which instead reads

$$\langle \xi_M^2 \rangle^{st} = \frac{\beta_2 \phi_M^{*2} + (\beta_2 \sigma - 2\gamma_2) \phi_M^* + 2\gamma_2 \varphi}{2(2\beta_2 \phi_M^* + \beta_2 \sigma + 2\gamma_2)}$$

In this latter case the stationary probability distribution  $\Pi(\underline{\xi})^{st}$  is given by

$$\Pi(\underline{\xi})^{st} = \frac{1}{\sqrt{2\pi} \langle \xi_M^2 \rangle^{st}} \exp \left[ -\frac{\xi_M^2}{2 \langle \xi_M^2 \rangle^{st}} \right] \quad (4.15)$$

Figure 4.5a shows the projection of the stationary probability distribution  $\Pi^{st}$  on the plane  $(\phi_{RF}, \phi_{RM})$ . As it can be appreciated by visual inspection, the dispersion occurs along the direction given by  $N\phi_{RM}^* + N\phi_{RF}^* - N_2 = 0$  which also contains the equilibrium point. In Fig. 4.5b the stationary probability distribution  $\Pi^{st}$  is plotted as a function of  $\xi_M$ . The figure testifies on the predictive ability of equation (4.15) here depicted with a solid line, which is shown to interpolate correctly the numerical data (symbols).

Imagine now to partition the plane  $(\phi_{RF}, \phi_{RM})$  into two regions separated by the bisectrix. Moving above the diagonal, the number of screened receptors increases which in turn implies reducing the pain, within our simplified scenario. Fluctuations can facilitate the road towards analgesia, as outlined in Fig. 4.5a. The stationary probability

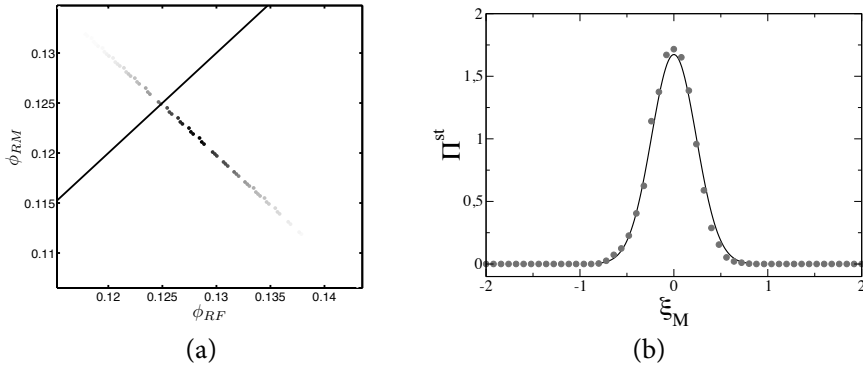


Figure 4.5: Panel (a) shows the projection of the stationary probability distribution  $\Pi^{st}$  on the original plane  $\phi_{RF}\phi_{RM}$ . The solid black line represents the bisectrix of the plane. Panel (b) reports the stationary probability distribution as a function of  $\xi_M$ . The solid line represents the theoretical prediction based on equation (4.15). The symbols refer to the Gillespie like numerical simulation. Here, the parameters are  $\alpha = 0.5$ ,  $\beta_1 = 0.2$ ,  $\beta_2 = 0.3$ ,  $\gamma_1 = 0.5$ ,  $\gamma_2 = 0.1$ ,  $N_1 = 3000$ , and  $N_2 = 1000$

distribution can be hypothetically employed to quantify the probability of entering the region in  $(\phi_{RF}, \phi_{RM})$  where the drug effect is supposedly more pronounced. This latter probability corresponds to the area of the distribution above the bisectrix and is quantified in  $p = 0.196$  for the chosen parameters' setting. Interestingly, although the mean-field solution predicts a stationary condition characterized by a pronounced sensation of pain ( $\phi_{RF}^* = 0.129$  and  $\phi_{RM}^* = 0.121$ ), there is a nonzero probability that, due to fluctuations, the system enters a region where pain is partially hindered. Obviously, this speculation applies as long as  $N$  is finite (though large). This is for instance the case where a local stimulus is applied which interests a finite patch of neurons (see for instance the whisker stimulation experiment [28]). In the general case where the number of involved receptors is exceedingly large, the mean-field dynamics takes over and the aforementioned distribution shrinks to a delta.

In the next chapter we shall move to considering a different case study, where the stochastic modeling proves fundamental. In particular, as anticipated in the introductory section, we will concentrate on analyzing an extended set of autocatalytic reactions which can be hypothesized to occur in a minimal model of cell.

## Chapter 5

### Extended auto-catalytic networks

Autocatalytic reactions have long fascinated physicists and chemists because of their unique features [70]. A chemical reaction is called autocatalytic if one of the reaction products is itself a catalyst for the chemical reaction. Part of the reason for the interest in these types of reactions stems from the fact that even if only a small amount of the catalyst is present, the reaction may start off slowly, but will quickly speed up once more catalyst is produced. If the reactant is not replaced, the process will again slow down producing the typical sigmoid shape for the concentration of the product. All this is for a single chemical reaction, but of greater interest is the case of many chemical reactions, where one or more reactions produce a catalyst for some of the other reactions. Then the whole collection of constituents is called an autocatalytic set [71]. In addition to the interesting properties of autocatalytic sets, there is also an intriguing possibility that “bootstrap” reactions such as this may have had an important role in producing complex or self-replicating molecules required for the origin of life on Earth [72, 73, 74, 75].

Theoretical studies of the properties of autocatalytic reactions are typically of two kinds. In the first, rate equations for the reactions are written down and these are either solved numerically or their properties investigated using the techniques used in the study of dynamical systems. An alternative is to carry out computer simulations of the actual reactions themselves. However, as outlined in the preceding discussion, a third strategy can be also employed: Using methods from the theory of stochastic processes an analytic approach to the full model (and not just the mean field version) is possible.

Occasionally, oscillatory behaviors manifest for a moderate number of constituents, a phenomenon which arise from the discrete nature of the system. As we pointed out earlier, these oscillations are purely stochastic in origin. The main tool that is here used to elaborate on their emergence in the autocatalytic setting is again the system-size expansion of van Kampen [64, 76] (see chapter 3).

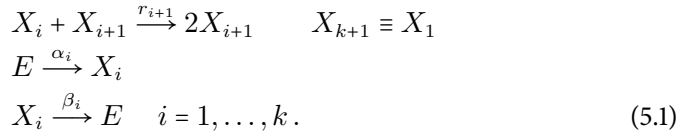
More specifically we shall consider the autocatalytic reaction scheme introduced by Togashi and Kaneko [77, 78]. In most autocatalytic reactions there are two types of constituent: the autocatalytic and the substrate. The number of the latter type are kept constant by continually feeding them in, however the former are not injected nor extracted from the system. In this sense the system is closed as far as the autocatalytic constituents are concerned, but open for the substrate. In the scheme that Togashi and Kaneko investigate, the reactions are cyclic, with  $k$  constituents  $X_1, \dots, X_k$  reacting according to  $X_i + X_{i+1} \rightarrow 2X_{i+1}$  with  $X_{k+1} \equiv X_1$ ,  $i = 1, \dots, k$ . The chemicals are assumed to be in a container which is well-stirred, but with the possibility of diffusing across the surface of the container into a particle reservoir.

Togashi and Kaneko [77, 78] used only computer simulation to study their proposed reaction scheme. At variance, and following the recipe of chapter 3 we shall proceed analytically by writing down the master equation for model at hand, and then studying it through a systematic expansion in  $N^{-1/2}$ , where  $N$  is the system size. To leading order one finds the rate equations which appear in [77], and to next-to-leading order a Langevin equation which describes the fluctuations about the stable fixed point of the rate equations. From previous work we expect that (i) this first-order correction will be sufficient to yield results which are in good agreement with simulation data, (ii) the large amplitude of the oscillations can be understood as a resonant effect. One of the strengths of the technique is that the next-to-leading order corrections give *linear* Langevin equations which can be analyzed exactly for arbitrary values of  $k$ .

As an additional step, we shall extend Togashi and Kaneko model to explicitly incorporate the notion of space. In doing so, the diffusion of the molecular species participating to the dynamics is consistently accounted for and spatio-temporal collective motions unraveled via a straightforward application of the van Kampen analysis. Section 5.2 is devoted to discuss this latter topic, combining the analytical and numerical viewpoints.

## 5.1 Enhanced stochastic oscillations in autocatalytic reactions

The autocatalytic reaction scheme described previously can be formulated as



Here  $r_i$ ,  $\alpha_i$  and  $\beta_i$  (with  $r_{k+1} \equiv r_1$ ), are the rates at which the reactions take place and  $E$  is the null constituent. Such constituents have to be included so that the number of molecules of type  $X_i$ ,  $n_i$ , are all independent. Figure 5.1 shows a schematic representation of these reactions. If the size of the system is denoted by  $N$ , then  $\sum_{i=1}^k n_i + n_E = N$ , where  $n_E$  is the number of null constituents. While  $N$  is fixed,  $n_E$  may vary as the total number of molecules changes with time. In practice,  $n_E$  does not explicitly appear in the formalism; it is always replaced by  $N - \sum_{i=1}^k n_i$ . The rate constants  $\alpha_i$  and  $\beta_i$  in equation (5.1) represent the interactions of the system with the particle reservoir outside the container. In effect  $\alpha_i$  and  $\beta_i$  are the rate at which molecules appear and disappear from the system, and thus are analogous to birth and death rates.

As an aside, we note that reaction rates which result from a binary encounter should be scaled by the volume of the system,  $V$ . That is,  $r_i \rightarrow r_i/V$ . This follows from a straightforward kinetic theory argument [79]. This is an innocent modification as far as this study is concerned, since it is carried out at constant volume, but it becomes crucially important when the volume is allowed to change, as it does in the analysis of the phase transition reported in [77, 78].

The state of the system is labeled by the set of integers  $\{n_1, \dots, n_k\}$  and, under the assumption that the transitions from this state to any other only depends on these integers, the system is Markov and may be described in terms of a master equation. In constructing the master equation we need to give the transition rates  $T(\mathbf{n}'|\mathbf{n})$  from the

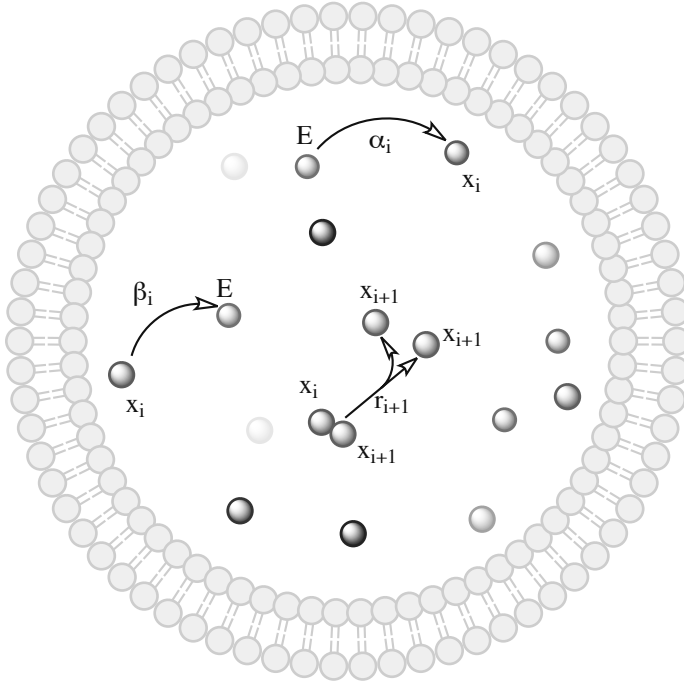


Figure 5.1: Schematic representation of reactions (5.1).

state  $\mathbf{n}$  to the state  $\mathbf{n}'$ , where  $\mathbf{n} \equiv (n_1, \dots, n_k)$ . If the system is well-stirred, so that the probability of a reaction taking place is proportional to its rate and the number of reactant molecules, then from equation (5.1) these transition rates are

$$\begin{aligned}
 T(n_1, \dots, n_i - 1, n_{i+1} + 1, \dots, n_k | \mathbf{n}) &= r_{i+1} \frac{n_i}{N} \frac{n_{i+1}}{N}, \\
 T(n_1, \dots, n_i + 1, \dots, n_k | \mathbf{n}) &= \alpha_i \left( 1 - \frac{\sum_{j=1}^k n_j}{N} \right), \\
 T(n_1, \dots, n_i - 1, \dots, n_k | \mathbf{n}) &= \beta_i \frac{n_i}{N}.
 \end{aligned} \tag{5.2}$$

The master equation for the probability that the system is in state  $\mathbf{n}$  at time  $t$ ,  $P(\mathbf{n}, t)$ , may now be written down:

$$\begin{aligned}
 \frac{dP(\mathbf{n}, t)}{dt} &= \sum_{i=1}^k (\mathcal{E}_i \mathcal{E}_{i+1}^{-1} - 1) [T(n_1, \dots, n_i - 1, n_{i+1} + 1, \dots, n_k | \mathbf{n}) P(\mathbf{n}, t)] \\
 &+ \sum_{i=1}^k (\mathcal{E}_i^{-1} - 1) [T(n_1, \dots, n_i + 1, \dots, n_k | \mathbf{n}) P(\mathbf{n}, t)] \\
 &+ \sum_{i=1}^k (\mathcal{E}_i - 1) [T(n_1, \dots, n_i - 1, \dots, n_k | \mathbf{n}) P(\mathbf{n}, t)]
 \end{aligned} \tag{5.3}$$

where  $\mathcal{E}_i^{\pm 1}$  are again the step-operators as introduced in Chapter 3. Their definition is hereafter recalled:

$$\mathcal{E}_i^{\pm 1} f(\mathbf{n}) = f(n_1, \dots, n_i \pm 1, \dots, n_k). \quad (5.4)$$

As previously remarked, equations such as (5.3) are difficult to analyze, but if one is particularly interested in large or moderately sized values of  $N$ , then the system-size expansion provides an elegant way of encapsulating the essential aspects of the model. The key assumption of the method is to write [64]

$$\frac{n_i}{N} = \phi_i(t) + \frac{\xi_i(t)}{\sqrt{N}}. \quad (5.5)$$

From this relation,  $\lim_{N \rightarrow \infty} (n_i/N) = \phi_i(t)$ , the fraction of the molecules which are of type  $X_i$  at time  $t$ , within the mean-field ( $N \rightarrow \infty$ ) limit. The fluctuations about these are assumed to be Gaussian, hence the  $1/\sqrt{N}$  in equation (5.5). This assumption applies as long as the system evolves reasonably far from the (absorbing) boundaries, so that the probability density functions of the  $X_i$  is Gaussian. In other words, stochastic extinctions cannot be captured by our perturbative calculation.

Substituting equation (5.5) into equation (5.3) allows us to expand the master equation as a power series in  $1/\sqrt{N}$ . We here recall that the step operator can be approximated as:

$$\mathcal{E}_i^{\pm 1} = 1 \pm \frac{1}{\sqrt{N}} \frac{\partial}{\partial \xi_i} + \frac{1}{2N} \frac{\partial^2}{\partial \xi_i^2} + \dots \quad (5.6)$$

If we set  $P(\mathbf{n}, t)$  equal to  $\Pi(\boldsymbol{\xi}, t)$ , the left-hand side of the master equation becomes [64]

$$\frac{dP(\mathbf{n}, t)}{dt} = \frac{\partial \Pi(\boldsymbol{\xi}, t)}{\partial t} - \sqrt{N} \sum_{i=1}^k \frac{\partial \Pi(\boldsymbol{\xi}, t)}{\partial \xi_i} \frac{d\phi_i}{dt}. \quad (5.7)$$

Applying the ansatz (5.5) to the right-hand side of equation (5.3), the step-operators (5.4) take the form (5.6), the  $n_i$  in the transition rates (5.2) are replaced by  $\phi_i$  and  $\xi_i$  using equation (5.5). This yields the following terms

(a) Terms of order  $N^{-1/2}$ :

$$\sum_{i=1}^k \left\{ r_{i+1} \phi_i \phi_{i+1} \left[ \frac{\partial}{\partial \xi_i} - \frac{\partial}{\partial \xi_{i+1}} \right] - \alpha_i \left( 1 - \sum_{j=1}^k \phi_j \right) \frac{\partial}{\partial \xi_i} + \beta_i \phi_i \frac{\partial}{\partial \xi_i} \right\} \Pi(\boldsymbol{\xi}, t) \quad (5.8)$$

(b) Terms of order  $N^{-1}$  and involving first order derivatives

$$\sum_{i=1}^k \left\{ r_{i+1} \phi_i \frac{\partial}{\partial \xi_i} \xi_{i+1} + r_{i+1} \phi_{i+1} \frac{\partial}{\partial \xi_i} \xi_i - r_{i+1} \phi_i \frac{\partial}{\partial \xi_{i+1}} \xi_{i+1} - r_{i+1} \phi_{i+1} \frac{\partial}{\partial \xi_{i+1}} \xi_i + \alpha_i \sum_{j=1}^k \frac{\partial}{\partial \xi_i} \xi_j + \beta_i \frac{\partial}{\partial \xi_i} \xi_i \right\} \Pi(\boldsymbol{\xi}, t) \quad (5.9)$$

(c) Terms of order  $N^{-1}$  and involving second order derivatives

$$\begin{aligned} & \frac{1}{2} \sum_{i=1}^k \left\{ r_{i+1} \phi_i \phi_{i+1} \left[ \frac{\partial^2}{\partial \xi_i^2} + \frac{\partial^2}{\partial \xi_{i+1}^2} - 2 \frac{\partial^2}{\partial \xi_i \partial \xi_{i+1}} \right] \right. \\ & \left. + \alpha_i \left( 1 - \sum_{j=1}^k \phi_j \right) \frac{\partial^2}{\partial \xi_i^2} + \beta_i \phi_i \frac{\partial^2}{\partial \xi_i^2} \right\} \Pi(\boldsymbol{\xi}, t). \end{aligned} \quad (5.10)$$

If we equate terms of the same order in  $1/\sqrt{N}$  on the left- and right-hand sides, the leading order gives

$$\frac{d\phi_i}{d\tau} = (r_i \phi_{i-1} - r_{i+1} \phi_{i+1}) \phi_i + \alpha_i \left( 1 - \sum_{j=1}^k \phi_j \right) - \beta_i \phi_i, \quad (5.11)$$

where  $\tau = t/N$  is a re-scaled time. This equation is a deterministic equation for the fraction of molecules which are of type  $i$ . It agrees with that of Togashi and Kaneko [77], if one takes into account that their equations are for concentrations and so contain the (constant) concentrations of the species in the reservoir. There is also an additional term  $\sum_j \phi_j$  in equation (5.11), which is typically present when mean-field equations are derived in systems with a fixed size, but not in the phenomenologically postulated form. For small concentrations it will not be important, but clearly it will have an effect as the ceiling on particle numbers is felt, reducing the number of molecules entering the container from the reservoir, as it should.

The terms of order  $N^{-1}$  in equations (5.9) and (5.10), are now identified with the remaining term on the right-hand side of equation (5.7). This resulting equation is a Fokker-Planck equation:

$$\frac{\partial \Pi}{\partial \tau} = - \sum_i \frac{\partial}{\partial \xi_i} [A_i(\boldsymbol{\xi}) \Pi] + \frac{1}{2} \sum_{i,j} B_{ij} \frac{\partial^2 \Pi}{\partial \xi_i \partial \xi_j}. \quad (5.12)$$

From equation (5.9) we see that the  $A_i(\boldsymbol{\xi})$  are linear functions of the  $\xi_j$  and from equation (5.10) that the  $B_{ij}$  are independent of them. Explicitly:

$$A_i(\boldsymbol{\xi}) = (r_i \phi_{i-1} - r_{i+1} \phi_{i+1}) \xi_i + r_i \phi_i \xi_{i-1} - r_{i+1} \phi_i \xi_{i+1} - \alpha_i \sum_{j=1}^k \xi_j - \beta_i \xi_i \quad (5.13)$$

and

$$B_{ij} = \begin{cases} -r_i \phi_{i-1} \phi_i & \text{if } j = i - 1 \\ r_{i+1} \phi_i \phi_{i+1} + r_i \phi_i \phi_{i-1} \\ \quad + \alpha_i \left( 1 - \sum_{j=1}^k \phi_j \right) + \beta_i \phi_i & \text{if } j = i \\ -r_{i+1} \phi_i \phi_{i+1} & \text{if } j = i + 1 \end{cases} \quad (5.14)$$

In equations (5.13) and (5.14),  $\phi_{k+1} \equiv \phi_1$  and  $\xi_{k+1} \equiv \xi_1$ , which follows from the cyclic nature of the model.

Since the  $A_i(\boldsymbol{\xi})$  are linear functions of the  $\xi_j$  we may write them as

$$A_i(\boldsymbol{\xi}) = \sum_{j=1}^k M_{ij} \xi_j. \quad (5.15)$$

This means that the probability distribution at next-to-leading order,  $\Pi(\boldsymbol{\xi}, \tau)$ , is completely determined by the two  $k \times k$  matrices  $M$  and  $B$ , whose elements are independent of the  $\xi_j$ , and only functions of the  $\phi_j$ . For our purposes, in complete analogy with the preceding discussion, we need to Fourier analyze the fluctuations. It is hence more convenient to characterize the fluctuation in terms of the equivalent Langevin equations:

$$\frac{d\xi_i}{d\tau} = \sum_{j=1}^k M_{ij} \xi_j(\tau) + \eta_i(\tau), \quad (5.16)$$

where  $M$  is a  $k \times k$  matrix which can be found from equations (5.13) and (5.15), and  $\eta_i$  is a Gaussian white noise with zero mean and correlator

$$\langle \eta_i(\tau) \eta_j(\tau') \rangle = B_{ij} \delta(\tau - \tau'), \quad (5.17)$$

and  $B_{ij}$  is another  $k \times k$  matrix given by equation (5.14).

Equation (5.16), is a stochastic differential equation for the deviation from the mean-field behavior. It is the analysis of this equation, together with the mean-field system (5.11), that allow us to describe the stochastic aspects of the autocatalytic reactions in a quantitative way.

### 5.1.1 On the fluctuations

In their numerical studies, Togashi and Kaneko [77, 78] looked at the simplest case of the model where the rates  $r_i$ ,  $\alpha_i$  and  $\beta_i$  were the same for all chemical species. To illustrate our method we will do the same, and so from now on we will drop the subscript  $i$  on these constants, but it should be clear that our analysis also applies to the general situation where they are different for each species. With this choice, the deterministic equations (5.11) have a single fixed point:

$$\phi^* = \frac{\alpha}{\beta + k\alpha}, \quad (5.18)$$

where the asterisk denotes the fixed point value.

In principle the matrices  $M$  and  $B$  are time dependent, since  $\phi_j$  is. However, in practice we are just interested in the fluctuations about the stationary state, once the initial transient has died out. This is equivalent to replacing  $\phi_j$  with its corresponding equilibrium solution. In our case the asymptotic value of  $\phi_j$  is specified by equation (5.18). Hence,  $M$  and  $B$  are given by

$$M = \begin{bmatrix} m_0 & m_1 & m_2 & m_2 \dots & m_2 & m_3 \\ m_3 & m_0 & m_1 & m_2 \dots & m_2 & m_2 \\ m_2 & m_3 & m_0 & m_1 \dots & m_2 & m_2 \\ m_2 & m_2 & m_3 & m_0 \dots & m_2 & m_2 \\ \dots & \dots & \dots & \dots & \dots & \dots \\ m_2 & m_2 & m_2 & m_2 \dots & m_0 & m_1 \\ m_1 & m_2 & m_2 & m_2 \dots & m_3 & m_0 \end{bmatrix}, \quad (5.19)$$

where

$$\begin{aligned}
 m_0 &= -\alpha - \beta \\
 m_1 &= -\alpha - r\phi^* \\
 m_2 &= -\alpha \\
 m_3 &= -\alpha + r\phi^*
 \end{aligned} \tag{5.20}$$

and

$$B = \begin{bmatrix} b_0 & b_1 & 0 \dots & 0 & b_1 \\ b_1 & b_0 & b_1 \dots & 0 & 0 \\ 0 & b_1 & b_0 \dots & 0 & 0 \\ \dots & \dots & \dots & \dots & \dots \\ 0 & 0 & 0 \dots & b_0 & b_1 \\ b_1 & 0 & 0 \dots & b_1 & b_0 \end{bmatrix}, \tag{5.21}$$

where

$$\begin{aligned}
 b_0 &= 2r(\phi^*)^2 + \beta\phi^* + \alpha(1 - k\phi^*) \\
 b_1 &= -r(\phi^*)^2.
 \end{aligned} \tag{5.22}$$

If  $N$  is so large that the fluctuations are completely negligible, then the system tends towards a state where the fractions of the chemical species in the system are equal, and given by equation (5.18), and stays there. Of course, if  $N$  is finite this is no longer the case and there are fluctuations about this stationary state, and as we will see these can be significant even if  $N$  is quite large. Since these fluctuations are expected to be oscillatory, we begin their analysis by taking the Fourier transform of equation (5.16) to find

$$\sum_{j=1}^k (-i\omega\delta_{ij} - M_{ij}) \tilde{\xi}_j(\omega) = \tilde{\eta}_i(\omega), \tag{5.23}$$

where the  $\tilde{f}$  denotes the Fourier transform of the function  $f$ . Defining the matrix  $-i\omega\delta_{ij} - M_{ij}$  to be  $\Phi_{ij}(\omega)$ , the solution to equation (5.23) is

$$\tilde{\xi}_i(\omega) = \sum_{j=1}^k \Phi_{ij}^{-1}(\omega) \tilde{\eta}_j(\omega). \tag{5.24}$$

To identify the dominant frequency of the oscillatory behavior, we compute the power spectrum for the  $i$ -th species,  $P_i(\omega)$ , from equation (5.24):

$$P_i(\omega) \equiv \left\langle |\tilde{\xi}(\omega)|^2 \right\rangle = \sum_{j=1}^k \sum_{l=1}^k \Phi_{ij}^{-1}(\omega) B_{jl} (\Phi^\dagger)^{-1}_{li}(\omega), \tag{5.25}$$

Since  $\Phi = -i\omega I - M$ , where  $I$  is the  $k \times k$  unit matrix, and since  $M$  and  $B$  are independent of  $\omega$ , the structure of  $P_i(\omega)$  is that of a polynomial of order  $2k$  divided by another polynomial of degree  $2k$ . The explicit form of the denominator is  $|\det \Phi(\omega)|^2$ .

From previous investigations of fluctuations of a similar kind [6, 8, 7], we expect that the fluctuations about the stationary state (5.18) will be enhanced by a resonant effect: For values of  $\omega$  for which  $|\det \Phi(\omega)|$  is a minimum, the power spectra will show peaks

which correspond to larger than expected fluctuations at that frequency. This effect was first conjectured by Bartlett [80] in the context of the modeling of measles epidemics, and later elaborated upon by Nisbet and Gurney [81], who called these stochastically induced cycles, quasi-cycles. However, as already emphasized, it is only in the last few years that explicit calculations within the system-size expansion have been carried out and a quantitative understanding of the phenomenon has emerged [6].

To understand the analytic structure of the power spectra, we begin by supposing that we can neglect the effects of the numerator on the right-hand side of equation (5.25), and simply determine the dominant frequency by looking for the value which minimizes  $|\det\Phi(\omega)|$ . The effect of the numerator will be to shift this frequency; we are assuming as a first approximation that this shift will be small, as indeed it has been found to be in some cases [6]. If  $\lambda_j$  are the eigenvalues of  $M$ , then the denominator of the expression for the power spectra may be written as

$$|\det\Phi(\omega)|^2 = \prod_{j=1}^k (-i\omega - \lambda_j)(i\omega - \lambda_j^*). \quad (5.26)$$

Since  $M$  is real, the  $\lambda_j$  will be real or come in complex conjugate pairs, so that the products in equation (5.26) has one of two forms:

- (i) If  $\lambda$  is real, the two factors involving this eigenvalue give  $(\omega^2 + \lambda^2)$ .
- (ii) If  $\lambda$  is complex:  $\lambda = \lambda_R + i\lambda_I$ , the four terms involving  $\lambda$  and  $\lambda^*$  give

$$|\omega^2 + (\lambda_R^2 - \lambda_I^2) + 2i\lambda_R\lambda_I|^2. \quad (5.27)$$

The resonant effect has its origin in the structure of the factor coming from the complex eigenvalues shown in the expression (5.27). It is smallest, and so gives the largest contribution when it is in the denominator, for frequencies which satisfy

$$\omega_c^2 = \lambda_I^2 - \lambda_R^2. \quad (5.28)$$

If there are several pairs of complex eigenvalues and their conjugates, the largest contribution should come from the pair for which  $\lambda_R\lambda_I$  is smallest. Clearly this will only be approximately true since, not only are we neglecting the numerator, but also the factors  $(\omega^2 + \lambda^2)$  coming from real eigenvalues, as well as those coming from other complex conjugate pairs. However, as we will now see by looking at two specific cases,  $k = 4$  and  $k = 8$ , these approximations appear to be remarkably good.

We study the cases  $k = 4$  and  $k = 8$  because they are the smallest even values of  $k$  for which one complex conjugate pair and two distinct complex conjugate pairs, respectively, exist (there are two complex conjugate pairs for  $k = 6$ , but they are equal, and three for  $k = 8$ , but two of these are equal). We therefore expect to see one peak in the power spectra when  $k = 4$  and two when  $k = 8$ . Our analysis, and the accuracy of our approximations, can be directly checked by numerical simulation of the chemical reaction system (5.1) by use of the Gillespie algorithm [79, 82]. This produces realizations of the stochastic dynamics which are equivalent to those found from the master equation (5.3). Averaging over many of these realizations gives us power spectra after Fourier transformation, which are exact to a given numerical accuracy. We now investigate the two cases  $k = 4$  and  $k = 8$  in more detail.

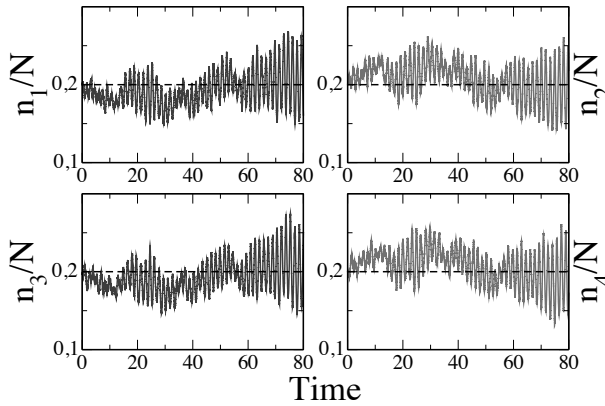


Figure 5.2: Time evolution of selected species,  $i = 1, 2, 3, 4$  in clockwise order for the case  $k = 4$ . Here  $r = 10$ ,  $\alpha = \beta = 1/64$ ,  $N = 8192$ . The dashed line indicates the mean field solution. The species display a clear oscillatory trend about their mean field values. A paired synchronization, (1, 3) vs. (2, 4) rich states, is also visible, as already observed in [77, 78].

### Power spectra when $k = 4$

The time evolution of the species is depicted in Fig. 5.2. This clearly displays large oscillations which we aim to investigate analytically. Before beginning this analysis, we observe that species 1, 3 (odd) and 2, 4 (even) are paired together and move up and down from the reference mean-field level in a synchronized fashion. This fact was already recognized in [77, 78] and shown to drive successive switches between the 1–3 or 2–4 rich states, close to the absorbing boundary, i.e. when a small number of molecules is simulated. The rate at which the changes occur is controlled by the diffusion parameter. However, the details of the transitions stem from a purely dynamical effect which cannot be captured within the perturbative analysis developed here.

Let us now turn to analytically characterizing the aforementioned oscillatory regime. To this end we begin by determining the eigenvalues of the  $M$  matrix.

We note that  $M$  is a circulant matrix [83], and therefore its eigenvalues are given by

$$\lambda_\ell = \sum_{j=1}^k m_{1j} e^{(2\pi i(j-1)\ell)/k}, \quad \ell = 0, 1, \dots, k-1, \quad (5.29)$$

where  $m_{1j}$  is the element of  $M$  in the first row and  $j$ -th column. In fact,  $M$  is not the most general form of circulant matrix;  $(k-3)$  entries in each row are equal (to  $m_2$ ).

This leads to a simplified form for the eigenvalues:

$$\begin{aligned}\lambda_\ell &= m_0 + m_1 e^{2\pi i \ell / k} + m_3 e^{-2\pi i \ell / k} + m_2 \sum_{j=2}^{k-2} e^{2\pi i j \ell / k} \\ &= m_0 + m_1 e^{2\pi i \ell / k} + m_3 e^{-2\pi i \ell / k} - m_2 \frac{\sin(3\pi \ell / k)}{\sin(\pi \ell / k)},\end{aligned}\tag{5.30}$$

where in the last line  $\ell \neq 0$ . Putting in the values from equation (5.20) gives

$$\lambda_\ell = \begin{cases} -\beta - k\alpha, & \text{if } \ell = 0 \\ -\beta - 2ir\phi^* \sin(2\pi \ell / k), & \text{if } \ell \neq 0. \end{cases}\tag{5.31}$$

For  $k = 4$ , the eigenvalues are

$$\begin{aligned}\lambda_0 &= -\beta - 4\alpha \\ \lambda_1 &= -\beta - 2ir\phi^* \\ \lambda_2 &= -\beta \\ \lambda_3 &= \lambda_1^*.\end{aligned}\tag{5.32}$$

Within the approximations we have discussed, we would expect that there should be a single peak in the power spectrum for any one of the chemical species at a frequency given by (see equation (5.28))

$$\omega_c^2 = 4r^2 (\phi^*)^2 - \beta^2 = \frac{4r^2 \alpha^2}{(\beta + 4\alpha)^2} - \beta^2.\tag{5.33}$$

In Fig. 5.3 we show the power spectrum (for the chemical species  $i = 2$ ) found by averaging over 500 realizations from the Gillespie algorithm, together with that found from equation (5.25). The good agreement between the simulation results and those found from applying the system-size expansion, shows that the method works well for  $N = 5000$ . The parameters used in this case were  $r = 10$  and  $\alpha = \beta = 1/64$ , which gives a value of  $\omega_c \approx 4$  from equation (5.33). From Fig. 5.3 we see this is a surprising good estimate for the position of the peak, given the significant frequency dependence which we have neglected to obtain the estimate (5.28).

Another check of the accuracy of these approximations, and so of equation (5.28), is to imagine increasing the parameter  $\beta$  at fixed  $r$  and  $\alpha$ , and asking when  $\omega_c^2$  will become zero, and so at what frequency will the peak in the power spectra disappear. From equation (5.33) we estimate this to be

$$\beta \sim \frac{2r\alpha}{\beta} \text{ or } \beta \sim \sqrt{2r\alpha},\tag{5.34}$$

which equals 0.56 for the values of  $r$  and  $\alpha$  used in Fig. 5.3. Once again this agrees well with the full spectrum which predicts the peak to disappear at about the same value. As a final check, we measure the position of the peak from a set of simulations run at different values of  $r$ . Direct measurements (symbols) are compared to the theory (solid line) in Fig. 5.4 and are in good quantitative agreement. Again, we recall that adjusting the rate  $r$  can be equivalently seen as modifying the volume of the system, which is the setting investigated in [77, 78].

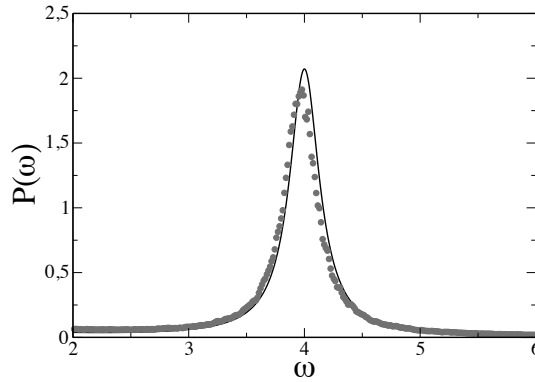


Figure 5.3: Power spectrum of species  $i = 2$  when  $k = 4$ . The analytical curve is shown as a solid line and the simulation (average over 500 independent realizations) as symbols. Here  $r = 10$ ,  $\alpha = \beta = 10/64$ ,  $N = 5000$ .

### Power spectra when $k = 8$

From equation (5.31), the eigenvalues of the  $M$  matrix are

$$\begin{aligned}
 \lambda_0 &= -\beta - 8\alpha, \lambda_4 = -\beta, \\
 \lambda_1 &= -\beta - \sqrt{2}ir\phi^*, \lambda_7 = \lambda_1^*, \\
 \lambda_2 &= -\beta - 2ir\phi^*, \lambda_6 = \lambda_2^*, \\
 \lambda_3 &= -\beta - \sqrt{2}ir\phi^*, \lambda_5 = \lambda_3^*.
 \end{aligned} \tag{5.35}$$

Since there are two distinct complex conjugate pairs we would expect to find two peaks in the power spectra, one at  $\omega_c^2 = 2r^2(\phi^*)^2 - \beta^2$  and the other at  $\omega_c^2 = 4r^2(\phi^*)^2 - \beta^2$ . For small  $\beta$ , one peak will be at a frequency  $\sqrt{2}$  times the other. We would also expect that the peak at lower frequency would be larger than the one at higher frequency, since  $\lambda_R \lambda_I$  is smaller for the former. That is, the pole in the power spectra in the complex frequency squared plane is nearer to the real axis for the peak at lower frequency, and so should have a bigger effect. So, in summary, our approximations indicate that the peaks in the power spectra should be given by

$$\begin{aligned}
 \omega_{c1}^2 &= \frac{2r^2\alpha^2}{(\beta + 8\alpha)^2} - \beta^2 \\
 \omega_{c2}^2 &= \frac{4r^2\alpha^2}{(\beta + 8\alpha)^2} - \beta^2,
 \end{aligned} \tag{5.36}$$

with the peak at  $\omega = \omega_{c1}$  larger than the one at  $\omega = \omega_{c2}$ . The results of plotting the full spectrum found from equation (5.25) and simulation results are shown in Fig. 5.5 for  $r = 200$ ,  $\alpha = 1.9$  and  $\beta = 2$ . This corresponds to peaks at  $\omega = 31.2$  and  $\omega = 44.14$ , according to equations (5.36), which once again agrees very well with the results displayed in the figure, as does the prediction that the peak nearest the origin should be the largest.

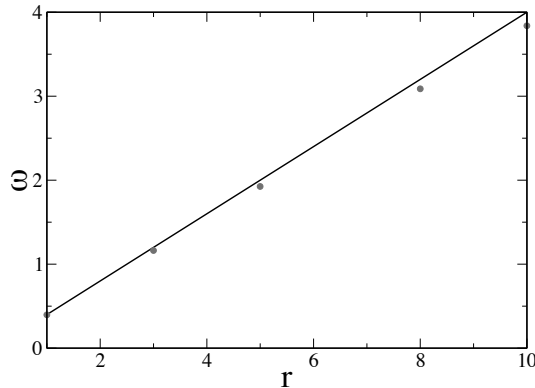


Figure 5.4: The position of the peak in the power spectrum (for species  $i = 2$  when  $k = 4$ ) plotted as function of the rate constant  $r$ . Symbols refers to the stochastic simulations, while the solid line shows the analytical prediction. Here  $\alpha = \beta = 1/64$ ,  $N = 5000$

To the best of our knowledge, this is the first time that a double-peaked power spectrum has been predicted to emerge as a resonant effect, within a van Kampen type of analysis.

## 5.2 On a spatial model of autocatalytic reactions

We here present a spatial version of the autocatalytic model discussed in the previous section. This work is developed in collaboration with Pietro de Anna and constitute the core of his master thesis essay [84] (see also [85]). Our analysis is closely inspired to that of Lugo and McKane [86]

The idea is to introduce a spatial coarse graining at the level of small micro-cells (which total to  $\Omega$ ) which are supposed to uniformly cover the volume occupied by the vesicle. In each microscopic cell autocatalytic reactions as specified by (5.1) (and recalled below) do occur. Migration between neighbours cells is allowed, an ingredient which in turn amounts to explicitly account for space. As a simplifying ansatz, we image a periodic geometry and focus on a chain of microscopic cells situated at the frontier with the external membrane. In the case of a 1D setting micro-cell 1 is adjacent to micro-cell  $\Omega$ . This simplifying hypothesis is put forward so to restore the translational invariance, which shall be invoked in the Fourier based treatment developed in the end. Physically one might imagine to simulate the transport of material along a tiny shell which is positioned close to the outer edge of the vesicle (a sort of spatio-temporal zonal flow). The shell is then assumed to communicate with the outside and the inside via an effective diffusion mechanism which, however, does not embed space explicitly.

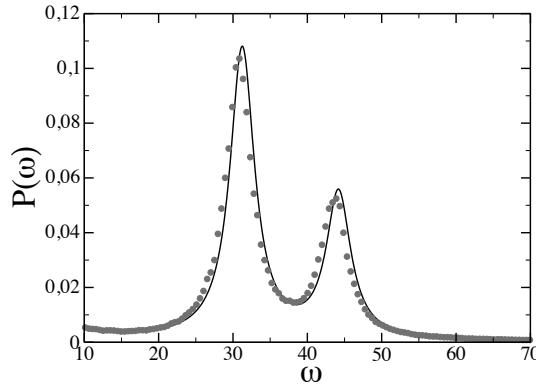
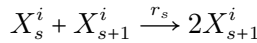


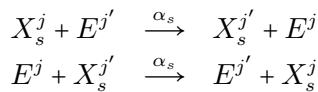
Figure 5.5: Power spectrum of the time series for species  $i = 2$  when  $k = 8$ . The analytical result (solid line) is superimposed onto the simulations (symbols), averaged over 500 independent realizations. Here  $r = 200$ ,  $\alpha = 1.9$ ,  $\beta = 2$ ,  $N = 7000$ .

### 5.2.1 The perturbative expansion

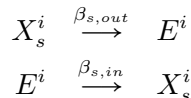
We start by consider, in complete analogy with the aforementioned Togashi and Kanenko model,  $k$  chemical species. The autocatalytic reactions for the  $X_s^i$  species are:



where  $X_{k+1}^i = X_1^i$ . The index  $i$  labels the cell where the reaction is supposed to occur, while  $s$  stands for the species type. Clearly,  $i = 1, \dots, \Omega$  and  $s = 1, \dots, k$ . As anticipated, we shall be concerned with migration between adjacent cells a process which is encapsulated in the following relations:



where  $j$  and  $j'$  represent nearby sites and  $E$  stands for the empty case. Finally, we shall be accommodating for the diffusion (in/out) through the region delimited by the shell. Such a diffusion occur either towards the inside of the cell or the outside. These effects are specified by:



The allowed reactions are also depicted in Fig. 5.6 Introducing  $n_s^i$  to label the population amount of species  $s$  living in cell  $i$ , one can characterize the status of the system as a vector  $\mathbf{n} = (\mathbf{n}^1, \mathbf{n}^2, \dots, \mathbf{n}^\Omega)$  where  $\mathbf{n}^i = (n_1^i, n_2^i, \dots, n_s^i)$ . With analogy of the previous section, we simplify the model assuming that all the rates  $r_s$ ,  $\alpha_s$ ,  $\beta_{s,in}$  and  $\beta_{s,out}$  are the

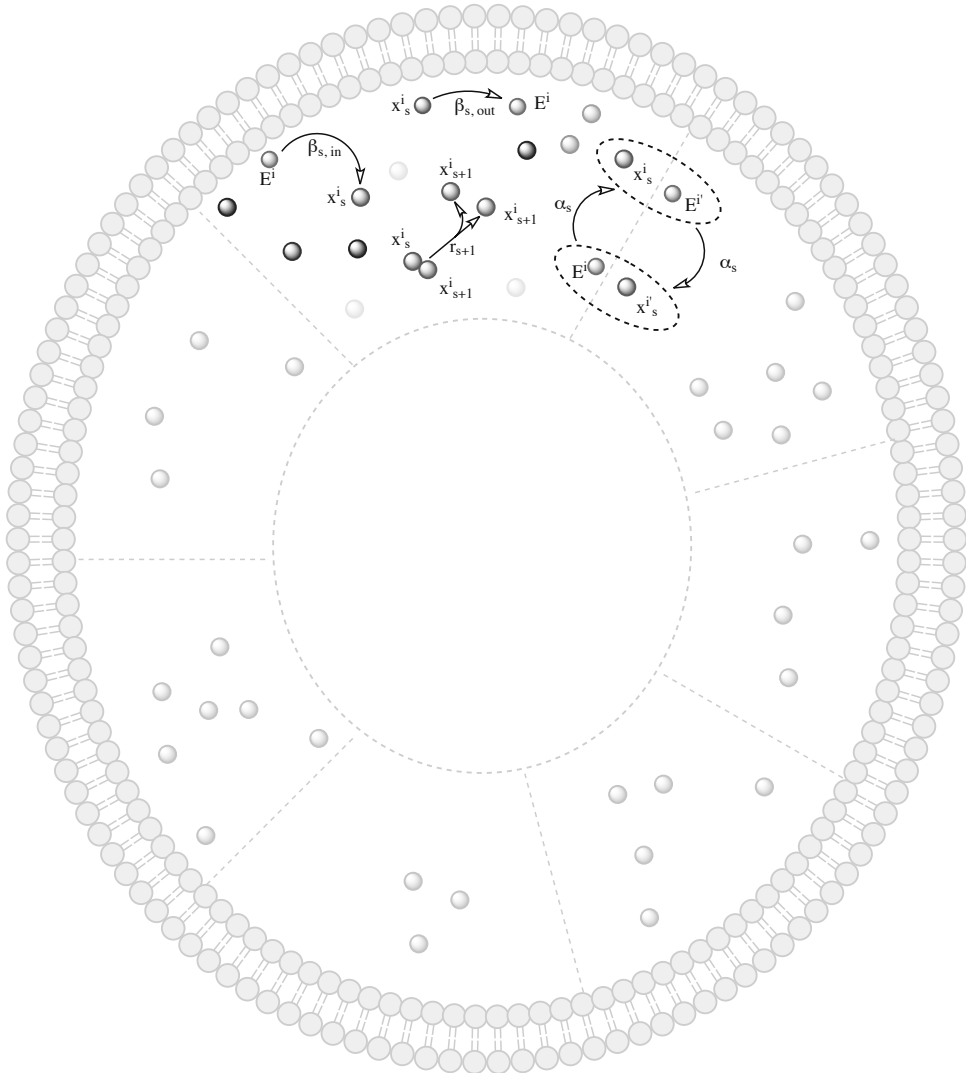


Figure 5.6: We consider a tiny, inner, shell adjacent to the external membrane. Such a shell is partitioned in  $\Omega$  micro-cells (dashed yellow sectors). In every cell, autocatalytic reactions do occur of the Togashi and Kaneko type. As an additional ingredient, migration between nearby cells is here allowed. An effective diffusion mechanism is also invoked to regulate the mass exchange between every micro-cell and the interior bulk (resp. outside environment).

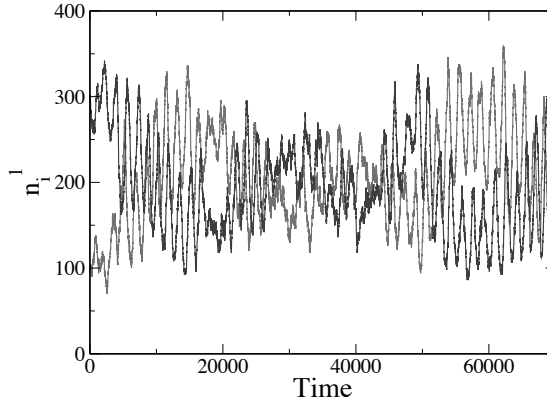


Figure 5.7: Time evolution of species 1 (red line) and species 2 (blue line) in cell number 1. Parameters used for the stochastic simulation are  $\alpha = 0.1$ ,  $r = 10$ ,  $\beta_{in} = 10/64$ ,  $\beta_{out} = 10/64$ ,  $\Omega = 16$ ,  $k = 4$ ,  $N = 1000$ .

same for all the chemical species, and we will drop the subscript  $s$  on the constants. The rates of transition from one state to the other as controlled by the above chemical equations, are listed below (adopting the standard convention).

Transitions stemming from the autocatalytic cycles:

$$T(n_s^i - 1, n_{s+1}^i + 1 | n_s^i, n_{s+1}^i) = \frac{r}{\Omega} \frac{n_s^i}{N} \frac{n_{s+1}^i}{N}$$

For the outward/inward incoming/escape:

$$T(n_s^i - 1 | n_s^i) = \frac{\beta_{out}}{\Omega} \frac{n_s^i}{N}$$

$$T(n_s^i + 1 | n_s^i) = \frac{\beta_{in}}{\Omega} \left( 1 - \sum_s^k \frac{n_s^i}{N} \right)$$

where use has been made of the equation of conservation of mass (all species amount, including the empties, should sum up to  $N$ ). Finally, the transition rates associated to the cell-to-cell migration are:

$$T(n_s^j - 1, n_s^{j'} + 1 | n_s^j, n_s^{j'}) = \frac{\alpha}{z\Omega} \frac{n_s^j}{N} \left( 1 - \sum_{m=1}^k \frac{n_m^{j'}}{N} \right)$$

$$T(n_s^j + 1, n_s^{j'} - 1 | n_s^j, n_s^{j'}) = \frac{\alpha}{z\Omega} \frac{n_s^{j'}}{N} \left( 1 - \sum_{m=1}^k \frac{n_m^j}{N} \right)$$

where  $z$  stands for the number of nearest neighbours.

Also in this case, we can use the transition probabilities to simulate the model with the Gillespie algorithm. Fig. 5.7 shows a typical result of the stochastic simulation relative to cell number 1 for a system populated by four species. Red line represents the

time evolution of specie 1, while the blue line refers to the second specie. With analogy with the non-spatial model, we observe that even-index species are asynchronized with those with odd-index.

The evolution of the system is governed by the master equation which can be cast in the form:

$$\frac{d}{dt}P(\mathbf{n}, t) = A + B + C$$

where the  $A$ ,  $B$  and  $C$  refer to the processes isolated above and explicitly read:

$$A = \sum_{j=1}^{\Omega} \sum_{s=1}^k \left[ T(n_s^j, n_{s+1}^j | n_s^j + 1, n_{s+1}^j - 1) P(n_s^j + 1, n_{s+1}^j - 1, t) - T(n_s^j - 1, n_{s+1}^j + 1 | n_s^j, n_{s+1}^j) P(n_s^j, n_{s+1}^j, t) \right] \quad (5.37)$$

$$B = \sum_{j=1}^{\Omega} \sum_{s=1}^k \sum_{j' \in j} \left[ T(n_s^j, n_s^{j'} | n_s^j + 1, n_s^{j'} - 1) P(n_s^j + 1, n_s^{j'} - 1, t) - T(n_s^j - 1, n_s^{j'} + 1 | n_s^j, n_s^{j'}) P(n_s^j, n_s^{j'}, t) + T(n_s^j, n_s^{j'} | n_s^j - 1, n_s^{j'} + 1) P(n_s^j - 1, n_s^{j'} + 1, t) - T(n_s^j + 1, n_s^{j'} - 1 | n_s^j, n_s^{j'}) P(n_s^j, n_s^{j'}, t) \right] \quad (5.38)$$

$$C = \sum_{j=1}^{\Omega} \sum_{s=1}^k \left[ T(n_s^j | n_s^j + 1) P(n_s^j + 1, t) - T(n_s^j - 1 | n_s^j) P(n_s^j, t) + T(n_s^j | n_s^j - 1) P(n_s^j - 1, t) - T(n_s^j + 1 | n_s^j) P(n_s^j, t) \right] \quad (5.39)$$

Introducing the shift operators as

$$\varepsilon_{s,j}^{\pm} f(\dots, n_s^j, \dots) = f(\dots, n_s^j \pm 1, \dots) \quad (5.40)$$

the master equation takes the form

$$\begin{aligned} \frac{d}{dt}P(\mathbf{n}, t) &= \sum_{j=1}^{\Omega} \sum_{s=1}^k \left[ (\varepsilon_{s,j}^+ \varepsilon_{s+1,j}^- - 1) T(n_s^j - 1, n_{s+1}^j + 1 | n_s^j, n_{s+1}^j) \right. \\ &\quad \times P(n_s, n_{s+1}, t) \\ &\quad + \sum_{j=1}^{\Omega} \sum_{s=1}^k \sum_{j' \in j} \left[ (\varepsilon_{s,j}^+ \varepsilon_{s,j'}^- - 1) T(n_s^j - 1, n_s^{j'} + 1 | n_s^j, n_s^{j'}) \right. \\ &\quad \times P(n_s^j, n_s^{j'}, t) + \\ &\quad \left. + (\varepsilon_{s,j}^- \varepsilon_{s,j'}^+ - 1) T(n_s^j + 1, n_s^{j'} - 1 | n_s^j, n_s^{j'}) P(n_s^j, n_s^{j'}, t) \right] \\ &\quad + \sum_{j=1}^{\Omega} \sum_{s=1}^k \left[ (\varepsilon_{s,j}^+ - 1) T(n_s^j - 1 | n_s^j) P(n_s^j, t) \right. \\ &\quad \left. + (\varepsilon_{s,j}^- - 1) T(n_s^j + 1 | n_s^j) P(n_s^j, t) \right] \end{aligned} \quad (5.41)$$

We now proceed according to the van Kampen prescriptions, splitting every discrete variable  $n_s^j$  into two components

$$n_s^j = N\phi_s^j + N^{\frac{1}{2}}\xi_s^j$$

where  $\phi_s^j$  is the deterministic part defined as  $\langle \phi_s^j \rangle / N$ , while  $\xi_s^j$  is the stochastic contribution. Within this change of variables, the step operators (5.40) have a simple form for large  $N$ , namely

$$\begin{aligned} \varepsilon_{s,j}^{\pm} &= 1 \pm N^{-\frac{1}{2}} \frac{\partial}{\partial \xi_s^j} + N^{-1} \frac{\partial^2}{\partial (\xi_s^j)^2} + \dots \\ &\equiv 1 \pm N^{-\frac{1}{2}} \partial_{\xi_s^j} + N^{-1} \partial_{\xi_s^j}^2 + \dots \end{aligned}$$

In this way, defining the new probability distribution  $\Pi(\xi_s^j, t) \equiv P(n_s^j, t)$ , the left hand side of the master equation (5.41) may be written as

$$\frac{d}{dt} P(\mathbf{n}, t) = \frac{\partial}{\partial t} \Pi(\xi_s^j, t) - N^{\frac{1}{2}} \sum_j \sum_s^k \frac{\partial}{\partial \xi_s^j} \Pi(\xi_s^j, t) \frac{d}{dt} \phi_s^j$$

The right hand side of the master equation can be also expressed as function of the expanded operators and of the stochastic variables,  $\Pi$ ,  $\phi_s^j$  and  $\xi_s^j$ . We start by noticing that

$$\begin{aligned} (\varepsilon_{s,j}^+ \varepsilon_{s+1,j}^- - 1) &\simeq N^{-\frac{1}{2}} (\partial_{\xi_s^j} - \partial_{\xi_{s+1}^j}) + \frac{1}{2} \left[ N^{-\frac{1}{2}} (\partial_{\xi_s^j} - \partial_{\xi_{s+1}^j}) \right]^2 \\ &= N^{-\frac{1}{2}} \widehat{L}_{1s} + \frac{1}{2} N^{-1} \widehat{L}_{2s} \\ (\varepsilon_{s,j}^+ \varepsilon_{s,j'}^- - 1) &\simeq N^{-\frac{1}{2}} (\partial_{\xi_s^j} - \partial_{\xi_s^{j'}}) + \frac{1}{2} \left[ N^{-\frac{1}{2}} (\partial_{\xi_s^j} - \partial_{\xi_s^{j'}}) \right]^2 \\ &= N^{-\frac{1}{2}} \widehat{L}_{1j} + \frac{1}{2} N^{-1} \widehat{L}_{2j} \\ (\varepsilon_{s,j}^- \varepsilon_{s,j'}^+ - 1) &\simeq N^{-\frac{1}{2}} (\partial_{\xi_s^{j'}} - \partial_{\xi_s^j}) + \frac{1}{2} \left[ N^{-\frac{1}{2}} (\partial_{\xi_s^{j'}} - \partial_{\xi_s^j}) \right]^2 \\ &= -N^{-\frac{1}{2}} \widehat{L}_{1j} + \frac{1}{2} N^{-1} \widehat{L}_{2j} \end{aligned}$$

where the operators  $\widehat{L}_{1s}$  and  $\widehat{L}_{2s}$  respectively read

$$\begin{aligned} \widehat{L}_{1s} &= (\partial_{\xi_s^j} - \partial_{\xi_{s+1}^j}) \\ \widehat{L}_{2s} &= (\partial_{\xi_s^j} - \partial_{\xi_{s+1}^j})^2 \end{aligned}$$

and

$$\begin{aligned} \widehat{L}_{1j} &= (\partial_{\xi_s^j} - \partial_{\xi_s^{j'}}) \\ \widehat{L}_{2j} &= (\partial_{\xi_s^j} - \partial_{\xi_s^{j'}})^2 \end{aligned}$$

In addition

$$\begin{aligned}(\varepsilon_{s,j}^- - 1) &\simeq -N^{-\frac{1}{2}} \partial_{\xi_s^j} + \frac{1}{2} N^{-1} \partial_{\xi_s^j}^2 \\(\varepsilon_{s,j}^+ - 1) &\simeq N^{-\frac{1}{2}} \partial_{\xi_s^j} + \frac{1}{2} N^{-1} \partial_{\xi_s^j}^2\end{aligned}$$

For each of the three terms (5.37)–(5.39), namely  $A, B, C$ , we can identify the associated  $N^{-1/2}$  and  $N^{-1}$  contributions.

### 5.2.2 Right hand side of the master equation: $N^{-1/2}$ terms

The leading term relative to  $A$  mentioned above reads:

$$A_{N^{-1/2}} = \frac{r}{\Omega} \sum_j \sum_s \widehat{L}_{1s}(\phi_s^j \phi_{s+1}^j) \Pi$$

Recalling the definition of  $\widehat{L}_{1s}$  one obtains

$$A_{N^{-1/2}} = \sum_j \sum_s \frac{r}{\Omega} (\phi_s^j \phi_{s+1}^j \partial_{\xi_s^j} - \phi_s^j \phi_{s+1}^j \partial_{\xi_{s+1}^j}) \Pi$$

but

$$\sum_j \sum_{s=1}^k \phi_s^j \phi_{s+1}^j \partial_{\xi_{s+1}^j} \Pi \rightarrow \sum_j \sum_{s=2}^{k+1} \phi_{s-1}^j \phi_s^j \partial_{\xi_s^j} \Pi$$

and since  $k+1 \rightarrow 1$  one finally gets

$$A_{N^{-1/2}} = \sum_j \sum_s \frac{r}{\Omega} (\phi_s^j \phi_{s+1}^j - \phi_{s-1}^j \phi_s^j) \partial_{\xi_s^j} \Pi$$

We now turn to considering the contribution of term  $B$ .

$$B_{N^{-1/2}} = \frac{\alpha}{z\Omega} \sum_j \sum_s \sum_{j' \in j} \widehat{L}_{1j} \left( \phi_s^j (1 - \sum_m \phi_m^{j'}) + \phi_s^{j'} (1 - \sum_m \phi_m^j) \right) \Pi \quad (5.42)$$

which, recalling the definition of  $\widehat{L}_{1j}$ , implies

$$B_{N^{-1/2}} = 2 \frac{\alpha}{z\Omega} \sum_j \sum_s \sum_{j' \in j} \partial_{\xi_s^j} \left( \phi_s^j (1 - \sum_m \phi_m^{j'}) - \phi_s^{j'} (1 - \sum_m \phi_m^j) \right) \Pi \quad (5.43)$$

where the factor 2 comes from exchanging  $j' \rightarrow j$  in the term associated in (5.42) to  $\partial_{\xi_s^{j'}}$ . We then proceed by adding on the right hand side two terms which sum to zero, namely

$$0 = \phi_s^j \sum_m \phi_m^j - \phi_s^j \sum_m \phi_m^j$$

a formal step which allows us to rewrite equation (5.43) in terms of differences between homologous quantities evaluated at the adjacent site

$$B_{N-1/2} = 2 \frac{\alpha}{z\Omega} \sum_j \sum_s \sum_{j' \in j} \partial_{\xi_s^j} \left[ (\phi_s^j - \phi_s^{j'}) + (\phi_s^{j'} - \phi_s^j) \sum_m \phi_m^j + \phi_s^j \sum_m (\phi_m^j - \phi_m^{j'}) \right] \Pi$$

Introducing the discrete Laplacian

$$\Delta f_j = \frac{2}{z} \sum_{j' \in j} (f_{j'} - f_j), \quad (5.44)$$

eventually yields

$$B_{N-1/2} = -\frac{\alpha}{\Omega} \sum_j \sum_s \left[ \Delta \phi_s^j (1 - \sum_m \phi_m^j) + \phi_s^j \sum_m \Delta \phi_m^j \right] \partial_{\xi_s^j} \Pi$$

Let us now consider the contribution relative to  $C$  for which one immediately gets

$$C_{N-1/2} = \sum_j \sum_s \left[ \frac{\beta_{out}}{\Omega} \phi_s^j - \frac{\beta_{in}}{\Omega} (1 - \sum_m \phi_m^j) \right] \partial_{\xi_s^j} \Pi$$

Retaining order  $N^{-1/2}$  terms in the development of master equation we obtain the mean-field equation for species  $s$  in cell  $j$

$$\begin{aligned} \frac{d}{d\tau} \phi_s^j &= \frac{r}{\Omega} (\phi_{s-1}^j \phi_s^j - \phi_s^j \phi_{s+1}^j) + \frac{\alpha}{\Omega} \left( \Delta \phi_s^j (1 - \sum_m \phi_m^j) + \phi_s^j \sum_m \Delta \phi_m^j \right) \\ &\quad + \frac{\beta_i}{\Omega} (1 - \sum_m \phi_m^j) - \frac{\beta_o}{\Omega} \phi_s^j \end{aligned} \quad (5.45)$$

Here time is re-scaled as  $\tau = \frac{t}{N}$ . Notice that by setting  $\alpha$  to zero we immediately recover the mean-field equations (5.11) for the non-spatial model.

To find the homogeneous equilibrium solution, we have to impose that no gradient in the concentration is allowed between nearby micro-cells. Hence the Laplacian contribution in equation (5.45) can be set to zero. The equilibrium point of the dynamics is therefore

$$\phi^* = \frac{\beta_{in}}{k\beta_{in} + \beta_{out}}$$

for any  $s = 1, \dots, k$  and  $j = 1, \dots, \Omega$ .

### 5.2.3 Right hand side of the master equation: $N^{-1}$ terms

It should be remarked that for any of the three contributions entering the master equation, namely  $A$ ,  $B$  and  $C$ , two types of terms are to be considered

- The terms where first derivatives enter. These are expressed as a function of the operator  $\widehat{L}_{1j}$ , so function of the first derivatives in the fluctuation variables. These contributions are here called  $A_{N-1}^1$ ,  $B_{N-1}^1$  and  $C_{N-1}^1$
- The terms where second derivatives enter. These are expressed as a function of the operator  $\widehat{L}_{2j}$ , so function of the second derivatives in the fluctuation variables. These contribution are termed  $A_{N-1}^2$ ,  $B_{N-1}^2$  and  $C_{N-1}^2$

Let us start by evaluating the above contributions.

### Evaluating $A_{N-1}^1$ , $B_{N-1}^1$ and $C_{N-1}^1$

Consider the autocatalytic reaction. We have

$$A_{N-1}^1 = \sum_j \sum_s \frac{r}{\Omega} \left[ \widehat{L}_{1s} \left( \phi_s^j \xi_{s+1}^j + \phi_{s+1}^j \xi_s^j \right) \right] \Pi$$

and, recalling the definition of  $\widehat{L}_{1s}$ , we obtain

$$A_{N-1}^1 = \sum_j \sum_s \frac{r}{\Omega} \left[ \partial_{\xi_s^j} \left( \phi_s^j \xi_{s+1}^j + \phi_{s+1}^j \xi_s^j \right) - \partial_{\xi_{s+1}^j} \left( \phi_s^j \xi_{s+1}^j + \phi_{s+1}^j \xi_s^j \right) \right] \Pi$$

Playing with the index just like we did before eventually results in

$$A_{N-1}^1 = \sum_j \sum_s \frac{r}{\Omega} \left\{ \partial_{\xi_s^j} \left[ \phi_s^j \left( \xi_{s+1}^j - \xi_{s-1}^j \right) + \xi_s^j \left( \phi_{s+1}^j - \phi_{s-1}^j \right) \right] \right\} \Pi$$

The term  $B_{N-1}^1$  corresponds to

$$B_{N-1}^1 = \frac{\alpha}{z\Omega} \sum_j \sum_s \sum_{j' \in j} \left\{ \widehat{L}_{1j} \left[ \phi_s^j \left( -\sum_m \xi_m^{j'} \right) + \xi_s^j \left( 1 - \sum_m \phi_m^{j'} \right) \right] - \widehat{L}_{1j} \left[ \phi_s^{j'} \left( -\sum_m \xi_m^j \right) + \xi_s^{j'} \left( 1 - \sum_m \phi_m^j \right) \right] \right\} \Pi$$

which after making it explicit  $\widehat{L}_{1s}$  reads

$$B_{N-1}^1 = \frac{\alpha}{\Omega z} \left[ \sum_j \sum_s \sum_{j' \in j} \partial_{\xi_s^j} \left( -\phi_s^j \sum_m \xi_m^{j'} - \xi_s^j \sum_m \phi_m^{j'} + \xi_s^j - \xi_s^{j'} + \phi_s^{j'} \sum_m \xi_m^j + \xi_s^{j'} \sum_m \phi_m^j \right) \Pi - \sum_{j'} \sum_s \sum_{j \in j'} \partial_{\xi_s^{j'}} \left( -\phi_s^{j'} \sum_m \xi_m^j - \xi_s^{j'} \sum_m \phi_m^j + \xi_s^{j'} - \xi_s^j + \phi_s^j \sum_m \xi_m^{j'} + \xi_s^j \sum_m \phi_m^{j'} \right) \Pi \right] \quad (5.46)$$

Changing the index  $j'$  to  $j$  in the second combination of nested sum in equation (5.46) we can re-write the expression for  $B_{N-1}^1$  as:

$$B_{N-1}^1 = \frac{2\alpha}{\Omega z} \left[ \sum_j \sum_s \sum_{j' \in j} \partial_{\xi_s^j} \left( \xi_s^j - \xi_s^{j'} - \phi_s^j \sum_m \xi_m^{j'} - \xi_s^j \sum_m \phi_m^{j'} + \phi_s^{j'} \sum_m \xi_m^j + \xi_s^{j'} \sum_m \phi_m^j \right) \Pi \right]$$

We can then re-write the above equation in a completely equivalent form by adding in each of the sum a pair of fictitious quantities, each summing up to zero

$$\begin{aligned} 0 &= \xi_s^j \sum_m \phi_m^j - \xi_s^j \sum_m \phi_m^j \\ 0 &= \phi_s^j \sum_m \xi_m^j - \phi_s^j \sum_m \xi_m^j \end{aligned}$$

Re-ordering the terms so to bring in evidence differences of species (both mean-field and fluctuations terms) between consecutive micro-cells and recalling the definition (5.44) of discrete Laplacian yield

$$\begin{aligned} B_{N-1}^1 &= -\frac{\alpha}{\Omega} \sum_j \sum_s \partial_{\xi_s^j} \left( \Delta \xi_s^j + \xi_s^j \sum_m \Delta \phi_m^j - \Delta \phi_s^j \sum_m \xi_m^j + \phi_s^j \sum_m \Delta \xi_m^j \right. \\ &\quad \left. - \Delta \xi_s^j \sum_m \phi_m^j \right) \Pi \end{aligned}$$

Finally we focus on  $C_{N-1}^1$  and immediately get

$$C_{N-1}^1 = \sum_j \sum_s \partial_{\xi_s^j} \left( \frac{\beta_{out}}{\Omega} \xi_s^j + \frac{\beta_{in}}{\Omega} \sum_m \xi_m^j \right) \Pi$$

### Evaluating $A_{N-1}^2$ , $B_{N-1}^2$ and $C_{N-1}^2$

The contribution due to the second derivative in  $A$  is

$$A_{N-1}^2 = \frac{r}{\Omega} \sum_j \sum_s \frac{1}{2} \widehat{L}_{2s} (\phi_s^j \phi_{s+1}^j) \Pi$$

which equivalently reads

$$A_{N-1}^2 = \frac{1}{2} \frac{r}{\Omega} \sum_j \sum_s \phi_s^j \phi_{s+1}^j \left( \frac{\partial^2}{\partial (\xi_s^j)^2} + \frac{\partial^2}{\partial (\xi_{s+1}^j)^2} - 2 \frac{\partial^2}{\partial \xi_s^j \partial \xi_{s+1}^j} \right) \Pi$$

Then as concerns  $B_{N-1}^2$

$$\begin{aligned} B_{N-1}^2 &= \frac{\alpha}{z\Omega} \sum_j \sum_s \sum_{j' \in j} \frac{1}{2} \left\{ \widehat{L}_{2j} \left[ \phi_s^j \left( 1 - \sum_m \phi_m^{j'} \right) \Pi \right] \right. \\ &\quad \left. + \widehat{L}_{2j} \left[ \phi_s^{j'} \left( 1 - \sum_m \phi_m^j \right) \Pi \right] \right\} \\ &= \frac{1}{2} \frac{\alpha}{z\Omega} \sum_j \sum_s \sum_{j' \in j} \left[ \phi_s^j \left( 1 - \sum_m \phi_m^{j'} \right) + \phi_s^{j'} \left( 1 - \sum_m \phi_m^j \right) \right] \\ &\quad \times \left( \frac{\partial^2}{\partial (\xi_s^j)^2} + \frac{\partial^2}{\partial (\xi_s^{j'})^2} - 2 \frac{\partial^2}{\partial \xi_s^j \partial \xi_s^{j'}} \right) \Pi \end{aligned}$$

It should be noted that the following relation applies

$$\sum_j \sum_{j' \in j} \left[ \frac{\partial}{\partial \xi_s^j} - \frac{\partial}{\partial \xi_s^{j'}} \right]^2 = 2 \sum_j \sum_{j'} \left[ z \frac{\partial^2}{\partial (\xi_s^j)^2} \delta_{jj'} - \frac{\partial^2}{\partial \xi_s^j \partial \xi_s^{j'}} J_{\langle jj' \rangle} \right] \quad (5.47)$$

where  $J_{\langle jj' \rangle}$  is equal to 1 if  $j'$  and  $j$  are nearest neighbors, zero otherwise. This is a technicality which enables us to cast in a compact form the coefficients of the matrix  $\mathcal{B}$  defined below. It should be noted that the factor 4 in the coefficients of matrix  $\mathcal{B}$  originates from the factor 2 in equation (5.47).

Finally the  $C_{N-1}^2$  term is

$$\begin{aligned} C_{N-1}^2 &= \sum_j \frac{1}{2} \sum_s \left\{ \frac{\partial^2}{\partial (\xi_s^j)^2} \left[ \frac{\beta_{in}}{\Omega} \left( 1 - \sum_m \phi_m^j \right) \Pi \right] + \frac{\partial^2}{\partial (\xi_s^j)^2} \left( \frac{\beta_{out}}{\Omega} \phi_s^j \Pi \right) \right\} \\ &= \frac{1}{2} \sum_j \sum_s \left[ \frac{\beta_{in}}{\Omega} \left( 1 - \sum_m \phi_m^j \right) + \frac{\beta_{out}}{\Omega} \phi_s^j \right] \frac{\partial^2}{\partial (\xi_s^j)^2} \Pi \end{aligned}$$

#### 5.2.4 The Fokker Planck equation

Equating the orders  $N^{-1}$  in the Master equation leads to the following Fokker Planck equation which governs the probability distribution function of fluctuations:

$$\frac{\partial \Pi}{\partial \tau} = - \sum_j \sum_s \frac{\partial}{\partial \xi_s^j} \left[ \sum_{l,m} \mathcal{A}_{js,lm} \xi_l^m \Pi \right] + \frac{1}{2} \sum_{j,j'} \sum_r \sum_q \frac{\partial^2}{\partial \xi_r^j \partial \xi_s^{j'}} \left[ \mathcal{B}_{jj',qs} \Pi \right]$$

The matrices  $\mathcal{A}$  and  $\mathcal{B}$  are defined on the basis of the above calculations. In particular we shall concentrate on the analysis of fluctuations around the fixed point. This is obtained by imposing  $\phi_s^j = \phi^*$  for each choice of  $s$  and  $j$ . In the following, the structures of the matrices  $\mathcal{A}$  and  $\mathcal{B}$  are discussed. Their elements are expressed as an explicit function of the chemical parameters specifying the model at hand.

The matrix  $\mathcal{A}$  has dimension  $k\Omega \times k\Omega$  and it can be explicitly written as

$$\mathcal{A} = \begin{bmatrix} \mathcal{A}_0 & \mathcal{C}_1 & 0 & 0 & \dots & \mathcal{C}_1 \\ \mathcal{C}_1 & \mathcal{A}_0 & \mathcal{C}_1 & 0 & \dots & 0 \\ 0 & \mathcal{C}_1 & \mathcal{A}_0 & \mathcal{C}_1 & \dots & 0 \\ 0 & 0 & \mathcal{C}_1 & \mathcal{A}_0 & \dots & 0 \\ \dots & \dots & \dots & \dots & \dots & \dots \\ 0 & 0 & 0 & 0 & \dots & \mathcal{C}_1 \\ \mathcal{C}_1 & 0 & 0 & 0 & \dots & \mathcal{A}_0 \end{bmatrix}$$

where  $\mathcal{A}_0$  is a circulant  $k \times k$  matrix

$$\mathcal{A}_0 = \begin{bmatrix} a_0 & a_1 & a_2 & a_2 & \dots & a_3 \\ a_3 & a_0 & a_1 & a_2 & \dots & a_2 \\ a_2 & a_3 & a_0 & a_1 & \dots & a_2 \\ a_2 & a_2 & a_3 & a_0 & \dots & a_2 \\ \dots & \dots & \dots & \dots & \dots & \dots \\ a_2 & a_2 & a_2 & a_2 & \dots & a_1 \\ a_1 & a_2 & a_2 & a_2 & \dots & a_0 \end{bmatrix}$$

and  $\mathcal{C}_1$  is also  $k \times k$  and takes the form

$$\mathcal{C}_1 = \begin{bmatrix} c_0 & c_1 & c_1 & c_1 & \dots & c_1 \\ c_1 & c_0 & c_1 & c_1 & \dots & c_1 \\ c_1 & c_1 & c_0 & c_1 & \dots & c_1 \\ c_1 & c_1 & c_1 & c_0 & \dots & c_1 \\ \dots & \dots & \dots & \dots & \dots & \dots \\ c_1 & c_1 & c_1 & c_1 & \dots & c_1 \\ c_1 & c_1 & c_1 & c_1 & \dots & c_0 \end{bmatrix}$$

The elements of such matrices follow from the calculation developed above and read

$$\begin{aligned} a_0 &= -\frac{2\alpha}{\Omega} [1 - (k-1)\phi^*] - \frac{\beta_{in}}{\Omega} - \frac{\beta_{out}}{\Omega} \\ a_1 &= -\frac{2\alpha}{\Omega}\phi^* - \frac{r}{\Omega}\phi^* - \frac{\beta_{in}}{\Omega} \\ a_2 &= -\frac{2\alpha}{\Omega}\phi^* - \frac{\beta_{in}}{\Omega} \\ a_3 &= -\frac{2\alpha}{\Omega}\phi^* + \frac{r}{\Omega}\phi^* - \frac{\beta_{in}}{\Omega} \\ c_0 &= \frac{2\alpha}{z\Omega} [1 - (k-1)\phi^*] \\ c_1 &= \frac{2\alpha}{z\Omega}\phi^* \end{aligned}$$

The coefficient of matrix  $\mathcal{B}$  are

$$\mathcal{B}_{jj',qs} = \begin{cases} -2\frac{r}{\Omega}\phi^*\phi^*\delta_{jj'} & \text{if } |q-s|=1 \\ \left[ 2\frac{r}{\Omega}\phi^*\phi^* + \frac{4\alpha}{\Omega}\phi^*(1-k\phi^*) \right. \\ \left. + \frac{\beta_{in}}{\Omega}(1-k\phi^*) + \frac{\beta_{out}}{\Omega}\phi^* \right] \delta_{jj'} \\ -4\frac{\alpha}{z\Omega}\phi^*(1-k\phi^*)J_{<jj'>} & \text{if } q=s \\ 0 & \text{otherwise} \end{cases}$$

More specifically matrix  $\mathcal{B}$  is  $k\Omega \times k\Omega$  and has the following structure:

$$\mathcal{B} = \begin{bmatrix} \mathcal{B}_0 & \mathcal{B}_1 & 0 & 0 & \dots & 0 & \mathcal{B}_1 \\ \mathcal{B}_1 & \mathcal{B}_0 & \mathcal{B}_1 & 0 & \dots & 0 & 0 \\ 0 & \mathcal{B}_1 & \mathcal{B}_0 & \mathcal{B}_1 & \dots & 0 & 0 \\ 0 & 0 & \mathcal{B}_1 & \mathcal{B}_0 & \dots & 0 & 0 \\ \dots & \dots & \dots & \dots & \dots & \dots & \dots \\ 0 & 0 & 0 & 0 & \dots & \mathcal{B}_0 & \mathcal{B}_1 \\ \mathcal{B}_1 & 0 & 0 & 0 & \dots & \mathcal{B}_1 & \mathcal{B}_0 \end{bmatrix}$$

where  $\mathcal{B}_0$  is a  $k \times k$  matrix defined as:

$$\mathcal{B}_0 = \begin{bmatrix} b_0 & b_1 & 0 & 0 & \dots & 0 & b_1 \\ b_1 & b_0 & b_1 & 0 & \dots & 0 & 0 \\ 0 & b_1 & b_0 & b_1 & \dots & 0 & 0 \\ 0 & 0 & b_1 & b_0 & \dots & 0 & 0 \\ \dots & \dots & \dots & \dots & \dots & \dots & \dots \\ 0 & 0 & 0 & 0 & \dots & b_0 & b_1 \\ b_1 & 0 & 0 & 0 & \dots & b_1 & b_0 \end{bmatrix}$$

and  $\mathcal{B}_1$  is also a  $k \times k$  matrix:

$$\mathcal{B}_1 = \begin{bmatrix} b_2 & 0 & 0 & \dots & 0 \\ 0 & b_2 & 0 & \dots & 0 \\ 0 & 0 & b_2 & \dots & 0 \\ \dots & \dots & \dots & \dots & \dots \\ 0 & 0 & 0 & \dots & b_2 \end{bmatrix}$$

The coefficients  $b_0, b_1, b_2$  read:

$$\begin{aligned} b_0 &= 2\frac{r}{\Omega}\phi^*\phi^* + \frac{4\alpha}{\Omega}\phi^*(1 - k\phi^*) + \frac{\beta_{in}}{\Omega}(1 - k\phi^*) + \frac{\beta_{out}}{\Omega}\phi^* \\ b_1 &= -2\frac{r}{\Omega}\phi^*\phi^* \\ b_2 &= -4\frac{\alpha}{z\Omega}\phi^*(1 - k\phi^*) \end{aligned}$$

Having defined the matrices  $\mathcal{A}$  and  $\mathcal{B}$ , we are in the position to obtain an analytical expression for the power spectrum for the fluctuations. This is achieved via a straightforward procedure which is essentially analogous to that reported in section 5.1.1. Just a few technical points need to be carefully handled, as clarified in [84]. Here, we are solely concerned with presenting a preliminary gallery of results which testifies on the predictive ability of our analysis.

In Fig. 5.8 the (two dimensional) analytical and numerical power spectra are displayed, for the case where  $k = 4$ . Clearly, the power spectra are now function of the time–frequency  $\omega$  and space–frequency  $\kappa$ . The migration parameter  $\alpha$  is set to zero so that the system is practically composed by  $\Omega$ , independent replica of the Togashi and Kaneko setting. The other parameters are set to the same values as adopted in Fig. 5.3. As expected, a peak at  $k = 4$  is observed, and no spatial modulation recorded. Direct simulations agree with the theoretically predicted profile. We then turn on the migration effect and set  $\alpha = 0.1$ , see Fig. 5.9a. The system still exhibits the peak for  $\omega = 4$ , but now a decay in  $k$  is predicted to occur. This feature is then observed in the simulations (see Fig. 5.9b), again pointing to the validity of the perturbative development, and suggesting that the system organizes collective modes on the large wavelength scale. We notice that a similar effect is also reported by Lugo and McKane in [86] for their spatial predator–prey model.

Preliminary simulations (not reported here) where the species are differentiated with respect to their chemical activity (different rates) shows a large zoology of allowed spatio–temporal patterns, including the existence of isolated peaks in the power spectra, see [84] for an extended discussion.

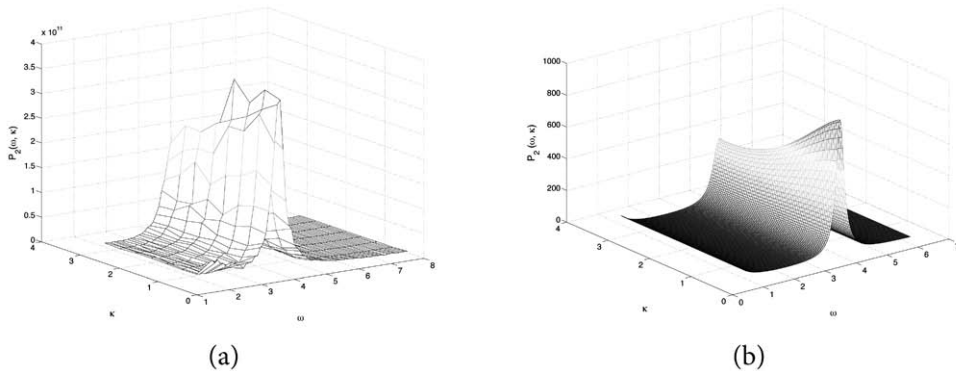


Figure 5.8: Numerically (panel (a)) and analytically (panel (b)) obtained power spectrum for a system with  $k = 4$ . Parameters used for the simulations are  $r = 10$ ,  $\alpha = 0$ ,  $\beta_{in} = 10/64$ ,  $\beta_{out} = 10/64$ ,  $\Omega = 16$ ,  $N = 5000$ . The numerical power spectrum is obtained from 100 runs of the stochastic simulation.

As a final remark, we wish to stress that the emergence of regular spatio-temporal oscillations in the concentration amount might have important implications for the dynamics of the so-called protocells. These are small-cell like, living, units, which can self-assemble, develop and replicate. Autocatalytic chemical reactions might have occurred inside those primordial containers back to the origin of life, and could have hypothetically contributed to mediate the minimal mechanisms involved in duplication. These aspects are little understood, despite the fact that lipidic vesicles (i.e. the candidate representative of the protocells' family) are nowadays heavily studied in laboratories. In a future work we intend to explore the possibility that the division process is initiated by a Turing instability, i.e. following from a purely spatial effect of the type investigated in this chapter.

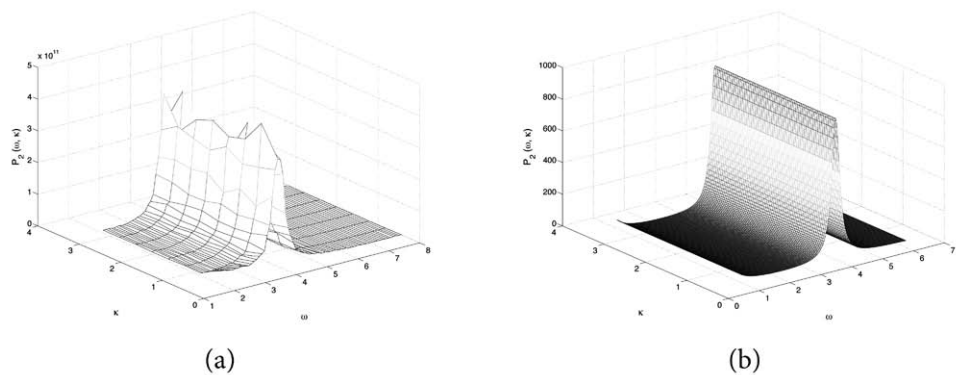


Figure 5.9: Numerically (panel (a)) and analytically (panel (b)) obtained power spectrum for a system with  $k = 4$ . Parameters used for the simulations are  $r = 10$ ,  $\alpha = 0.1$ ,  $\beta_{in} = 10/64$ ,  $\beta_{out} = 10/64$ ,  $\Omega = 16$ ,  $N = 5000$ . The numerical power spectrum is obtained from 100 runs of the stochastic simulation.



## Conclusions

Microscopic systems, such as the intracellular environment, are characterized by pronounced biochemical oscillations that the standard deterministic approach fails to capture. This observation has stimulated the research of novel theoretical frameworks to interpret the large class of intriguing scenarios characterizing these systems. In particular, the discrete nature of the system, which can be microscopically segmented in independent entities, can yield to an effective stochastic resonance, resulting in amplified regular cycles. Finite size contributions do matter and may hence cause complex dynamical patterns for the populations under inspection.

In this thesis we have investigated this crucial aspect with reference to a selected gallery of problems. First, focusing on pain perception, we have developed a discrete dynamical framework to study the molecular processes which are activated in response to an external harming stimulus. These cascade of reactions ultimately triggers the pain sensation. The problem has been analyzed, paying special attention to the associated finite-size effects. Through the van Kampen perturbative theory, we are able to recover an exact analytic description of the fluctuations. We were in particular interested in elucidating the crucial interplay between the administered drug molecules, which express their analgesic function chasing the target receptors, and other chemical elements freely diffusing in the bloodstream. The latter can substantially reduce the anaesthetic effect, by hindering the available binding sites. Similarly, drug molecules can be turned into inactive species following binary encounters. The mechanisms here postulated were formally coded via chemical reactions and define a consistent stochastic scheme. Numerical simulations displayed macroscopic oscillations in the concentration amount: the number of bound receptors changed cyclically in time, a trend which we assumed to induce an analogous modulation for the experienced perception of pain. It is important to remark that the amplification process here discussed stems from the underlying stochasticity, which is resonant with the natural frequencies of the system. Oscillations arise hence spontaneously, driven by the noise which is intrinsic to the system and without invoking any ad hoc couplings among the molecular agents participating to the dynamics. Our findings suggest the existence of a simple, though general, molecular mechanism responsible for the emergence of cyclic behaviors in response to analgesic treatments.

An extension of the model included drug-metabolite interactions where different populations compete for the same target receptors, so to induce analgesia. The system has been analyzed, focusing first on the mean-field dynamics ( $N \rightarrow \infty$ ) which is governed by a set of coupled ordinary differential equations for the species amount. The fixed points have been studied together with their associated stability properties. The

chemical parameters are found to control the asymptotic regime determining the effectiveness of the administered therapy. More interestingly, in the transient dynamics a lethargic phase is registered, where the number of bound receptors appear to have stabilized to a quota sensitive to initial condition, before reaching their equilibrium solution. Moreover, fluctuations have been also analyzed via the van Kampen technique. It is here speculated that, in particular cases, they might influence the degree of experienced pain, which could hence change over time.

Another context where intrinsic noise may have important effects on the dynamics is that of the auto-catalytic networks. These kind of reactions are central in many different contexts and play an important role in intracellular biochemical reaction schemes. In this latter scenario, species are confined in a closed volume, delimited by the cellular membrane. Low concentration can occasionally develop resulting from the complex mutual interaction between microscopic actors. Under such conditions, fluctuations matter and the effects of the intrinsic discreteness need to be properly accounted for. In other words, continuous kinetic equations prove inadequate, finite size corrections becoming significant. These aspects were numerically substantiated by Togashi and Kaneko [77, 78] within the framework of a simplified system of  $k$  coupled autocatalytic reactions. In this thesis we elaborate on this concept by studying analytically the associated master equation via a systematic expansion in power of  $N^{-1/2}$ , where  $N$  is the system size. To leading order, the mean-field rate equations are recovered, while higher order corrections enable us to explain the large amplitude of the oscillations as detected in direct simulations. Importantly, the calculation applies to arbitrary values of  $k$ . For  $k = 4$  a peak in the power spectrum is found, while for  $k = 8$  two peaks develop. To the best of our knowledge, this is the first time that a double-peaked power spectrum has been predicted to emerge as a resonant effect, within a van Kampen type of analysis. In both cases, theory and simulations agree well thus confirming the importance of finite  $N$  contributions. Later on we have extended our work by taking spatial effects into account. Also in this case, we detected spatio-temporal oscillations in the species concentration, which are again driven by the discreteness of the system components.

In addition to finite-size effects problems, a short part of this thesis has been devoted to describe new method for analyzing experimental data relative to drugs kinetics and to microarray experiments.

First, we have proposed a mathematical model for the kinetics of tramadol. This novel theoretical framework could result in an objective criterion on how to adjust the assigned dose, depending on the genetic polymorphisms of CYP2D6. The model describes the coupled dynamics of tramadol and the metabolite O-desmethyl-tramadol. The effect of diffusion of the drug in the blood is here accounted for and we further hypothesize the existence of a time delay in the process of chemical translation from tramadol into metabolites. The system of coupled differential equations is solved numerically and the free parameters adjusted so to interpolate the experimental time series for the intravenous injection setting. Theoretical curves are shown to reproduce correctly the experimental profiles obtained from clinical trials. This enables in turn to extract an estimate of the metabolization rate. A difference in metabolization rate between CYP2D6 poor and extensive metabolizers is also found, and the stereoselectivity in the O-demethylation of tramadol highlighted. Our results allow one to quantify the dose of (+)-tramadol (resp. (-)-tramadol) administered to poor or extensive metabolizers, if the same effect is sought. The latter is here quantified through the blood

concentration of (+)-metabolites (resp. (-)-metabolites).

As for the microarray experiments, we have developed a method for measuring the distance among records based on the correlations among available data, with the aim of estimating the missing values. Finally, we have reviewed the Van Dongen algorithm, suggesting a new method for detecting different levels of communities, i.e. clusters of homogeneous objects with respect to a predefined norm.



## Chapter A

### A technique to simulate the full stochastic process: The Gillespie algorithm

In 1976 Daniel T. Gillespie proposed an algorithm to exactly simulate the stochastic dynamics of chemical reactions [79, 82]. To describe this method, let us consider a volume  $V$  which contains molecules of  $N$  chemically active species  $S_i$  for  $i = 1, \dots, N$ , and denote by  $X_i$  the current number of molecules of species  $S_i$  in  $V$ . The molecules interact according to  $M$  chemical reactions  $R_\mu$  for  $\mu = 1, \dots, M$ , each characterized by a reaction parameter  $c_\mu$ . The quantity  $c_\mu \delta t$  represents the first order approximation<sup>1</sup> of the average probability that a particular combination of  $R_\mu$  reactant molecules will react accordingly in the next time interval  $\delta t$ , as it follows by a chemical kinetics theory derived into details in the original paper [79].

To illustrate the relationship between  $c_\mu$  and the more familiar “reaction rate constant”  $k_\mu$  used in the deterministic formulation of chemical kinetics, let us consider the reaction  $S_1 + S_2 \longrightarrow 2S_3$ . In this case,  $X_1 X_2 \cdot c_\mu dt$  is the probability that the reaction will occur inside  $V$  in the next time interval  $dt$ , where  $X_1 X_2$  represents the distinct combinations of reactant molecules in  $V$ . Averaging over a set of stochastically identical system, and diving by  $V$ , we obtain the average reaction rate per unit time  $\langle X_1 X_2 \rangle c_\mu / V$  or, in terms of molecular concentrations  $x_i = X_i / V$ ,  $\langle x_1 x_2 \rangle c_\mu V$ . If we divide this latter quantity by the product of the average densities of the reactants, we obtain the expression for  $k_\mu$ , namely

$$k_\mu = \frac{\langle x_1 x_2 \rangle c_\mu V}{\langle x_1 \rangle \langle x_2 \rangle} \quad (\text{A.1})$$

In the deterministic formulation the average of a product is equivalent to the product of the averages, thus  $\langle x_1 x_2 \rangle = \langle x_1 \rangle \langle x_2 \rangle$  and (A.1) simplifies to

$$k_\mu = V c_\mu$$

The factor  $V$  in this relation is due to the type of reaction considered. In reactions with only one reactant molecule, indeed, the factor  $V$  would be absent, while in those with three reactants, a  $V^2$  would instead appear.

The aim of the method is to simulate the time evolution of the  $N$  variables  $X_i$  knowing their initial values  $X_i(0)$ , the  $M$  reactions  $R_\mu$  and the associated reaction parame-

<sup>1</sup> More precisely, the first order in  $\delta t$  means that the average probability is  $c_\mu \delta t + o(\delta t)$  with  $\lim_{\delta t \rightarrow 0} o(\delta t) / \delta t = 0$ .

Reaction	$h_\mu$
$S_j \longrightarrow$ reaction products	$X_j$
$S_j + S_k \longrightarrow$ reaction products	$X_j X_k$
$2S_j \longrightarrow$ reaction products	$X_j(X_j - 1)/2$
$S_i + S_j + S_k \longrightarrow$ reaction products	$X_i X_j X_k$
$S_j + 2S_k \longrightarrow$ reaction products	$X_j X_k(X_k - 1)/2$
$3S_j \longrightarrow$ reaction products	$X_j(X_j - 1)(X_j - 2)/6$

Table A.1: A selection of possible reactions and their corresponding state variables  $h_\mu$ .

ters  $c_\mu$ . The standard stochastic approach to this problem focuses on the master equation, namely the time evolution of the probability function  $P(X_1, \dots, X_N; t)$  to have  $X_i$  molecules of  $S_i$  (for  $i = 1, \dots, N$ ) at time  $t$ . In most cases this approach turns out to be intractable, both analytically and numerically. To overcome this problem, Gillespie proposed a method based on what he called the reaction probability density function  $P(\tau, \mu)$ . He defined this quantity as the probability at time  $t$  that the next reaction in  $V$  will occur in the time interval  $(t + \tau, t + \tau + \delta\tau)$  and that the selected reaction was of the type  $R_\mu$ .

The first step for deriving an analytical expression for  $P(\tau, \mu)$ , consists in associating to every chemical reaction, a state variable  $h_\mu$  defined as the distinct molecular reactant combinations for reaction  $R_\mu$  within the volume  $V$  at time  $t$ . Table A shows the state variables for a selection of reactions. In this way  $h_\mu c_\mu \delta t$  is the probability, to first order in  $\delta t$ , that an  $R_\mu$  reaction occurs in  $V$ , in the next time interval  $\delta t$ .

The second step requires decomposing  $P(\tau, \mu)$  as

$$P(\tau, \mu) d\tau = P_0(\tau) \cdot h_\mu c_\mu d\tau \quad (\text{A.2})$$

where  $P_0(\tau)$  is the probability at time  $t$  that no reaction will occur in the time interval  $(t, t + \tau)$ , and  $h_\mu c_\mu d\tau$  is the probability that an  $R_\mu$  reaction will occur in the next differential time interval  $(t + \tau, t + \tau + d\tau)$ .

To calculate  $P_0(\tau)$  one can divide the interval  $(t, t + \tau)$  in  $K$  subintervals of equal length  $\epsilon = \tau/K$ . In each subinterval, the probability that none of the reactions occurs is given by

$$\prod_{\nu=1}^M [1 - h_\nu c_\nu \epsilon + o(\epsilon)] = 1 - \sum_{\nu=1}^M h_\nu c_\nu \epsilon + o(\epsilon) \quad (\text{A.3})$$

In this way,  $P_0(\tau)$  is just the product of  $K$  times equation (A.3)

$$\begin{aligned} P_0(\tau) &= \left[ 1 - \sum_{\nu=1}^M h_\nu c_\nu \epsilon + o(\epsilon) \right]^K \\ &= \left[ 1 - \sum_{\nu=1}^M h_\nu c_\nu \frac{\tau}{K} + o(K^{-1}) \right]^K \end{aligned}$$

This relation holds for any  $K > 1$ , and therefore it is true for infinitely large value of  $K$ :

$$\begin{aligned} P_0(\tau) &= \lim_{K \rightarrow \infty} \left[ \frac{1 - \sum_{\nu=1}^M h_{\nu} c_{\nu} \tau + o(K^{-1})K}{K} \right]^K \\ &= \exp \left[ - \sum_{\nu=1}^M h_{\nu} c_{\nu} \tau \right] \end{aligned} \quad (\text{A.4})$$

Putting together equation (A.2) with equation (A.4) one obtains the exact expression for the probability density function

$$P(\tau, \mu) = h_{\mu} c_{\mu} \exp \left[ - \sum_{\nu=1}^M h_{\nu} c_{\nu} \tau \right] \quad (\text{A.5})$$

for  $0 \leq \tau < \infty$  and  $1 \leq \mu \leq M$  with  $\tau \in \mathbb{R}$  and  $\mu \in \mathbb{N}$ .

Before moving to the description of the algorithm, we recall the main ideas of a Monte Carlo method. This latter constitutes a crucial step in the Gillespie implementation, providing a method to generate two random numbers  $\tau$  (real) and  $\mu$  (integer) according to the joint probability density function in (A.5). The trick consists in splitting the probability density function  $P(\tau, \mu)$  into the product of two one-variable probability density functions. This procedure is called conditioning and leads to

$$P(\tau, \mu) = P_1(\tau) \cdot P_2(\mu|\tau) \quad (\text{A.6})$$

where  $P_1(\tau)d\tau$  is the probability that the next reaction will occur between times  $t + \tau$  and  $t + \tau + d\tau$ , and  $P_2(\mu|\tau)$  is the probability that the next reaction will be an  $R_{\mu}$  type, given that it happens at time  $t + \tau$ . Invoking the addition theorem for probabilities,  $P_1(\tau)d\tau$  is obtained by summing  $P(\tau, \mu)d\tau$  over all  $\mu$ , and thus

$$P_1(\tau) = \sum_{\mu=1}^M P(\tau, \mu)$$

Putting this into (A.6) and solving for  $P_2(\mu|\tau)$  it gives

$$P_2(\mu|\tau) = P(\tau, \mu) / \sum_{\nu=1}^M P(\tau, \nu)$$

Substituting  $P(\tau, \mu)$  with (A.5) in the previous two equations, we obtain

$$P_1(\tau) = \begin{cases} a \exp[-a\tau] & \text{for } 0 \leq \tau < \infty \\ 0 & \text{otherwise} \end{cases} \quad (\text{A.7})$$

and

$$P_2(\mu|\tau) = \begin{cases} a_{\mu} / \sum_{\nu=1}^M a_{\nu} & \text{for } \nu = 1, \dots, M \\ 0 & \text{otherwise} \end{cases} \quad (\text{A.8})$$

where

$$a = \sum_{\mu=1}^M a_{\mu}$$

with

$$a_\mu = h_\mu c_{mu} \quad \text{for } \mu = 1, \dots, M \quad (\text{A.9})$$

In this way the problem of finding two random numbers according to  $P(\tau, \mu)$  may be recast as the problem of drawing a real random number from the  $P_1$  distribution, and an integer random number according to  $P_2$ .

Let us first focus on the former case. We wish to generate a real number  $x$  according to a probability density function  $P(x)$ . The corresponding probability distribution function

$$F(x_0) = \int_{-\infty}^{x_0} P(x) dx \quad (\text{A.10})$$

quantifies the probability that  $x$  will be less than  $x_0$ . The inversion method for generating a random value  $x$  according to  $P(x)$  is to draw a random number  $r$  from the uniform distribution in the unit interval, and then take

$$x = F^{-1}(r) \quad (\text{A.11})$$

To prove that this procedure is correct, we have to show that the probability that the  $x$  value so generated will lie between  $x'$  and  $x' + dx'$ , is  $P(x')dx'$ . By construction, this is equivalent to calculating the probability that  $r$  will lie between  $F(x')$  and  $F(x' + dx')$ . Since  $r$  is a random number drawn from the uniform distribution in the unit interval, this probability is just the length of the interval  $[F(x'), F(x' + dx')]$ , namely  $F(x' + dx') - F(x') = F'(x')dx'$ . Applying the definition (A.10), we get

$$F(x' + dx') - F(x') = F'(x')dx' = P(x')dx'$$

and this prove that the probability density function for the random number  $x$  generated according to (A.11) is indeed  $P(x)$ .

For the specific case at hand, we wish to generate a random number  $\tau$  according to the probability density function (A.7). In this case  $F(\tau) = 1 - \exp[-a\tau]$ . Putting  $F(\tau) = r$  and inverting the function  $F$ , we obtain

$$\tau = \frac{1}{a} \ln\left(\frac{1}{r}\right) \quad (\text{A.12})$$

where, for simplicity, we have replaced the random variable  $1 - r$  by the statistically equivalent random variable  $r$ .

We have seen how to generate a random number according to a specific probability density distribution for a continuous variable. Now we consider the discrete case and we look for a method which enables us to obtain a random integer  $i$  according to the probability density function  $P(j)$ , where now  $P(j)$  is the probability that  $i = j$ . The corresponding distribution function  $F(i)$  is defined by

$$F(i) = \sum_{j=-\infty}^i P(j)$$

and  $F(i_0)$  represents the probability that  $i \leq i_0$ . With analogy to the continuous case, the inversion method consists in drawing a random number  $r$  from the uniform distribution in the unit interval and take for  $i$  that value which satisfies

$$F(i - 1) < r \leq F(i) \quad (\text{A.13})$$

To show that the procedure is correct also in this case, we use the fact the resulting integer  $i$  will equal  $j$  is equivalent to the probability that  $r$  will lie between  $F(j-1)$  and  $F(j)$ . So we have

$$F(j) - F(j-1) = \sum_{k=-\infty}^j P(k) - \sum_{k=-\infty}^{j-1} P(k) = P(j)$$

This proves that  $P(i)$  is indeed the probability density function for the random integer  $i$  generated according to (A.13).

As an example, we consider again our specific case, and make it explicit the expression of the random integer  $\mu$  with respect to the density function (A.8). Applying (A.13) we see that we have to select the integer  $\mu$  so that

$$\sum_{\nu=1}^{\mu-1} P_2(\nu|\tau) < r \leq \sum_{\nu=1}^{\mu} P_2(\nu|\tau)$$

or

$$\sum_{\nu=1}^{\mu-1} a_{\nu} < r \sum_{\nu=1}^M a_{\nu} \leq \sum_{\nu=1}^{\mu} a_{\nu} \quad (\text{A.14})$$

Now we have all the ingredients to describe the details of the simulation methods. The steps of the algorithm are the following:

**Step0** Assign values to the  $M$  reaction constants  $c_1, \dots, c_M$  and initialize the  $N$  molecular population numbers  $X_1, \dots, X_N$ . Set the time variable  $t = 0$ , and specify a stopping time  $t_{stop}$ .

**Step1** Calculate the quantities  $a_{\nu} = h_{\nu} c_{\nu}$  for  $\nu = 1, \dots, M$  for the current molecular population numbers, and the quantity  $a_0 = \sum_{\nu=1}^M a_{\nu}$ .

**Step2** Use the Monte Carlo technique to generate a random pair  $(\tau, \mu)$  according to (A.12) and (A.14).

**Step3** According to the numbers  $\tau$  and  $\mu$  generated in the previous step, advance time by  $\tau$  ( $t = t + \tau$ ) and update the values of  $X_i$  for every species involved in reaction  $R_{\mu}$ .

**Step4** If  $t < t_{stop}$  go to step1, otherwise terminate the calculation.

It is important to stress that the time series generated with this algorithm recover the exact probability distribution function given by the master equation. It can be shown, in fact, that the two approaches, the master equation and the Gillespie's method, are equivalent at the first order approximation grounded on the kinetic theory argument mentioned before.



## Bibliography

- [1] Hofbauer J and Sigmund K. *Evolutionary Games and Population Dynamics*. Cambridge University Press, 1998.
- [2] Murray JD. *Mathematical Biology I: An Introduction*. Springer-Verlag, third edition, 2002.
- [3] Gopalsamy K. *Stability and Oscillations in Delay Differential Equations of Population Dynamics*. Kluwer Academic Publisher, 1992.
- [4] Mahaffy J, Belair J, and Mackey M. Hematopoietic model with moving boundary condition and state dependent delay: Applications in erythropoiesis. *J Theor Biol*, 190:135–146, 1998.
- [5] Murray JD. *Mathematical Biology II: Spatial Models and Biomedical Applications*. Springer-Verlag, third edition, 2003.
- [6] McKane AJ and Newman TJ. Predator-prey cycles from resonant amplification of demographic stochasticity. *Phys Rev Lett*, 94:218102, 2005.
- [7] McKane AJ, Nagy JD, Newman TJ, and Stefanini MO. Amplified biochemical oscillations in cellular systems. *J Stat Phys*, 128:165–191, 2007.
- [8] Alonso D, McKane AJ, and Pascual M. Stochastic amplification in epidemics. *J. R. Soc. Interface*, 4:575–582, 2007.
- [9] Melzack R and Casey KL. Sensory, motivational, and central control determinants of pain: A new conceptual model. In Kenshalo D, editor, *The skin senses*, pages 423–429. Charles C. Thomas, Springfield, IL, 1968.
- [10] *Principles of Neural Science*. McGraw-Hill, fourth edition, 2000.
- [11] Freudenrich C. How pain works. <http://health.howstuffworks.com/pain.htm>.
- [12] NIDA National Institute on Drug Abuse (The Science of Drug Abuse & Addiction). <http://www.nida.nih.gov/pubs/Teaching/Teaching2/Teaching2.html>, 2008.
- [13] Module 1 Pain Management: Pathophysiology of Pain and Pain Assessment. American Medical Association, 2007–2009.
- [14] Gracely RH and Kwilosz DM. The descriptor differential scale: applying psychophysical principles to clinical pain assessment. *Pain*, 35:279–288, 1988.

- [15] Gamsa A. The role of psychological factors in chronic pain. I. A half century of study. *Pain*, 57:5–15, 1994.
- [16] The endogenous opioid system. [www.wehealny.org/stoppain/pcd/\\_pdf](http://www.wehealny.org/stoppain/pcd/_pdf).
- [17] Wilkinson GR. Pharmacokinetics: the dynamics of drug absorption, distribution and elimination. In Hardman JC, Limbird LE, and Gilman AG, editors, *Goodman & Gilman's the pharmacological basis of therapeutics*, pages 3–29. McGraw–Hill, New York, 10th edition, 2001.
- [18] Ingelman-Sundberg M. Genetic polymorphisms of cytochrome P4502D6 (CYP2D6): clinical consequences, evolutionary aspects and functional diversity. *Pharmacogenomics J*, 5:6–13, 2005.
- [19] Raimundo S, Toscano C, Klein K, and et al. A novel intronic mutation, 2988G>A, with high predictivity for impaired function of cytochrome P450 2D6 in white subjects. *Clin Pharmacol Ther*, 76:128–138, 2004.
- [20] Goldstein JA, Ishizaki T, Chiba K, and et al. Frequencies of the defective CYP2C19 alleles responsible for the mephenytoin poor metabolizer phenotype in various Oriental, Caucasian, Saudi Arabian and American black populations. *Pharmacogenetics*, 7:59–64, 1997.
- [21] Bertilson L, Dahl ML, Dalen P, and Al-Shurbaji A. Molecular genetics of CYP2D6: Clinical relevance with focus on psychotropic drugs. *Br J Clin Pharmacol*, 53:111–122, 2002.
- [22] Ikenaga Y, Fukuda T, Fukuda K, and et al. The frequency of candidate alleles for CYP2D6 genotyping in the Japanese population with an additional respect to the -1584C to G substitution. *Drug Metab Pharmacokinet*, 20:113–116, 2005.
- [23] Wennerholm A, Johansson I, Idestrand M, Bertilsson L, Gustafsson LL, and Ingelman-Sundberg M. Characterization of the CYP2D6\*29 allele commonly present in black Tanzanian population causing reduced catalytic activity. *Pharmacogenetics*, 11:417–427, 2001.
- [24] Mikus G and Weiss J. Influence of CYP2D6 genetics on opioid kinetics, metabolism and response. *Current Pharmacogenomics*, 3:43–52, 2005.
- [25] Grond S and Sablotzki A. Clinical pharmacology of tramadol. *Clin Pharmacokinet*, 43:879–923, 2004.
- [26] Raffa RB, Friderichs E, Reimann W, and et al. Complementary and synergistic antinociceptive interaction between the enantiomers of tramadol. *J Pharmacol Exp Ther*, 267:331–40, 1993.
- [27] Gillen C, Haurand M, Kobelt DJ, and et al. Affinity, potency and efficacy of tramadol and its metabolites at the cloned human mu-opioid receptor. *Naunyn Schmiedebergs Arch Pharmacol*, 362:116–21, 2000.
- [28] Rojas MJ, Navas JA, and Rector DM. Evoked response potential markers for anesthetic and behavioral states. *Am J Physiol Regul Integr Comp Physiol*, 291:R189–R196, 2006.

- [29] Holford NH and Sheiner LB. Understanding the dose–effect relationship: clinical application of pharmacokinetic–pharmacodynamic models. *Clin Pharmacokinet*, 1981.
- [30] Katzung BG. *Basic & Clinical Pharmacology*. McGraw–Hill Medical, 2003.
- [31] Makoid MC, Vuchetich PJ, and Banakar UV. *Basic Pharmacokinetics*. The Virtual University Press, first edition, Updated at December 2008. <http://pharmacyonline.creighton.edu/pha443/pdf/default.htm>.
- [32] Eichelbaum M, Ingelman-Sundberg M, and Evans WE. Pharmacogenomics and individualized drug therapy. *Annual Review of Medicine*, 57:119–137, 2005.
- [33] Stamer UM, Bayerer B, and Stüber F. Genetics and variability in opioid response. *European Journal of Pain*, 9:101–104, 2004.
- [34] Subrahmanyaam S, Renwick AB, Walters DG, Young PJ, Price RJ, Tonelli AP, and Lake BG. Identification of cytochrome P–450 isoforms responsible for cis–tramadol metabolism in human liver microsomes. *Drug Metabolism and Disposition*, 29:1146–1155, 2001.
- [35] Weiss M. Analysis of metabolite formation pharmacokinetics after intravenous and oral administration of the parent drug using inverse Laplace transformation. *Drug Metabolism and Disposition*, 26:562–565, 1998.
- [36] Lötsch J, Weiss M, Kobal G, and Geisslinger G. Pharmacokinetics of morphine–6–glucuronide and its formation from morphine after intravenous administration. *Clinical Pharmacology & Therapeutics*, 63:629–693, 1998.
- [37] Luan PG and Kao YM. Drifting diffusion on a circle as a continuous limit of a multiurn Ehrenfest model. *Physical Review E*, 69:022102, 2004.
- [38] Pedersen RS, Damkier P, and Brøsen K. Enantioselective pharmacokinetics of tramadol in CYP2D6 extensive and poor metabolizers. *European Journal of Clinical Pharmacology*, 62:513–521, 2006.
- [39] Kagimoto M, Heim M, Kagimoto K, Zeugin T, and Meyer UA. Multiple mutations of the human cytochrome–P450IID6 gene (CYP2D6) in poor metabolizers of debrisoquine – study of the functional–significance of individual mutations by expression of chimeric genes. *The Journal of Biological Chemistry*, 265:17209–17214, 1990.
- [40] Marez D, Legrand M, Sabbagh N, Lo Guidice JM, Spire C, Lafitte JJ, and et al. Polymorphism of the cytochrome P450 CYP2D6 gene in a European population: characterization of 48 mutations and 53 alleles, their frequencies and evolution. *Pharmacogenetics*, 7:193–202, 1997.
- [41] Hanioka N, Kimura S, Meyer UA, and Gonzalez FJ. The human CYP2D locus associated with a common genetic–defect in drug oxidation: a G1934–A base change in intron–3 of a mutant cyp2D6 allele results in an aberrant–3′ splice recognition site. *The American Journal of Human Genetics*, 47:994–1001, 1990.

- [42] Gough AC, Miles JS, Spurr NK, Moss JE, Gaedigk A, Eichelbaum M, and et al. Identification of the primary gene defect at the cytochrome-P450CYP 2D locus. *Nature*, 347:773–776, 1990.
- [43] Evert B, Griese EU, and Eichelbaum M. Cloning and sequencing of a new non-functional CYP2D6 allele – deletion of T–1795 in exon–3 generates a premature stop codon. *Pharmacogenetics*, 4:271–274, 1994.
- [44] Daly AK, Leathart JB, London SJ, and Idle JR. An inactive cytochrome-p450 CYP2D6 allele containing a deletion and a base substitution. *Human Genetics*, 95:337–341, 1995.
- [45] Saxena R, Shaw GL, Relling MV, Frame JN, Moir DT, Evans WE, and et al. Identification of a new variant CYP2D6 allele with a single–base deletion in exon–3 and its association with the poor metabolizer phenotype. *Hum Mol Genet*, 3:923–926, 1994.
- [46] Tyndale R, Aoyama T, Broly F, Matsunaga T, Inaba T, Kalow W, and et al. Identification of a new variant CYP2D6 allele lacking the codon encoding Lys–281–possible association with the poor metabolizer phenotype. *Pharmacogenetics*, 1:26–32, 1991.
- [47] Pedersen RS, Brosten K, and Nielsen E. Enantioselective HPLC Method for Quantitative Determination of Tramadol and O–Desmethyltramadol in Plasma and Urine: Application to Clinical Studies. *Chromatographia*, 57:279–285, 2003.
- [48] Abdel-Rahman SM, Leeder JS, Wilson JT, Gaedigk A, Gotschall RR, Medve R, Liao S, Spielberg SP, and Kearnsset GL. Concordance between tramadol and dextromethorphan parent/metabolite ratios: the influence of CYP2D6 and non-CYP2D6 pathways on biotransformation. *The Journal of Clinical Pharmacology*, 42:24–29, 2002.
- [49] Gillen C, Haurand M, Kobelt DJ, and Wnendt S. Aaffinity, potency and efficacy of tramadol and its metabolites at the cloned human  $\mu$ -opioid receptor. *Naunyn-Schmiedeberg's Archives of Pharmacology*, 362:116–121, 2000.
- [50] Paar WD, Frankus P, and Dengler HJ. The metabolism of tramadol in human liver microsomes. *Clin Invest*, 70:708–10, 1992.
- [51] Wu WN, Mckown LA, and Liao S. Metabolism of the analgesic drug ULTRAM (R) (tramadol hydrochloride) in humans: API–MS and MS/MS characterization of metabolites. *Xenobiotica*, 32:411–425, 2002.
- [52] van Dongen SM. *Graph Clustering by Flow Simulation*. PhD thesis, University of Utrecht, Netherlands, 2000.
- [53] Nowak MA. *Evolutionary Dynamics*. The Belnap Press of Harward University Press, 2006.
- [54] Danon L, Díaz-Guilera A, Duch J, and Arenas A. Comparing community structure identification. *Journal of Statistical Mechanics: Theory and Experiment*, 2005. P09008.

- [55] Troyanskaya O, Cantor M, Sherlock G, Brown P, Hastie T, Tibshirani R, Botstein D, and Altman R. Missing value estimation methods for dna microarrays. *Bioinformatics*, 17:520–525, 2001.
- [56] Bagnoli F, Berrones A, and Franci F. De gustibus disputandum (forecasting opinions by knowledge networks). *Physica A*, 332:509–518, 2004.
- [57] Maslov S and Zhang YC. Extracting hidden information from knowledge networks. *Phys Rev Lett*, 87:248701, 2001.
- [58] Gan X, Liew AWC, and Yan H. Microarray missing data imputation based on a set theoretic framework and biological knowledge. *Nucleic Acids Research*, 34:1608–1619, 2006.
- [59] Esponda F, Ackley ES, Helman P, Jia H, and Forrest S. Protecting data privacy through hard-to-reverse negative databases. In Springer LNCS, editor, *In proceedings of the 9th Information Security Conference (ISC'06)*, pages 72–84, 2006.
- [60] Misulis K E and Fakhoury T. *Spehlmann's Evoked Potential Primer*. Butterworth-Heinemann, 3rd edition, 2001.
- [61] De Pascalis V and Cacace I. Pain perception, obstructive imagery and phase-ordered gamma oscillations. *Int. J. Psychophysiol.*, 56:157–169, 2005.
- [62] Gross J, Schnitzler A, Timmermann L, and Ploner M. Gamma oscillations in human primary somatosensory cortex reflect pain perception. *PLoS Biol*, 5:1168–1173, 2007.
- [63] Danhof M, de Jongh J, De Lange ECM, Della Pasqua O, Ploeger BA, and Voskuyl RA. Mechanism-based pharmacokinetic–pharmacodynamic modeling: Biophase distribution, receptor theory, and dynamical systems analysis. *Annu. Rev. Pharmacol. Toxicol.*, 47:357–400, 2007.
- [64] van Kampen NG. *Stochastic processes in Physics and Chemistry*. North Holland, Amsterdam, 1992.
- [65] Lintz W, Barth H, Osterloh G, and Schmidt-Bothelt E. Bioavailability of enteral tramadol formulations. 1st communication: capsules. *Arzneimittelforschung*, 36:1278–1283, 1986.
- [66] Di Patti F and Fanelli D. Can a microscopic stochastic model explain the emergence of pain cycles in patients? *J Stat Mech*, 1:P01004, 2009.
- [67] Gardiner CW. *Handbook of Stochastic Methods*. Springer, second edition, 1985.
- [68] Pokora O and Lánský. Statistical approach in search for optimal signal in simple olfactory neuronal models. *Mathematical Biosciences*, 214:100–108, 2008.
- [69] Di Patti F and Fanelli D. On the molecular mechanisms driving pain perception and emergent collective behaviors. *Commun Nonlinear Sci Numer Simulat*, 15:1385–1399, 2010.

- [70] Gray P and Scott SK. Sustained oscillations and other exotic patterns of behavior in isothermal reactions. *J Phys Chem*, 89:22–32, 1985.
- [71] Jain S and Krishna S. Autocatalytic sets and the growth of complexity in an evolutionary model. *Phys Rev Lett*, 81:5684–5687, 1998.
- [72] Dyson F. *Origins of Life*. Cambridge University Press, Cambridge, England, 1985.
- [73] Kauffman SA. Autocatalytic sets of proteins. *J Theor Biol*, 119:1–24, 1986.
- [74] Stadler PF and Schuster P. Dynamics of small autocatalytic reaction networks – I. bifurcations, permanence and exclusion. *Bull Math Biol*, 52:485–508, 1990.
- [75] Wächtershäuser G. Evolution of the first metabolic cycles. *Proc Natl Acad Sci U.S.A.*, 87:200–204, 1990.
- [76] McKane AJ and Newman TJ. Stochastic models in population biology and their deterministic analogs. *Phys Rev E*, 70:041902, 2004.
- [77] Togashi Y and Kaneko K. Transitions induced by the discreteness of molecules in a small autocatalytic system. *Phys Rev Lett*, 86:2459–2462, 2001.
- [78] Togashi Y and Kaneko K. Alteration of chemical concentrations through discreteness-induced transitions in small autocatalytic systems. *J Phys Soc Jpn*, 72:62–68, 2003.
- [79] Gillespie DT. A general method for numerically simulating the stochastic time evolution of coupled chemical reactions. *J Comp Phys*, 22:403–434, 1976.
- [80] Bartlett MS. Measles periodicity and community size. *J R Stat Soc A*, 120:48–70, 1957.
- [81] Nisbet RM and Gurney WSC. *Modelling Fluctuating Populations*. Wiley, New York, 1982.
- [82] Gillespie DT. Exact stochastic simulation of coupled chemical reactions. *J Phys Chem*, 81:2340–2361, 1977.
- [83] Bellman R. *Introduction to Matrix Analysis*. McGraw–Hill, New York, 2–nd edition, 1970.
- [84] de Anna Pietro. studio analitico di quasi-cicli in un modello spaziale di cellula minimale. Master's thesis, Department of Physics, University of Florence, 2009.
- [85] de Anna P, Di Patti F, Fanelli D, McKane A J, and Dauxois T. Spatial model of autocatalytic reactions. *PRE*, 81:056110, 2010.
- [86] Lugo CA and McKane AJ. Quasicycles in a spatial predator–prey model. *Phys Rev E*, 78:051911, 2008.

PREMIO FIRENZE UNIVERSITY PRESS  
TESI DI DOTTORATO

- Coppi E., *Purines as Transmitter Molecules. Electrophysiological Studies on Purinergic Signalling in Different Cell Systems*, 2007
- Natali I., *The Ur-Portrait. Stephen Hero ed il processo di creazione artistica in A Portrait of the Artist as a Young Man*, 2007
- Petretto L., *Imprenditore ed Università nello start-up di impresa. Ruoli e relazioni critiche*, 2007
- Mannini M., *Molecular Magnetic Materials on Solid Surfaces*, 2007
- Bracardi M., *La Materia e lo Spirito. Mario Ridolfi nel paesaggio umbro*, 2007
- Bemporad F., *Folding and Aggregation Studies in the Acylphosphatase-Like Family*, 2008
- Buono A., *Esercito, istituzioni, territorio. Alloggiamenti militari e «case Herme» nello Stato di Milano (secoli XVI e XVII)*, 2008
- Castenasi S., *La finanza di progetto tra interesse pubblico e interessi privati*, 2008
- Gabbiani C., *Proteins as Possible Targets for Antitumor Metal Complexes: Biophysical Studies of their Interactions*, 2008
- Colica G., *Use of Microorganisms in the Removal of Pollutants from the Wastewater*, 2008
- Inzitari M., *Determinants of Mobility Disability in Older Adults: Evidence from Population-Based Epidemiologic Studies*, 2009
- Di Carlo P., *I Kalasha del Hindu Kush: ricerche linguistiche e antropologiche*, 2009
- Pace R., *Identità e diritti delle donne. Per una cittadinanza di genere nella formazione*, 2009
- Macrì F., *Verso un nuovo diritto penale sessuale. Diritto vivente, diritto comparato e prospettive di riforma della disciplina dei reati sessuali in Italia*, 2009
- Vignolini S., *Sub-Wavelength Probing and Modification of Complex Photonic Structures*, 2009
- Decorosi F., *Studio di ceppi batterici per il biorisanamento di suoli contaminati da Cr(VI)*, 2009
- Di Patti F., *Finite-Size Effects in Stochastic Models of Population Dynamics: Applications to Biomedicine and Biology*, 2009

Finito di stampare presso  
Grafiche Cappelli Srl - Osmannoro (FI)